Spring 2019

Inclusion engineering in FeMnAl steels

Rairu Vaz Penna

Department:

INCLUSION ENGINEERING IN FeMnAl STEELS

by

RAIRU VAZ PENNA

A THESIS

Presented to the Faculty of the Graduate School of the

MISSOURI UNIVERSITY OF SCIENCE AND TECHNOLOGY

In Partial Fulfillment of the Requirements for the Degree

MASTER OF SCIENCE IN METALLURGICAL ENGINEERING

2019

Approved by:

Laura N. Bartlett, Advisor
Simon N. Lekakh
Ronald J. O'Malley

PUBLICATION THESIS OPTION

This thesis contains three manuscripts prepared for journal publication in the style specified by Missouri University of Science and Technology:

Paper I: Pages 47-81 have been published in the International Journal of Metalcasting (IJMC).

Paper II: Pages 82-117 are intended for submission to International Journal of Metalcasting (IJMC).

Paper III: Pages 118-142 are intended for submission to International Journal of Metalcasting (IJMC).

ABSTRACT

Low density high Mn and Al steels, or FeMnAl steels, show great promise for military vehicles and automotive applications in which high strength and toughness is a requirement. However, these steels are subject to processing challenges including development of oxide and nitride inclusions during melting and casting as well as a large as-cast grain size and heavy interdendritic segregation. This can lead to non-uniform heat treatment response and cracking during subsequent hot rolling. Adding up to 10%Al lowers the density of these steels by as much as 15%, unfortunately, this also results in large amounts of hard and faceted AlN inclusions that are known to reduce toughness. Inclusion engineering techniques in other cast alloys can mitigate the effect of harmful inclusions or decrease grain size, segregation, and microporosity and improve ductility and toughness. Unfortunately, there is limited understanding of inclusion evolution in FeMnAl steels and the inclusion engineering strategies to improve mechanical properties.

The goal of this research is to explore potential nonmetallic inclusions as inoculants to refine the as-cast grain size as well as potential mitigation of detrimental AlN by soft and globular MnS co-precipitation. MnS was effective at coating most of the AlN inclusions. However, this produced a large overall inclusion population that reduced dynamic fracture toughness.

The potential of Ti(C,N), Nb(C,N), and complex Ce-oxides to refine the as-cast grain size was investigated. A decrease in the columnar zone was observed with addition of FeSiMg+FeTi and Ce addition, however, the equiaxed grain size did not decrease. A low N melt practice with Ti additions was effective at eliminating AlN.

ACKNOWLEDGMENTS

I would not be able to stand where I am today without the help of innumerous people along the way, people that assisted me, supported me or simply listened to me. I would like to first, and most importantly, thank my amazing wife, Lais, for all of her support. She has always been by my side through this long walk. Thank you for all of your sacrifices that have helped me accomplish this chapter in my life. The same also goes to my family that gave me great support to be here.

I am very grateful for Dr. Von Richards for giving me the opportunity to work with him as an undergraduate research assistant and opening the doors for me to come back and pursue my master's degree. My most sincere gratitude to Dr. Bartlett for all the guidance, and shared knowledge that helped me with the challenge as well as all of the uncountable hours in meetings and reviews for the continuous improvement of my work. I would also like to acknowledge Dr. O'Malley, Dr. Xu and especially Dr. Lekakh for all the thoughtful discussions and exchange of ideas.

For their patience and availability in assisting during experiment preparation, material purchases, and keeping things running as smoothly as possible, I am very thankful to Nathaniel Inskip, Brian Bullock, Teneke Hill, Denise Eddings. I would also like to thank Defense Logistics Agency in cooperation with Steel Founders Society and Army Research Lab for sponsoring this project. At last, I would like to thank all the fellow undergraduate and graduate students that helped with experiments, provided helpful discussion, and being my friends during moments of relaxation. Special thanks to my closer friends, Michael Piston, Koushik Balasubramanian, and Trevor Constance.

TABLE OF CONTENTS

Page

LIST OF ILLUSTRATIONS

SECTION Page

PAPER III

LIST OF TABLES

1. INTRODUCTION

1.1. PROJECT PURPOSE AND OVERVIEW

High manganese and aluminum steels or FeMnAl steels are a growing class of advanced high strength steels that are being considered for reducing the weight of military vehicles as well as in civilian transportation and in the mining industry. These steels have manganese concentrations from 15-30wt.% with aluminum and carbon contents from 5-12%wt.%Al, and 0.7-1.3wt.%C. Aluminum reduces the density up to 18% and this represents a possibility to decrease the overall weight of steel components with an improvement of strength and toughness. However, the performance of these steels is limited by the formation of detrimental inclusions during the melting and casting process that reduce toughness, high amounts of alloy segregation during solidification, and a large as-cast grain structure that is prone to cracking during subsequent thermomechanical processing. Therefore, the objective of this project was to understand inclusion evolution in high manganese and aluminum austenitic steels with the goal of engineering the inclusion population to improve toughness and refine the as-cast grain size. In the current study, a thermodynamic modeling approach combined with experimental validation was utilized to alter the shape of faceted AlN inclusions with the goal of improving dynamic fracture toughness. Controlled amounts of sulfur produced globular MnS that encapsulated AlN during solidification. In addition, two methods of inoculation-based melt practices were utilized with the intention of refining the as-cast grain size, *in-situ* formation of *TiN* on pre-existing *Mg-Al* spinel oxides, and a master alloy addition containing preformed *TiN*. Although grain refinement was not observed,

Ti additions were found to suppress AlN formation and this may be an effective way of controlling nitrogen.

1.2. HIGH MANGANESE AND ALUMINUM STEEL

Fe-Mn-Al-C steels are a class of high strength and low-density steels. They have been developed and explored over the years for wear resistant applications, oxidation resistance, and cryogenic applications. Recently studies have been focused on high strength and high energy absorption properties with target applications for ballistic armor as well as applications in the transportation industry. For these applications, the combination of high strength and toughness with a reduction in density up to 18% lower than martensitic high strength steels is highly valuable to decrease component weight. Austenitic FeMnAlC steel compositions are based on the original work by Robert Hadfield who developed high manganese steel over a century ago. [1] Hadfield steel is a cast steel containing Fe-Mn-C with typically 11-14%wt. Mn and 1.25%C used in abrasion resistance applications such as the mining and railroad industries.[1] The high manganese and carbon content of these steels stabilizes a metastable austenitic matrix with excellent strain hardening capacity and toughness. In the 1950s Ham and Cairns added aluminum to a modified composition of Hadfield steel with the intention of improving corrosion and oxidation resistance without costly Cr and Ni additions that are standard in 300 series stainless steels.[1,2]

The main property of the FeMnAl steels that makes them interesting alloys is the reduction in density that is mainly attributed by Al and C additions. This occurs by two mechanisms: elemental mass reduction and lattice expansion. The reduction in elemental

mass occurs by substitution of Fe in the FCC lattice by lighter Al atoms. Lattice expansion also occurs with increasing Al, decreasing the density of the unit cell. Figure 1.1 shows the influence of Al on austenite density, decreasing it from 8.1g/cm^{3}of pure Fe austenite to about 6.4g/cm^3 at a composition of Fe-30Mn-1C-10Al.[4] It should be noted that all compositions in the following text are expressed as weight percent unless otherwise noted.

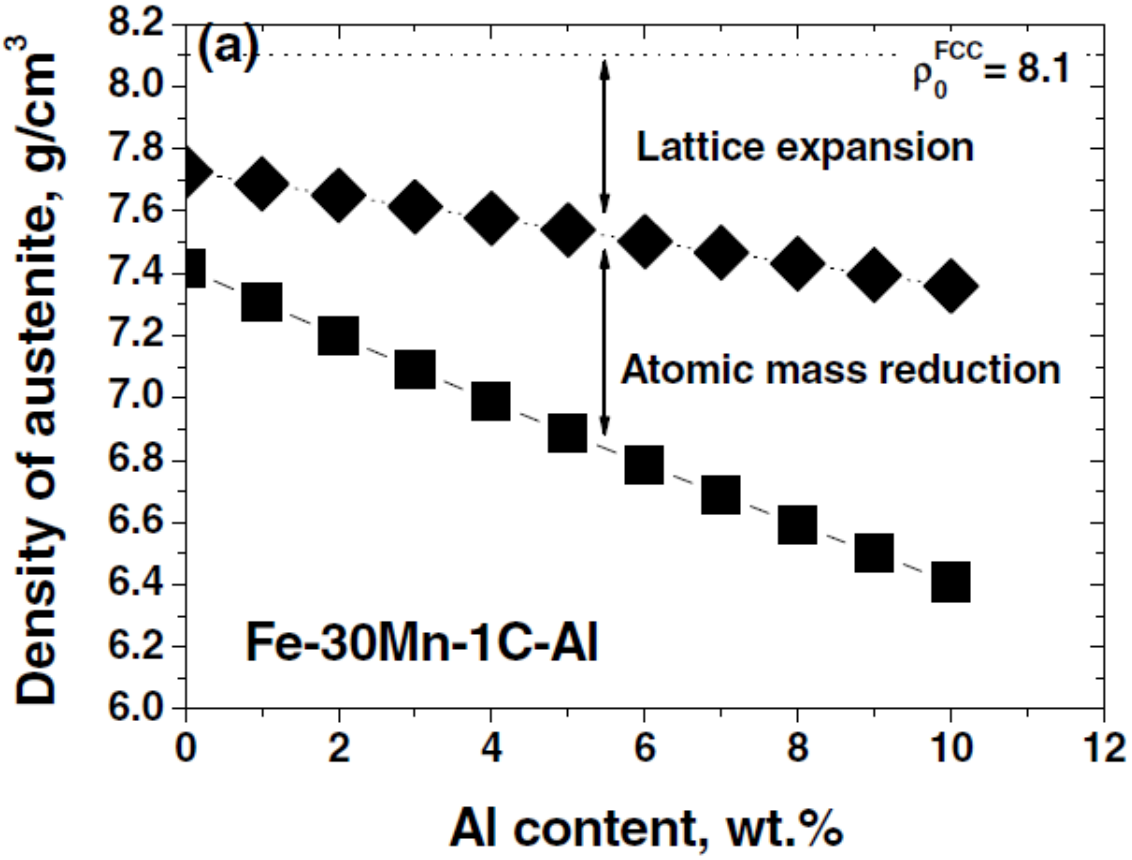

Figure 1.1. Correlation between the density of austenite and the Al content in Fe-30Mn-1C-XAl steels.[4]

The strength of austenitic Fe-Mn-Al-C steels can be greatly increased by the precipitation of κ-carbide. The κ-carbide phase can be formed in alloys with above approximately 6%Al and 0.7%C. The κ-carbide unit cell is shown in Figure 1.2, and has a composition of $(Fe,Mn)_3AlC_x$ and an $E2_1$ cubic perovskite crystal structure where Fe/Mn atoms occupy face positions, Al orders on corners, and a carbon occupies the octahedral interstitial position.[5]

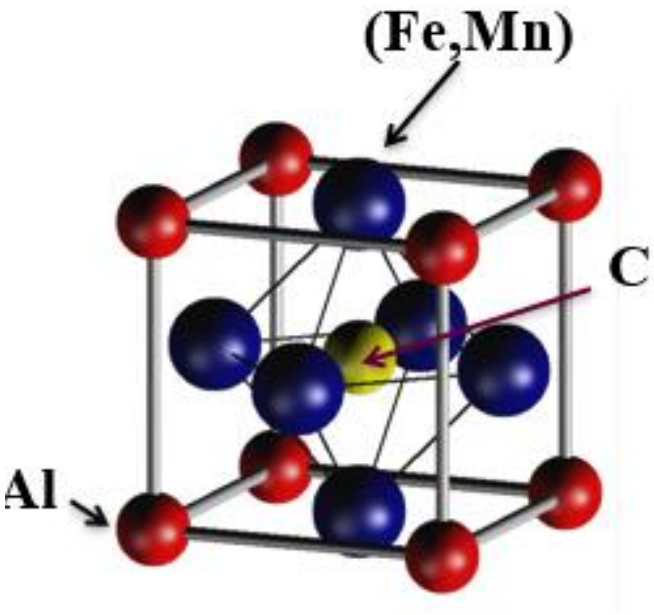

Figure 1.2. The κ-carbide has the Perovskite $E2_1$ crystal structure with Fe/Mn atoms on faces, Al atoms on corners and C atoms in the middle of the unit cell.

κ-carbide precipitation occurs on grain boundaries during slow cooling of the steel after solidification or during heat treatment and this is amplified by a large as-cast

grain structure and high amounts of alloy segregation. Therefore these steels are solution treated at temperatures from 1050°C to 1100°C for at least 2 hours prior to rapid quenching to avoid κ-carbide precipitation on grain boundaries.[6]

However, a very important hardening mechanism for Fe-Mn-Al-C steels is through controlled homogeneous precipitation of coherent nanosized κ-carbide within the austenite matrix. Age hardening of FeMnAlC steels is limited by the composition range where κ-carbide can precipitate. An experimental relationship on the influence of composition on the stability of κ-carbide was derived by previous authors and is shown in Eq. (1) .[7,8]

$$0.098\ (wt\%\ Al) + 0.208\ (wt\%\ C) > 1 - 0.0054\ (wt\%\ Mn) \quad (1)$$

For a steel with composition of Fe-28Mn-8.5Al-1C-1.25Si an isothermal phase transformation diagram was constructed by Acselrad et al. in the temperature range from 300 to 1000°C, in Figure 1.3.[9] According to his diagram, the precipitation of κ-carbide occurs in the range of 400 to 950°C. Precipitation occurs homogeneously in the matrix for temperatures below 550°C and on grain boundaries for temperatures above that temperature. This is the reason why most studies have considered aging temperatures in the range of 530-550°C.[10] Prolonged aging above 550°C can also stabilize B2 or DO_3 intermetallic phases that embrittles grain boundaries.[9]

Austenitic compositions of interest are in the range of Fe-(15-30)Mn-(3-12)Al-(0.5-1.5)C with additions of other minor alloying elements such as Si, Mo, and Ni. Silicon additions between 0.5 and 1.5%Si are routinely added in both cast and wrought steels to prevent the precipitation of brittle β-Mn during age hardening and to increase fluidity during casting processes.[11,12]

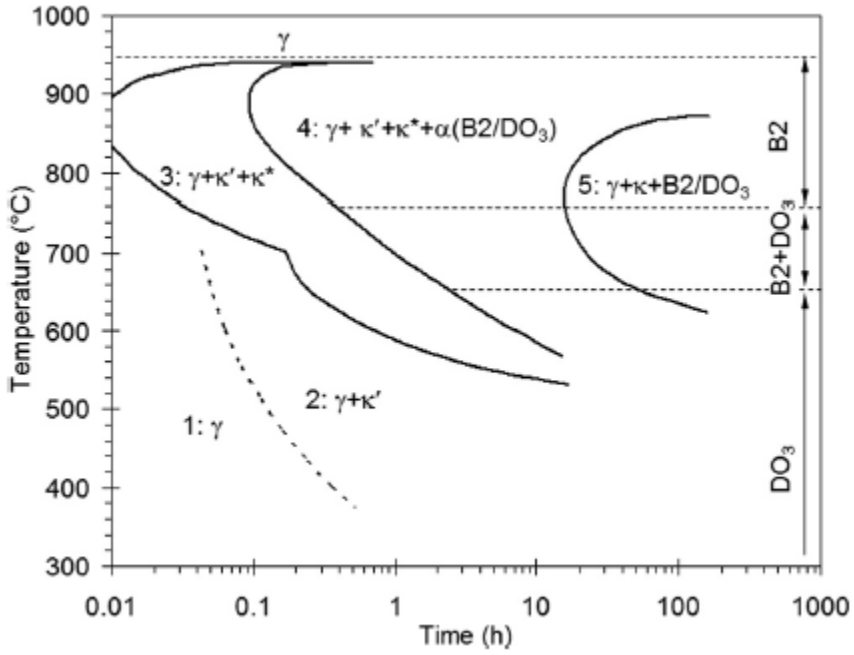

Figure 1.3. Diagram of isothermal phase transformation for Fe-28Mn-8.5Al-1C-1.25Si. The intragranular homogenous precipitation of κ-carbide is identified by κ` and occurs at lower temperatures in region 2. Region 3 represents the region where the precipitation occurs homogeneously in the matrix, κ`, and in the grain boundaries of the steel, κ*. Regions 2 is thus the appropriate region for aging processes targeting homogeneous precipitation of κ-carbides.[9]

1.2.1. Solidification Behavior. The solidification path in FeMnAlC steels can start as primary γ-austenite or primary δ-ferrite with austenite forming later through a peritectic. Because of the high alloy content, the stable phase depends on composition. Additions of Mn and C will favor the stability of austenite and additions of Al and Si stabilize ferrite.[13] Chen et al. classified FeMnAlC steels into four different types according to composition.[10] These are summarized in Table 1.1.

The focus of the current work is on alloys that are fully austenitic at room temperature as shown in the last column of Table 1.1. Initial solidification as δ-ferrite is

favored even in the austenitic alloy range, except for compositions with Mn>28%, Al<6% and C>1.5% . As temperature decreases, the δ-ferrite is partially transformed to γ-austenite through a peritectic reaction.[10] Figure 1.4(a) shows that even though the Fe-30Mn-9Al-1C composition is fully austenitic at 1000°C, solidification starts with the formation of up to 40% of δ-ferrite. The solid first phase formed from the liquid has an important impact in the final microstructure. Therefore, controlled additions to promote grain refinement must be designed to nucleate either ferrite or austenite depending on composition. At higher carbon contents (>1.5%) and lower aluminum (<6%) the steel can solidify as a fully austenitic alloy without formation of δ-ferrite, as in Figure 1.4(b).

Table 1.1. Different classes of Fe-Mn-Al-C steels based on microstructure.[10]

	Ferritic	**Ferritic based duplex**	**Austenite based duplex**	**Austenitic**
Alloying range	Al ~ 5-9% Mn< 5% C< 0.05%	Al ~ 3-7% Mn ~ 2-12% C ~ 0.05%-0.5%	Al ~ 5-10% Mn ~ 5-30% C ~ 0.4-0.7%	Al ~ 5-12% Mn ~ 12-30% C ~ 0.6-2.0%

1.2.2. Microstructure and Mechanical Properties. The effect of Mn, Al, and C on the mechanical properties was studied by Kalashnikov for wrought steels. The strength, ductility, and U-notch toughness were evaluated for alloys solution treated for 2h at 1050°C and aged for 16h at 550°C, as shown in Figures (5-7).[6]

As shown in Figure 1.5, carbon continuously increases the strength of aged Fe-30Mn-9Al-XC steels with a maximum ultimate tensile strength, UTS, of 1300MPa when

carbon is 1.2%. Room temperature notch toughness and ductility appear to have maximum values around 120 J/cm^2 and 50%, respectively, for the Fe-30Mn-9Al-0.8C steel.

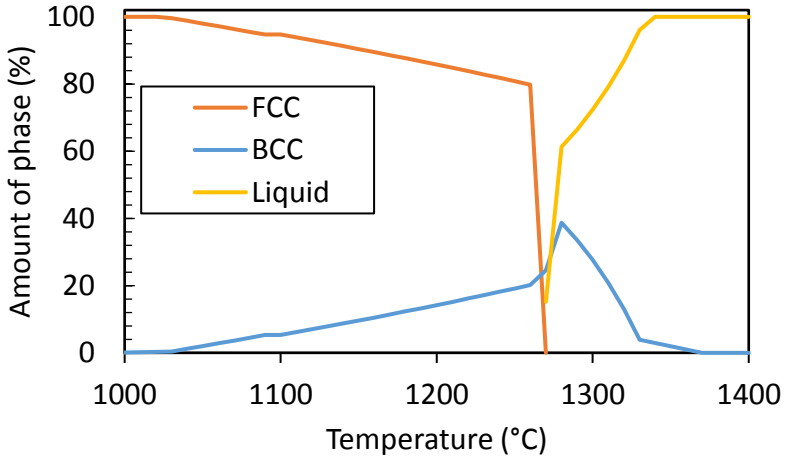

(a)

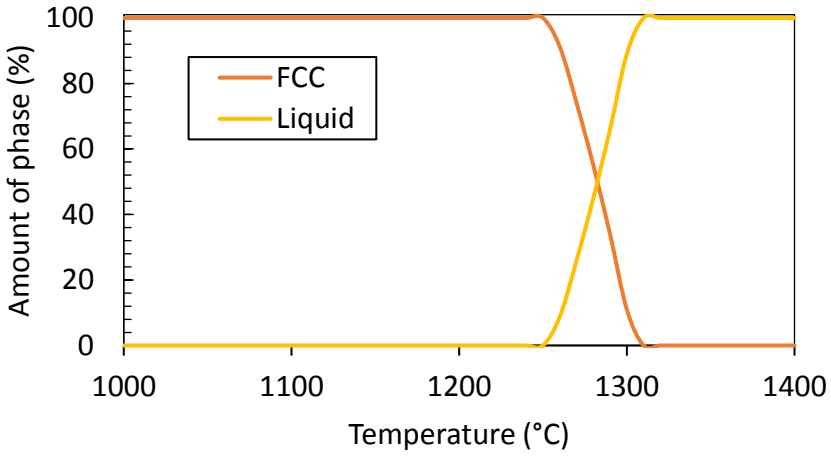

(b)

Figure 1.4. Solidification sequence as modeled utilizing ThermoCalc 7.0 thermodynamic modeling software. (a) For Fe-30Mn-9Al-1C steel, δ-ferrite is the primary phase followed by austenite formation well after the liquidus temperature of 1332°C. (b) For Fe-30Mn-5.6Al-1.5C steel, primary austenite forms and remains stable until room temperature.

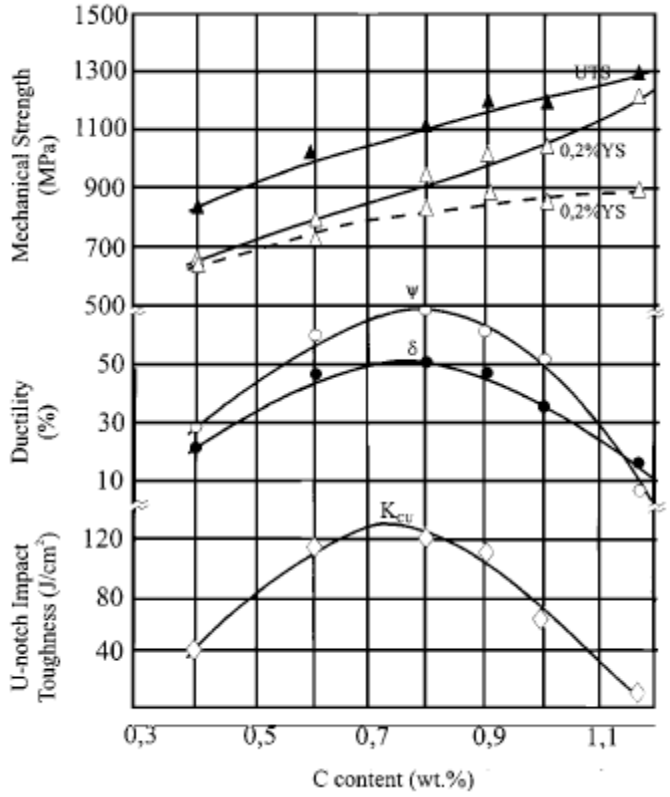

Figure 1.5. Effect of carbon content on the mechanical properties of wrought Fe-30Mn-9Al steel. The dashed lines represent specimens tested in the solution treated condition while solid curves were solution treated, quenched, and aged for 16h at 530°C. [14]

Aluminum has been shown by several authors to increase strength and decrease ductility as shown in Figure 1.6 for the aged Fe-30Mn-(0.85-0.95)C steel. Correspondingly, aluminum generally decreases toughness in age hardened steels as shown in Figure 1.6. Several authors have reported this to be the result of short-range ordering of the austenite as well as precipitation of intermetallic phases on grain boundaries when Al contents are greater than 9%.[14,15] The manganese content

maximizes notch toughness and ductility at 30%, with a small loss in tensile strength, as shown in Figure 1.7.

The mechanical properties of Fe-Mn-Al-C steels cover a wide range of values and are intrinsically controlled by the microstructure and heat treatment. The ultimate tensile strength, UTS, of Fe-Mn-Al-C steels with fully austenitic microstructures has been reported to be between 0.8 and 1 GPa with elongations between 10% and 80% at lower UTS around 800MPa depending on the heat treatment condition.[7,16]

In the solution treated condition, Fe-30Mn-9Al-0.9C steels have mainly an austenitic matrix microstructure with less than 10% retained δ-ferrite. Steels with a fully austenitic microstructure as in Table 1.1, present total elongations of up to 80%, yield strengths up to 700MPa, and CVN impact toughness up to 200J at room temperature when in the solution treated condition.[10,17] Figure 1.8 shows the range of properties for different aging times at 530°C for a Fe-30Mn-9Al-0.9C-1Si alloy. Wrought steels show a higher tensile strength than cast steels at equivalent aging times. The tensile strength for cast steels at peak aging can be above 1GPa, however the total elongation is less than 20%. In solution treated steels, elongation values have been reported close to 50% with tensile strength over 700MPa.[17]

The hardening effect is closely related to the carbon content and the aging temperature. Lower temperatures and higher carbon contents yield higher hardness as shown in Figure 1.9. In general, a maximum hardness of 450 HBN was reported for nominal compositions Fe-30Mn-8Al-1.5C steel aged at 530°C.[18,19] The kinetics of the hardening process and κ-carbide precipitation have been shown to be related mainly to Al and C content, as well as a phosphorus content.[7,14,17]

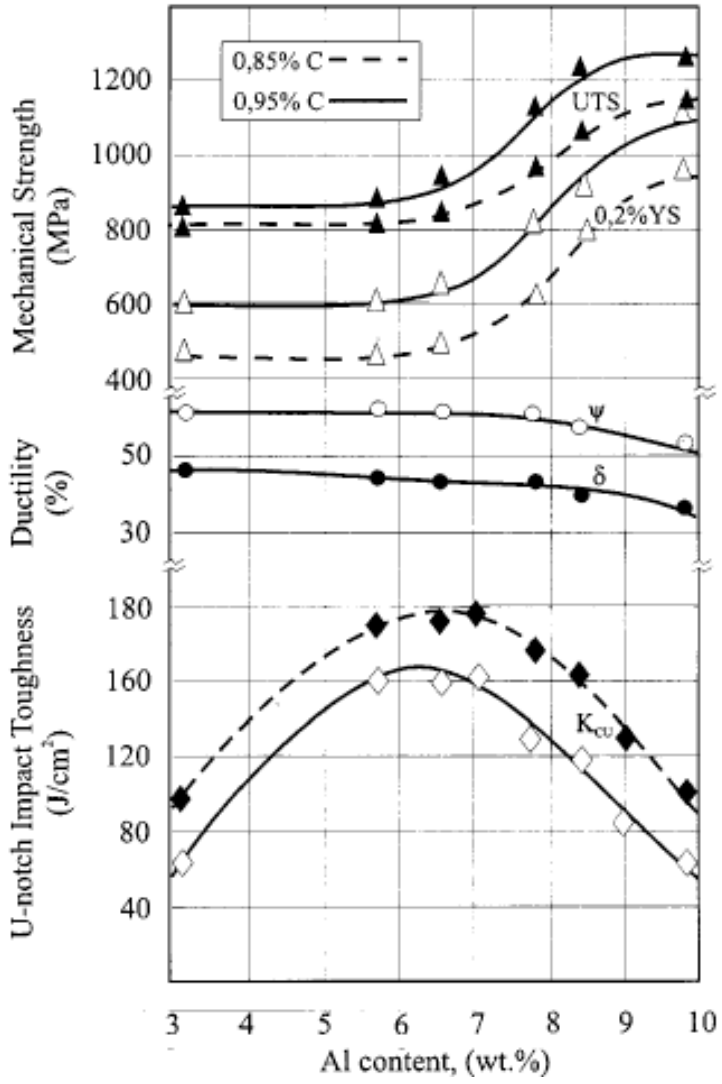

Figure 1.6. Effect of aluminum on the mechanical properties of Fe-30Mn-(0.85-0.95)C. The steel was solution treated at 1050°C for 2h and then aged at 550°C for 16h. [14]

When age hardened, the hardness, yield strength, and ultimate tensile strength increases at the expense of a decrease in the total elongation and toughness. During aging 530°C for 10h, a steel casting with composition of Fe-29Mn-8Al-0.9C-0.5Mo-1.4Si increased in yield strength from 549 to 891MPa but decreased in total elongation from 44

to 18%. Further aging for a total of 30h increased yield strength to 1016MPa and decreased elongation to 5%.[7,17] In a similar study, aging the same steel from the solution treated condition, from a hardness of 200 HBN to 350 HBN, decreased the room temperature notch toughness from 199J in the solution treated condition to only 55J.[17]

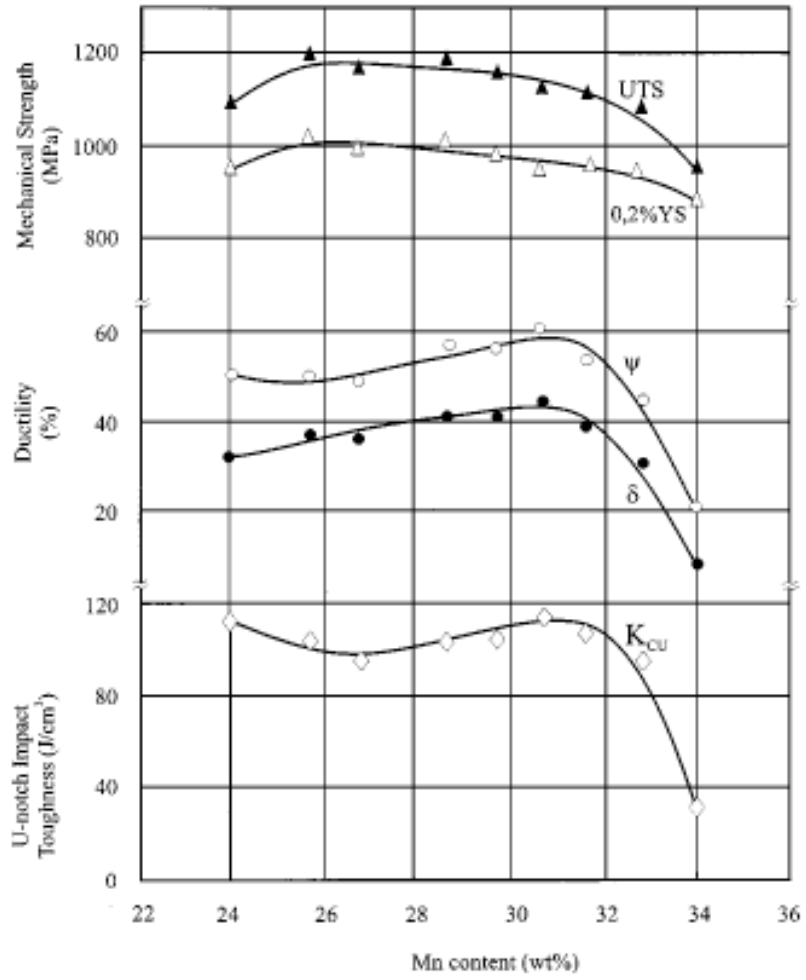

Figure 1.7. Effect of manganese on the mechanical properties of Fe-9Al-0.9C steel solution treated at 1050°C for 2h and then aged at 550°C for 16h. [14]

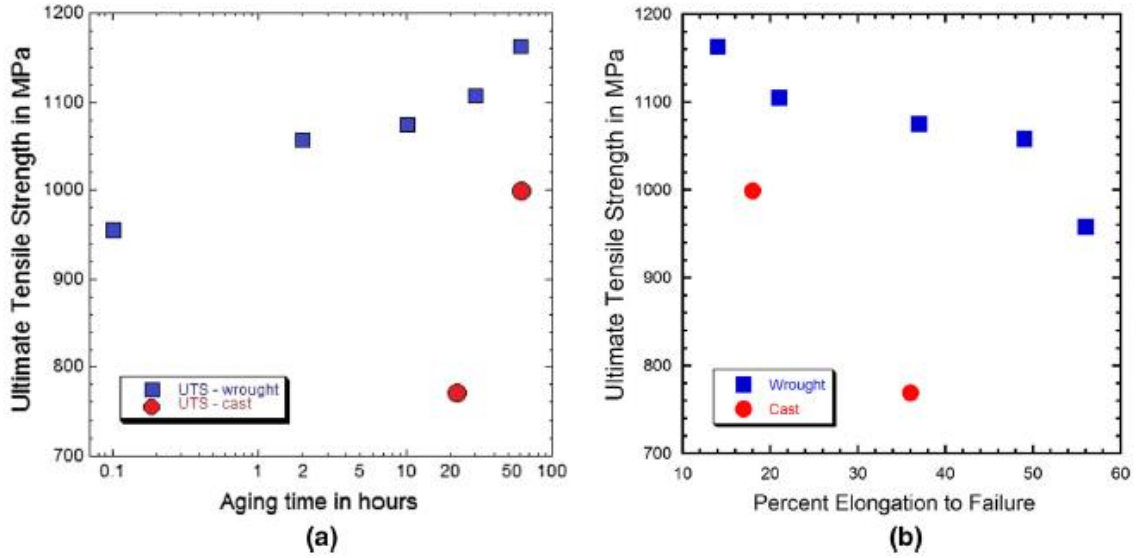

Figure 1.8. Mechanical properties of a Fe-30Mn-9Al-0.9C-1Si steel. (a) The ultimate tensile strength (UTS) as a function of aging time at 530°C. (b) The UTS and elongation for steels in (a) shows an inverse relationship between UTS and elongation.[17]

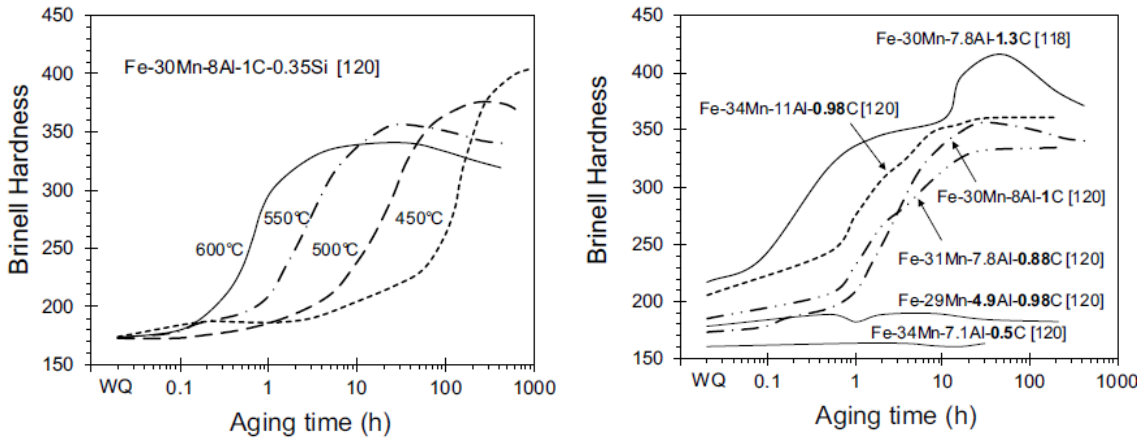

(a) (b)

Figure 1.9. The effect of aging temperature and carbon content on the age hardening process. (a) Increasing age hardening temperature speeds the aging kinetics but decreases the maximum hardness and (b) increasing carbon increases the overall hardening kinetics at 550°C.[10,18,19]

Dynamic fracture toughness (DFT) was evaluated for a Fe-30Mn-(3-9)Al-(0.9-1.2)C steel in a study by Bartlett et al. The study showed that aged FeMnAlC steels can attain a dynamic fracture toughness, $J_{ID,}$ above 100kJ/mm^2, comparable to commercial quenched and tempered high strength steels such as 4325 and 4130 at the same hardness levels.[20] In the solution treated and quenched condition DFT values above 700 kJ/mm^2 have been reported for Fe-30Mn-(3-9)Al-(0.9-1.2)C steels.[21,22]

Improvement in toughness is unlikely to be achieved through precipitation of κ-carbide. Other methods available to increase toughness include grain refinement, solid solution hardening, and inclusion control. Grain refinement methods during normalizing heat treatments are commonly performed to steels which have an α→γ transformation at heat treatment temperatures. During a phase transformation each grain nucleates several grains of the new phase, thus refining the microstructure.[23] It is well known that compositions similar to Fe-30Mn-9Al-1C present fully austenitic microstructures below 1200°C.[21,24] Because of the absence of polymorphic phase transformations, grain size control of cast FeMnAlC steels cannot be achieved during heat treatment.

Another limiting characteristic of the FeMnAlC steels is related to the steel cleanliness. Because of the high aluminum content, large amounts of AlN and complex MnO-Al_2O_3 bi-films have been observed to precipitate during melting and melt transfer.[17,25] The presence of such nonmetallic inclusions usually has detrimental effects on the mechanical properties of these steel. It has already been shown that presence of AlN in FeMnAlC steel is detrimental to the impact properties even at relatively low amounts (<50particles/mm^2).[20,26]

1.3. NONMETALLIC INCLUSIONS

Nonmetallic inclusions have different sources and a variety of effects depending on the material processing, inclusion type and material. Some of these characteristics are discussed below.

1.3.1. Inclusions Sources. Nonmetallic inclusions are commonly classified into endogenous and exogenous particles. The exogenous inclusions are introduced from external sources, such as particles of dust, refractories materials, re-oxidation, and slag entrainment. The endogenous inclusions are mainly oxides, sulfides, nitrides, and carbides that are formed in the steel as a consequence of chemical reactions during the steel refining process. Exogenous inclusions are usually larger than 10 μm in size, much larger than the endogenous inclusions which are typically less 5 μm.

In low alloy steels, the majority of the inclusions are formed as a product of the steel deoxidation. The deoxidation process consists of the addition of elements with high affinity with oxygen to form stable phases in the liquid steel and decrease the amount of oxygen in solution. A high amount of dissolved oxygen during solidification can cause a large amount of oxide precipitation, gas generation, and pinhole porosity.[27] Commonly used deoxidants in steel castings include Mn, Si, Al, and Ca that are often added as ferroalloys. Nonmetallic inclusions can also be the result of reaction with oxygen in the air during metal transfer as well as by chemical interaction with slags and refractories.

Sulfides are also common in steel castings. Sulfur is commonly present in the charge material used to produce steel and enters the system as a contamination element. The solubility of sulfur in solid steel is generally very low, on the order of a few parts per million, ppm. Segregation of sulfur and precipitation of low melting point liquid FeS in

the last areas to solidify and on grain boundaries can cause hot shortness and hot tearing for steels with high sulfur, for low-manganese steels that would be for Mn:S ratio <4.[23] Calcium is added to steel to remove sulfur after deoxidation and forms high temperature CaS inclusions. The solid CaS inclusions can be removed from the melt by stirring with argon bubbling using an argon lance or a porous plug in the bottom of the furnace.[28] The remaining sulfur in the steel typically forms MnS inclusions upon solidification that can be beneficial but machinability and detrimental to impact properties if they are present in large quantities.

1.3.2. Harmful Effects. Nonmetallic inclusions present in the steel can have beneficial effects such as in ODS strengthened steel and inclusions utilized for grain refinement. However, many nonmetallic inclusions are considered to be detrimental to mechanical properties. Much research has been directed toward controlling the type, shape, number, and distribution of nonmetallic inclusions to minimize their detrimental effects on mechanical properties.

The presence of non-metallic inclusions is in general detrimental to elongation and toughness. In steel alloys, the presence of inclusions also has a direct negative effect on the impact properties, fatigue, and fracture toughness.[29] The nonmetallic inclusions affect the mechanical properties by decreasing the critical stress for the crack nucleation and propagation process. As the steel matrix deforms around the inclusion, the inclusion can fracture by different mechanisms:[27]

- Inclusion decohesion from the matrix;

- Inclusion fracture with propagation to the matrix;

- Creation of stress concentration zones in sharp corners of the inclusions;

- Presence of residual stress in the matrix surround the inclusion as a result of differences in the thermal expansion coefficient during solidification and cooling of the steel.

The different mechanisms will occur depending on the inclusion properties. Hard and brittle inclusions such as alumina and AlN cannot deform when the steel deforms and so they tend to fracture or de-bond from the matrix. A faceted morphology also leads to stress concentration in the corners. Soft inclusions can deform with the steel, but that deformation leads to stress on the interface between the inclusions and the steel leading to decohesion and automatic void nucleation. Inclusions with a lower thermal expansion coefficient than steel will shrink less during cooling than the matrix surrounding it and this will lead to residual stresses on the matrix.[27,29,30] Figure 1.10 shows the thermal expansion coefficient of a few non-metallic inclusions, as it can be seen inclusions such as SiO_2, Al_2O_3, and TiN have lower thermal expansion coefficients and thus this leads to residual stress within the matrix. Inclusions such as CaS and MnS have much higher thermal expansion coefficients which may lead to decohesion from the matrix.

In general, despite having a lower or higher thermal expansion than the matrix, inclusions have a detrimental effect on the mechanical properties of steels, especially total elongation and impact toughness. Thornton reviewed the influence of NMI on mechanical properties of a 4340 steel and showed that increases in inclusion density characterized can decrease total elongation by over 50% as in Figure 1.11. The NMI does not have much effect on the UTS and yield strength.[29]

In rolled materials, inclusions have the additional effect of increasing anisotropy. During the rolling process, the inclusions tend to either fracture or elongate along the

rolling direction. Anisotropy is generally increased during the rolling process for steels with a high inclusion density.[32]

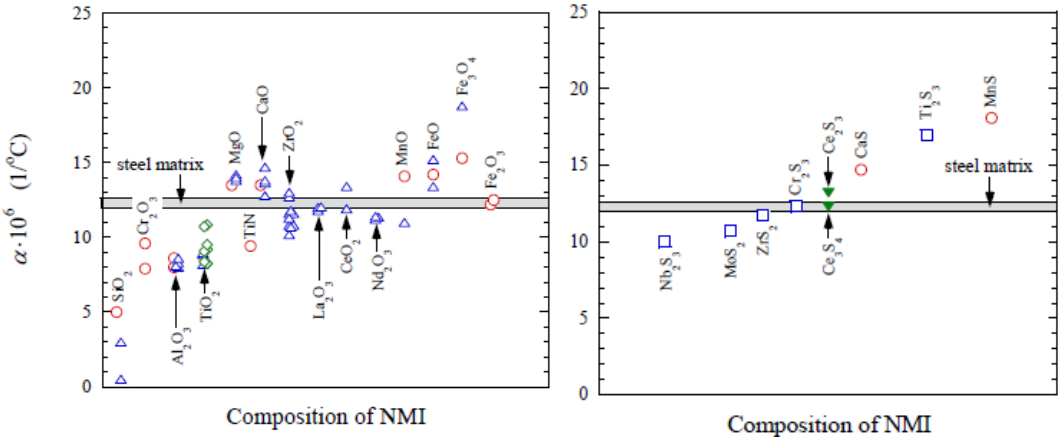

Figure 1.10. Thermal expansion coefficients of different non-metallic inclusions (NMI).[30]

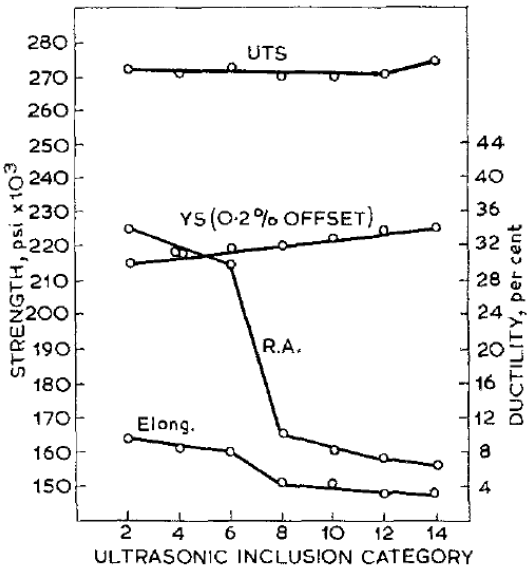

Figure 1.11. Influence of NMI in the tensile mechanical properties of a 4340 steel.[32]

The main effect of NMI is on properties related to the fracture of the material. This occurs because NMI are usually starting points for the nucleation of voids during deformation. The voids start either by decohesion from the matrix or due to fracture of the NMI at a stress much lower than the required to fracture the steel matrix. The voids then grow and coalesce with neighboring voids nucleated from other particles.[33] The process is exemplified in Figure 1.12.

An inverse relationship between the volume fraction of NMI and fracture toughness of material has been proposed by Hahn et al.[35] The plain strain fracture toughness describes the ability of a material to resist fracture in the presence of a crack or flaw. The plane strain fracture toughness of a material can be represented by the critical stress intensity factor, K_{IC}. For materials that display significant ductility and blunting of the crack tip, an elastic plastic fracture mechanics is used and is determined by the critical J-integral, J_{IC}. FeMnAlC steel can display both ductile and brittle behavior during fracture and that mainly depends on the degree of age hardening. The direct effect of the NMI volume fraction is demonstrated by the mechanism in Figure 1.12. Hahn et al. determined a mathematical model that described the effect of inclusion diameter, d, and the volume fraction of particles, V_F, on the fracture toughness, J_{Ic}, of aluminum alloys and found an inverse relationship between volume fraction of NMI and fracture toughness as shown in Eq. (2):

$$J_{Ic} = V_F^{-\frac{1}{3}} \sqrt{2\left(\frac{\pi}{6}\right)^{\frac{1}{3}} \sigma_Y d} \qquad (2)$$

where σ_Y is the yield strength.[35] A further development of the equation also done by Hahn et al. and shows a linear relationship between the J_{Ic} and the inclusion spacing, L_0 in

Eq. (3). This relationship shows that the J_{Ic} is diminished equally by increase in the volume fraction of inclusions as well as a decrease in inclusion spacing. It should be noted that the relationships proposed by Hahn et al. were for a spherical alumina particles. It is more likely that different inclusions have different effects on toughness because of the differences in shape, physical and mechanical properties, and the nature of the bonding between the matrix and the inclusions.

$$J_{Ic} \sim 2\sigma_Y L_0 \tag{3}$$

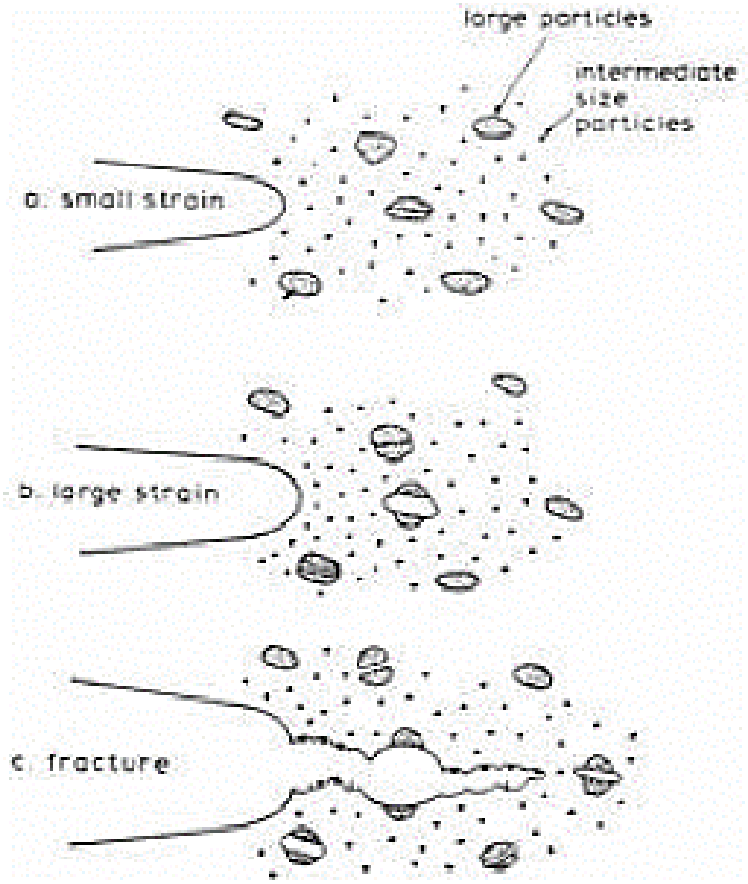

Figure 1.12. Mechanism of void nucleation by particle cracking in the strained region ahead of the crack tip. Additional strain leads to coalescence of the voids and early fracture when the particle spacing is reduced.[34]

Dynamic fracture toughness (DFT) is evaluated using an instrumented Charpy impact test to determine the fracture toughness by a linear elastic or elastic plastic fracture mechanics approach. The DFT in the solution treated condition was observed to decrease from 380kJ/m^2 to 60kJ/m^2 when AlN increased from 10 to 40 particles/mm^2.[22]

Figure. 1.13 shows the DFT of quenched and tempered Cr an Mo cast steels with different additions of Ni in comparison with FeMnAl cast steel with a nominal composition of Fe-30Mn-9Al-0.9C-1Si-0.5Mo that was aged to approximately 302 BHN. In this study, the effects of different deoxidant practices on the DFT of different high strength steels with similar hardness was determined. It was observed that the dynamic fracture toughness (DFT) increased linearlly with inclusion spacing and decreased linearlly with inclusion density.[20] It was also observed that steels deoxidized with Al and Al+Ca had higher DFT at similar inclusion density than steels deoxidized by Ti.

Fractography revealed the presence of fractured TiN in steels deoxidized with Ti additions. These inclusions were brittle and fractured in the strained area ahead of the crack tip during failure. In contrast, soft and globular calcium aluminate steels were found in steels deoxidized with Al and Ca. These inclusions were able to deform and de-bond from the matrix and thus increase the fracture energy when compared to TiN inclusions. The FeMnAlC steel was shown to contain mainly sharp and crystallographic AlN and globular MnS inclusions.

1.3.3. Beneficial Effects. Nonmetallic inclusions can also be beneficial to mechanical properties for further steel processing in situations like promoting grain

refinement, improving machinability, and controlling the detrimental effect of other inclusions.

The use of NMI to improve machinability of steels is commonly used in many steels. Resulfurized steels have additions of sulfur in order to form (Ca,Mn)S and aid machinability. Studies report a decrease in cutting force, power consumption, and tool wear rate for steels with the presence of MnS when compared to low sulfur steels.[30] Several mechanisms are involved in the improvement in machinability due to the presence of MnS: formation of stress fields in the steel matrix, a lower hardness of MnS compared to the matrix, lower friction between tool and chip, and others.[30]

The non-metallic inclusions control grain size by acting as nucleation sites during solidification and by limiting grain growth during recrystallization. The presence of particles in the liquid with low interfacial energy with the solid during the beginning stages of solidification decreases the energy barrier for nucleation and increases the number of active nuclei for grain growth. The higher number of nuclei leads to limited growth prior to contacting the adjacent grains. Several studies can be found in recent literature on the use of carbides and nitrides for controlling grain size of steels during solidification or during processing. In plain carbon and low alloy steels, some examples are the use of NbC and TiC to successfully refine the as-cast grain structure while in stainless TiN has also been successful.[36-38]

1.3.4. The Concept of Inclusion Engineering. Non-metallic inclusions can be engineered in order to have beneficial effects or limit their detrimental effect on the steel properties. The size, shape distribution and composition of the NMI population is therefore controlled in order to achieve the desired objective. In order to be able to

control the properties of nonmetallic inclusions, it is necessary to deeply understand their formation, interaction, and their effect on steel properties.[39]

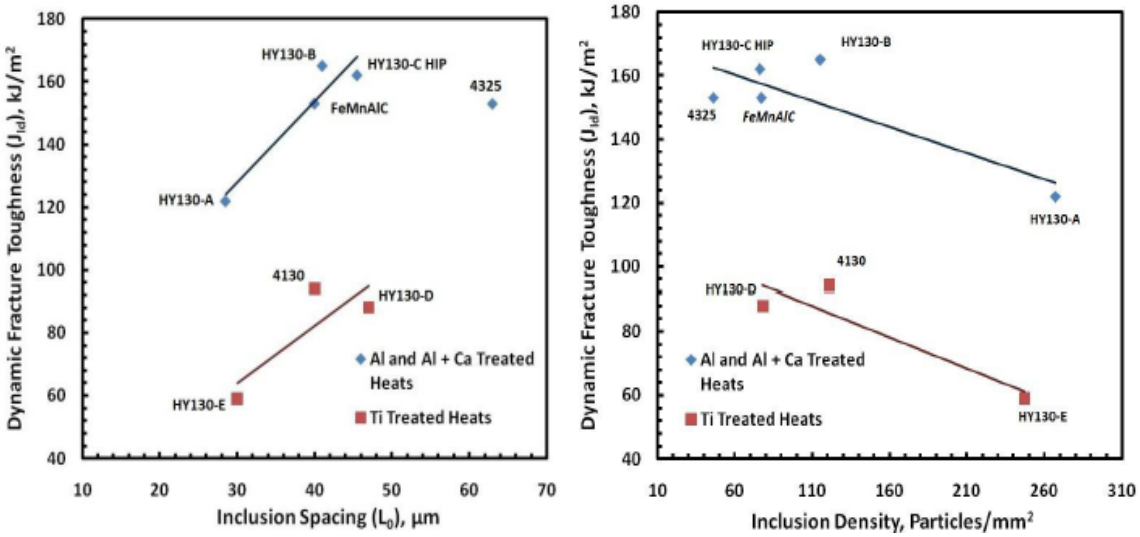

(a) (b)

Figure 1.13. The effect of inclusion spacing and number density on DFT for different quenched and tempered Cr, Mo, and Ni cast steels in comparison to a Fe-30Mn-9Al-0.9C-1Si-0.5Mo steel. (a) The DFT increases linearly with inclusion spacing and (b) decreases linearly with inclusion density.[20]

One of the most common methods of inclusion engineering is the control of inclusions physical and mechanical properties during calcium treatment. Calcium treatment in aluminum-killed steels is a well-stablished method to control the inclusion population, by changing their composition, morphology and size distribution.[40] Al_2O_3 inclusions in aluminum-killed steels tend to clog nozzles in the continuous casting processes. The addition of calcium modifies the inclusion composition and produces

liquid calcium-aluminates that do not clog nozzles. Calcium desulfurization treatment also helps to controls the detrimental effects of sulfides in rolled steel, by creating CaS inclusions that are stable at steelmaking temperature and can be floated out into the slag. In addition, Ca treatment can also form solid solution (Ca,Mn)S that does not deform as much as MnS during rolling, decreasing anisotropy.[40]

Figure 1.14 shows the binary phase diagram for $CaO\text{-}Al_2O_3$. In order for the inclusions formed by the addition of calcium to be liquid, there is a specific composition range 38-58wt% of CaO in solution in the inclusion.[40] Outside of this range, solid inclusion will be formed and the nozzle clogging will still occur. Additionally, the composition of the inclusions might change over time and leave that range, making it necessary to form the inclusions at the correct time.

The activity of different elements in the liquid steel can also be controlled to modify the inclusion population. The morphology of Al_2O_3 and MnS is controlled by controlling the activity of deoxidants, oxygen, and sulfur in the steel. Dendritic morphologies of inclusions are the most detrimental for mechanical properties and globular inclusions have the least influence. Figure 1.15 shows the morphology change of alumina and Figure 1.16 of MnS by controlling the activity of deoxidants and oxygen.[41,42] Controlling this composition variable to modify the morphology of the inclusions can decrease greatly the detrimental effect in the mechanical properties. A dendritic morphology leads to higher stress concentration factor around the inclusion and dendritic inclusions are typically larger which also makes it a more effective crack initiation site.[43]

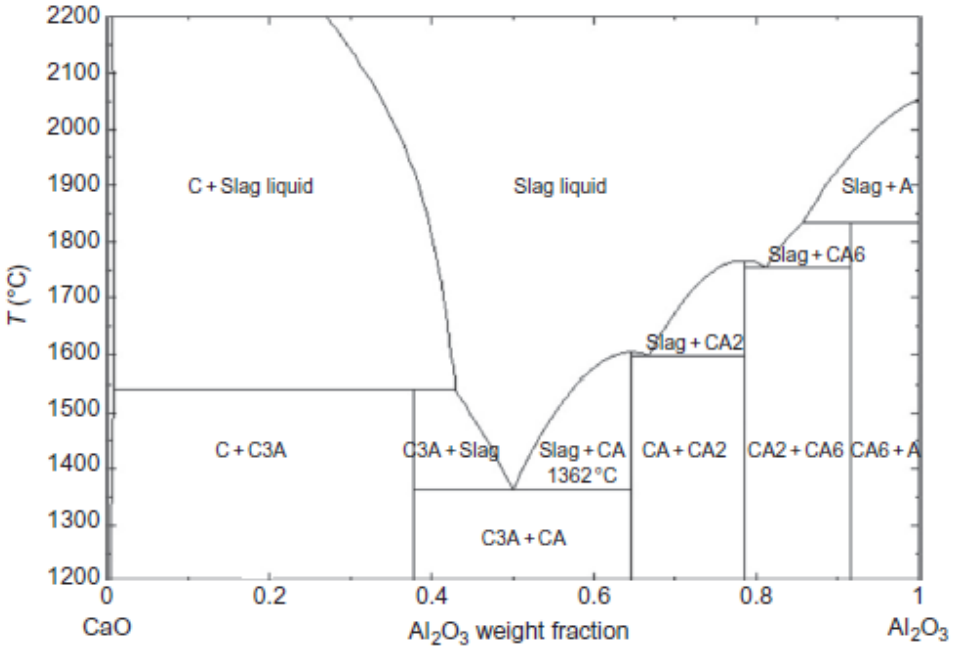

Figure 1.14. Binary solid solution diagram of CaO-Al2O3 at steelmaking temperatures.[40]

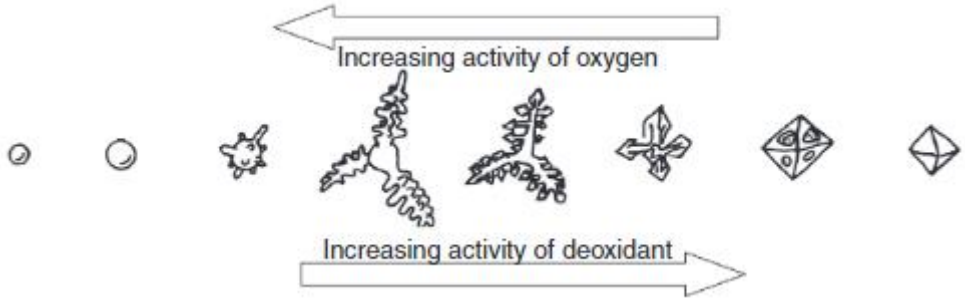

Figure 1.15. Influence of oxygen and deoxidant activity on the morphology of Al2O3 inclusion in aluminum killed steels.[41]

From the above discussion it becomes clear how important it is to control inclusions for effective removal or to modify the morphology, type, composition, size distribution, and volume fraction of inclusions in high strength steels.

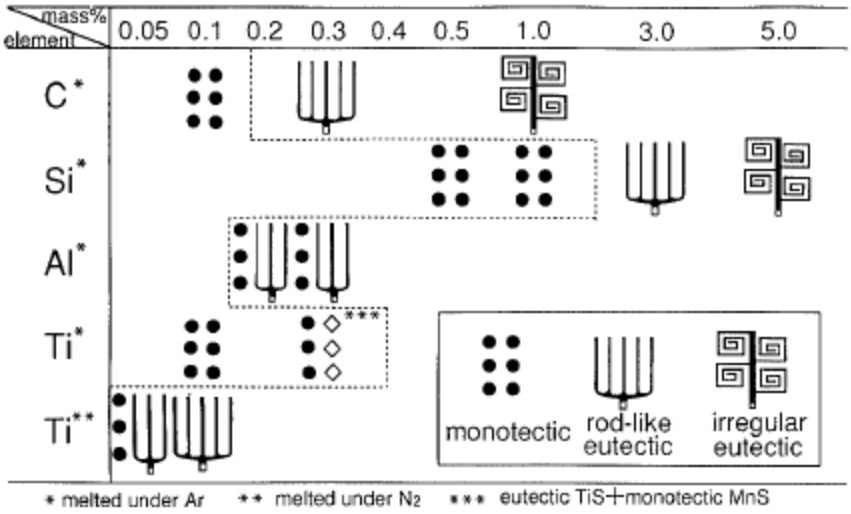

Figure 1.16. Influence of deoxidant addition on MnS morphology.[42]

1.3.5. Inclusions in FeMnAlC Steels. In FeMnAlC steels, the presence of high contents of alloying elements with high affinity with oxygen such as Mn, Al, Si, and carbon leads to complete removal of oxygen from solution early in the melting process and plenty of time for the inclusions to float and be removed from the liquid through the slag. Studies have reported on the presence of large MnO-Al_2O_3 bi-films which float out to the slag in short period of times.[25] However, when the steel is poured into the mold or during melt transfer operations, mixing with the air can cause formation of oxide bi-films that are entrapped within the casting and can seriously degrade toughness.

Endogenous oxides are a class of inclusions with a low impact on the mechanical properties of this steel. In the FeMnAlC system, the population of AlN inclusions is mainly controlled by the amount of dissolved nitrogen. The amount of MnS inclusions is controlled by the amount of sulfur in the steel as manganese levels are nominally 30wt%. Sulfur is introduced in the steel by the impurities in the alloying additions and is the

result of the ore location or manufacturing process of the alloys. Nitrogen is also present in the alloying additions and is also introduced in the steel from the atmosphere during melting and melt transfer operation. In a simplified approach, the maximum amount of nitrogen in solution in liquid steel in equilibrium conditions can be described by Eq. (4) partial pressure of nitrogen gas above the steel melt, p_{N_2}, the activity of dissolved nitrogen in the liquid steel, a_N, and the equilibrium constant of the dissolution reaction of nitrogen, K. The equilibrium constant, K, is related to the Gibbs free energy of dissolution of nitrogen and it can be calculated as in Eq. (5).[23]

$$\frac{a_N}{\left(p_{N_2}\right)^{1/2}} = K \tag{4}$$

$$\log K = \frac{-188}{T} + 2.76 \tag{5}$$

The actual amount of nitrogen in solution in the steel is also related to the presence of alloying elements that modify the activity of nitrogen in the liquid steel. In FeMnAlC steel any nitrogen present in solution will react with aluminum to form nitrides. A more useful equation was developed by Liu et al. for the prediction of AlN precipitation and the solubility limit of N and Al in the steel.[45] The equation takes into account the concentration of each alloying element and their interactions. Calculation of the solubility of nitrogen using Liu et al. method is shown in Figure 1.17. For a Fe-25.5%Mn-3.3%Al steel a maximum nitrogen in solution at 1372°C (1645 K) is only 13ppm.[45] Considering that typical FeMnAlC steels have around 9%Al, the amount of dissolved nitrogen in the melt could be much lower.

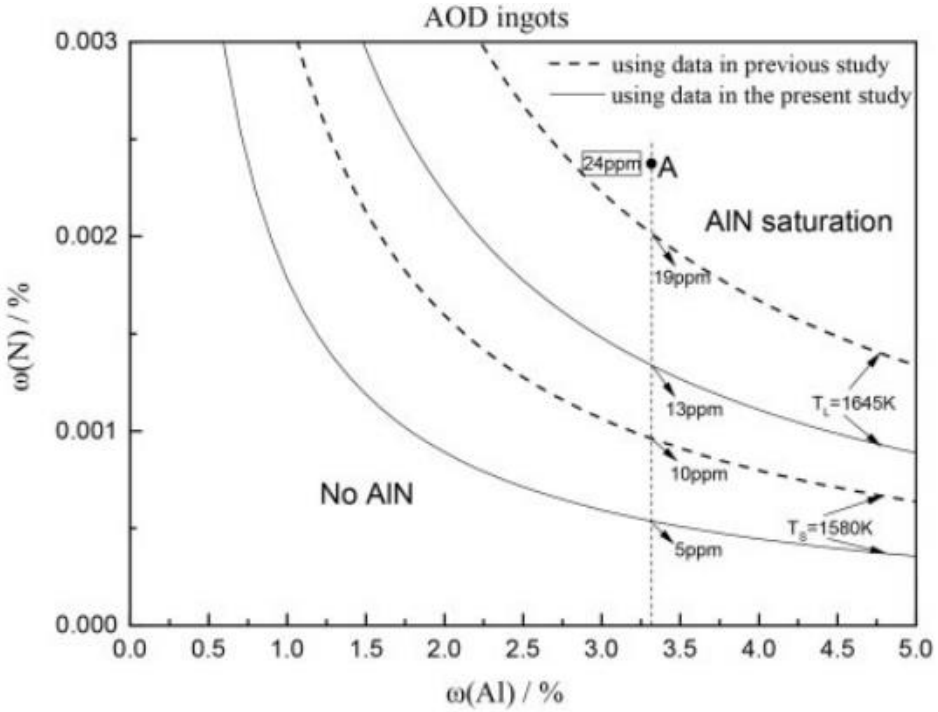

Figure 1.17. Amount of nitrogen present in equilibrium with aluminum at steelmaking temperatures in a Fe-25.5%Mn-xAl steel.[45]

AlN inclusions may not float to the slag as easily as the oxides and are often the predominant inclusion type. The inclusion population shown in Figure 1.18 was taken from a Fe-30Mn-9Al-0.9C-1Si steel.[17] AlN accounts for over 40% of the inclusions present. Some Mn, Al, and Si oxides were also identified. The steel had a low sulfur content and consequently few sulfides.[17]

Park et al. studied the formation of inclusions in FeMnAlC steels with different amounts of Mn and Al.[25] Secondary electron images of typical inclusion types observed in FeMnAlC steels are shown in Figure 1.19 for steels with nominal compositions of Fe-(10-20)Mn-(1-6)Al. The inclusions types were found to be Al_2O_3, AlN, $MnAl_2O_4$, AlON-Al_2O_3, MnS, AlN-MnS, and Al_2O_3-MnS. The MnS sulfide was shown to precipitate on

preexisting AlN and Al_2O_3. In their procedure, aluminum was added after Mn, which indicates that despite Mn being added first, the MnS precipitated after the AlN and thus the MnS sulfide does not precipitate upon addition of Mn but actually during cooling.

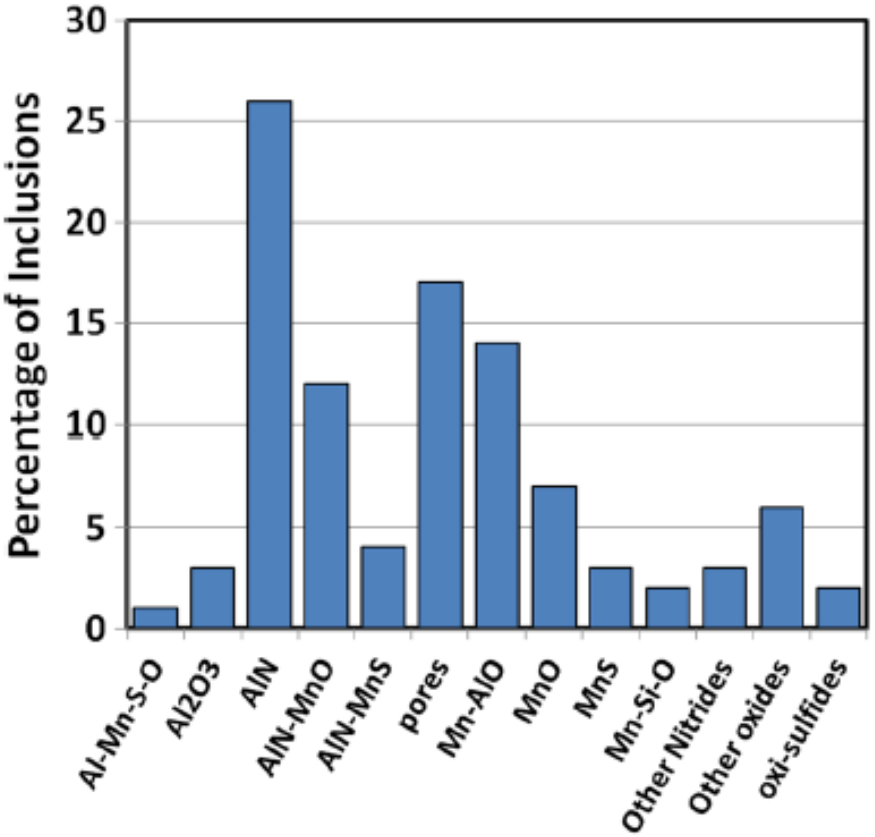

Figure 1.18. Inclusion population of a Fe-30Mn-9Al-0.9C-1Si steel recorded with an automated SEM.[17]

There are only a few studies available in the literature that attempt to correlate the inclusion population in FeMnAlC alloys to mechanical properties. However, reduced toughness has been linked with an increase in the population of AlN inclusions. AlN

inclusions are hard and angular, thus they serve as effective stress concentration sites and can lead to early fracture in sufficient quantities. Therefore, some research has been directed at clean melt practices that mitigate or reduce the population of AlN in FeMnAlC steels. The influence of AlN inclusions has been shown to be particularly detrimental to CVN impact toughness of FeMnAlC steels. Schulte et al. studied the effect of melt processing on inclusion formation and impact properties of a steels with a nominal composition of Fe-30Mn-9Al-0.9C-1Si as shown in Figure 1.20. It was observed that the CVN impact toughness at -40°C decreased from 38J to 20J when the amount of AlN increased from 4 to 50 particles/mm^2. The same study by Schulte et al. did not show a correlation between total inclusion density and notch toughness and indicated that the drop in toughness is mainly the result of the amount of AlN.[46]

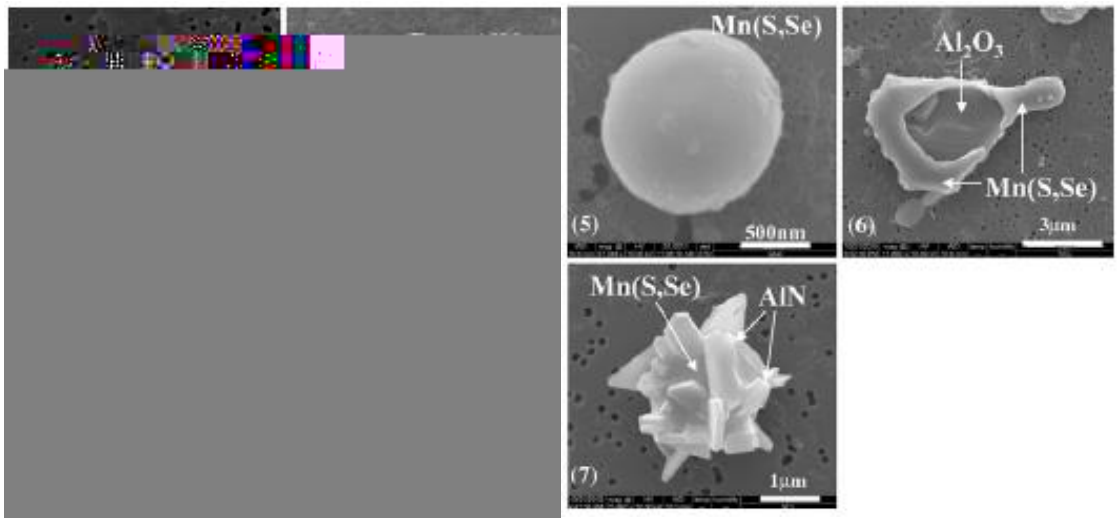

Figure 1.19. Secondary electron images of typical inclusion of the FeMnAlC steels observed in Fe-(10-20)Mn-(1-6)Al steels.[25]

1.4. THE CAST STRUCTURE

The microstructure of cast steel has a profound impact on the resulting physical and mechanical properties. The microstructure of the as-cast steel depends on the composition and segregation of alloying elements but also on the casting process and solidification conditions. Because of the high manganese and aluminum contents in the FeMnAlC steels, these alloys are difficult to cast using the continuous casting process. As a result, casting of these steels is accomplished by the ingot casting process as well as in near net shapes as castings in steel foundries.

1.4.1. The Ingot Structure. A schematic of the steelmaking process used to produce high manganese steels is shown in Figure 1.21. Production starts with melting in an induction or electric arc furnace. The material to be melted or, charge, consists mainly of high purity induction iron, electrolytic manganese or ferromanganese, graphite, ferrosilicon, and low alloy aluminum ingots. Scrap steel is also commonly used as an iron source in plain carbon and low alloy steels, however, the use of scrap as well as ferromanganese is limited in the production of FeMnAlC steels as these steels are sensitive to impurities like phosphorus. The molten metal is poured into either ingot molds or sand molds that are produced with a pattern with dimensions similar to the final product desired. After solidification, the sand mold is removed and the steel part is shot blasted and the risers and gating system is removed. The part is then cleaned and prepared for finishing steps that might be necessary such as machining and heat treatment.

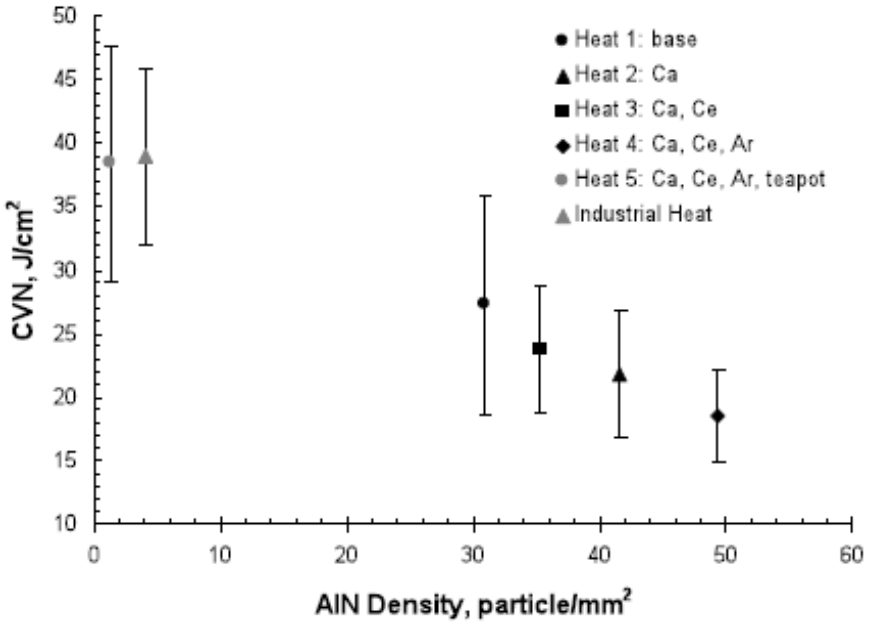

(a)

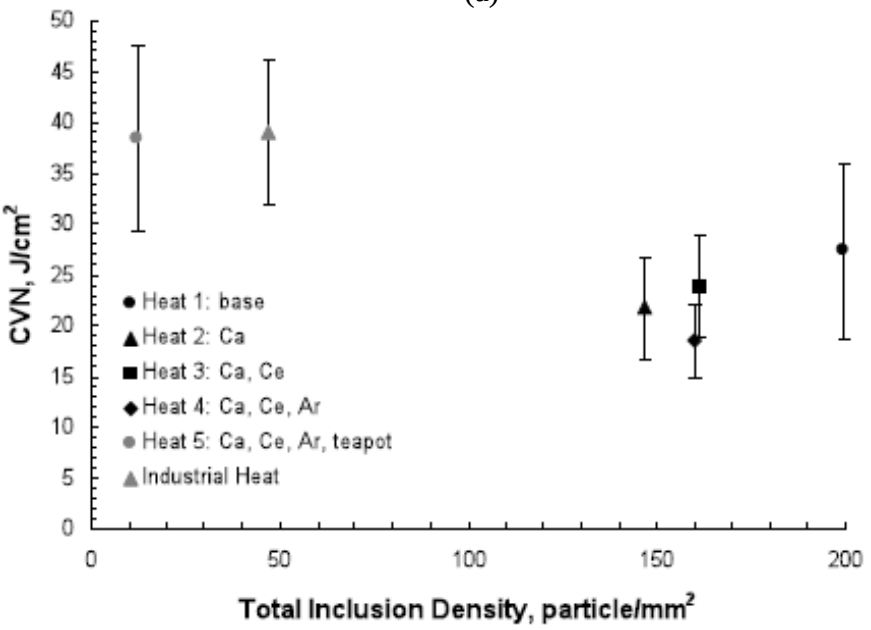

(b)

Figure 1.20. The correlation between CVN notch toughness and inclusion population in a nominal composition of Fe-30Mn-9Al-0.9C-1Si suggests that (a) CVN is inversely proportional to AlN density. (b) A strong correlation between notch toughness and the total inclusion density was not observed. Notch toughness was evaluated at -40°C for specimens aged at 530°C to a hardness of approximately 302 BHN [46]

The sand casting process has typically much lower cooling rates that the continuous casting processes which leads to excessive grain growth during solidification. Upon solidification, the grain growth and consequently the final microstructure occurs differently in each part of the casting, shown in Figure 1.22, and is classically separated into three zones: (1) chill, (2) columnar and (3) equiaxed.

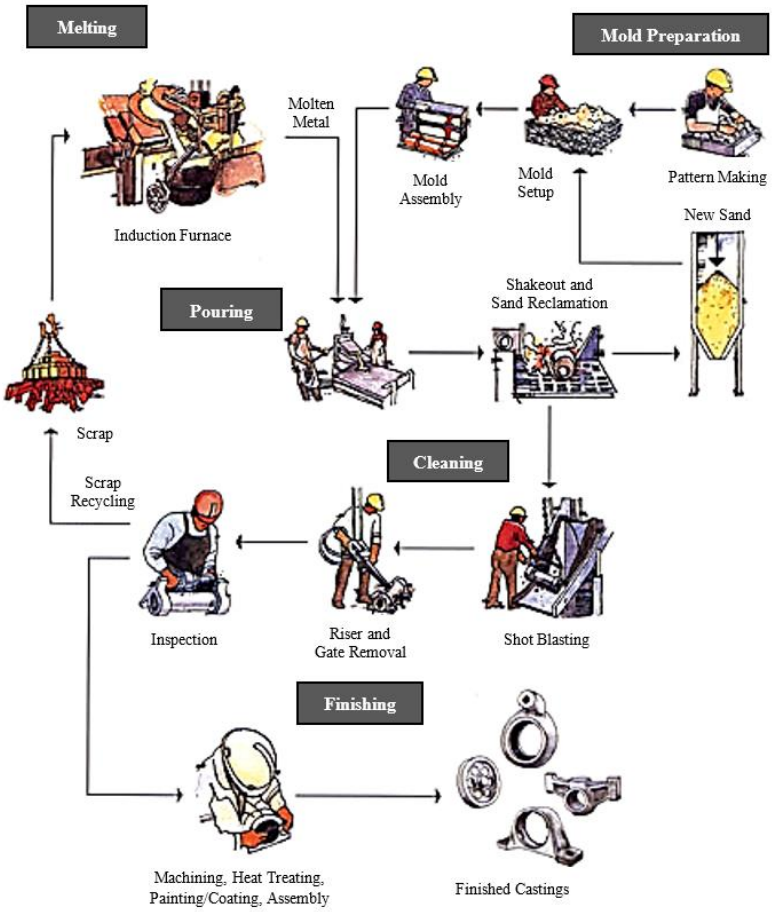

Figure 1.21. Conventional steelmaking, molding, casting, cleaning and finishing processes in a steel foundry.[47]

The chill zone is located next to the mold walls where there is a fast cooling rate with high undercooling leads to heterogenous nucleation of randomly oriented grains on the mold wall. The chill grains that have preferred orientations along the opposite direction of heat flow will grow faster than other chill grains. In cubic metals this is the <100> direction. Those grains grow parallel to the heat extraction direction and create the columnar zone.[49] The columnar zone is characterized by large grains with low angle grain boundaries and a high degree of anisotropy. The columnar zone extends until the thermal gradient is diminished to the point where heterogeneous nucleation sites become activated in the last liquid producing an equiaxed zone of randomly oriented grains that nucleate from the liquid.

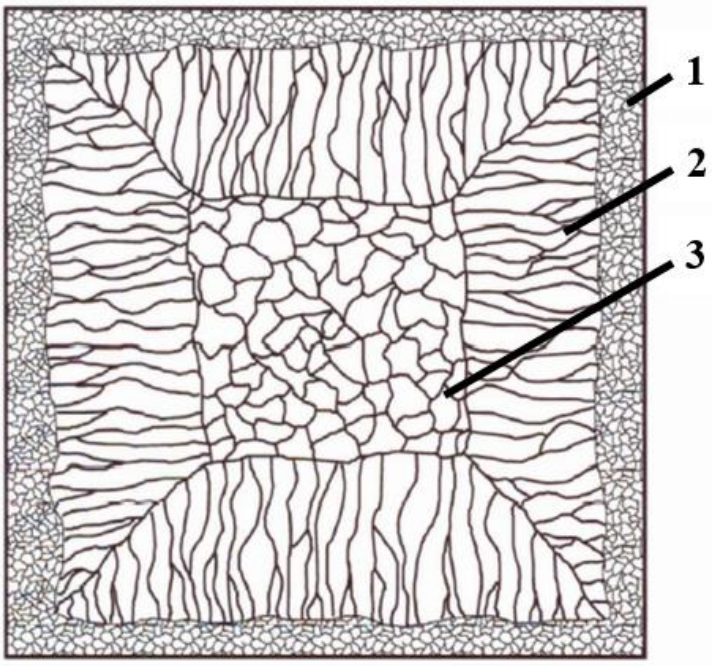

Figure 1.22. Grain structure of a typical cast steel ingot microstructure consisting of a (1) chill zone, (2) columnar zone, and (3) equiaxed zone[48]

The nucleation and growth in the equiaxed zone can occur by two methods: from the fragmented solid nuclei that are broken off from the chill zone or from new solid nuclei that are formed if enough undercooling is present in the last liquid. During the growth of the solid nuclei, temperature variation can lead to the fragmentation of the solid crystals originated in the chill zone. These grains may survive and grow new solid grains from the liquid. The fragmentation of grains can be increased by promoting metal flow inside the solidifying microstructure. This creates temperature fluctuations around the growing dendrites which leads to weakening and fragmentation. Convection currents in the liquid help to transport the fragmented nuclei to the middle of the casting. In addition, low superheat during the pouring of the material will assist in increasing the stability of the nuclei.[49,50]

The type of the solidification structure is also related to the temperature gradient imposed on the liquid, G, and the growth rate of the solid, R. The Figure 1.23 shows the relationship between G, R and the type of solidification structure formed. The product GxR is equivalent to the cooling rate, with higher cooling rates refining the as-cast structure. The ratio of G/R has been used by some authors to determine the morphology of the solidification structure. When the growth rate is much higher than the temperature gradient, the solidification structure is dendritic, as the ratio decreases it changes to columnar dendritic, then to cellular and finally to a planar interface. Finer structures are achieved by increasing the cooling rate.[49]

1.4.2. Nucleation Theory. Classic nucleation theory states that solidification starts with the metastable formation of a conglomerate of atoms in the liquid steel due to thermal fluctuations in the melt that form embryonic nuclei. For the nuclei to be stable

and grow, they must reach a critical radius size. The volumetric free energy for solid formation from the liquid is always negative below the solidification temperature. However, the creation of a solid nucleus requires the formation a solid/liquid interface or surface and this always has a positive contribution to the total free energy of solidification. The stability of a nuclei is thus dependent on the balance between the decrease in volumetric free energy change for the formation of the solid, ΔG_v, and the increase in the surface free energy to the formation of the interface, γ_{SL}. For the homogenous nucleation of a spherical solid nucleus from a pure liquid, the overall change in the free energy, ΔG_{hom}, is represented in Eq. (6), where the volumetric term, $\Delta G_{v,}$ is multiplied by the volume of the nuclei and the surface energy of the solid/liquid interface is multiplied by the area of the nuclei assuming a spherical morphology.

$$\Delta G_{Hom} = \frac{4}{3}\pi R^3 \Delta G_V + 4\pi R^2 \gamma_{SL} \quad (6)$$

In most application, homogeneous nucleation rarely occurs because the presence of solid particles in the liquid, nonmetallic inclusions, and the mold wall itself which can serve as a preferential surfaces for nucleation. These heterogeneous nucleation sites effectively decrease the activation energy for nucleation as well as the amount of undercooling required to start the nucleation event. Undercooling is defined as the temperature below the liquidus temperature that is needed to start the nucleation process. For homogeneous nucleation, the undercooling needed to start nucleation for pure Fe can be as high as 420K.[52] For heterogeneous nucleation, the undercooling necessary is in the order of tens of degrees and can be a fraction of a degree in a system with the presence of solid particles with high nucleation potential.[52]

When a solid particle is present in the liquid, the surface energies involved in the formation of a solid embryo from the liquid will be modified by the presence of new interfaces. Figure 1.24 represents the different interfaces that will appear from the heterogeneous nucleation.

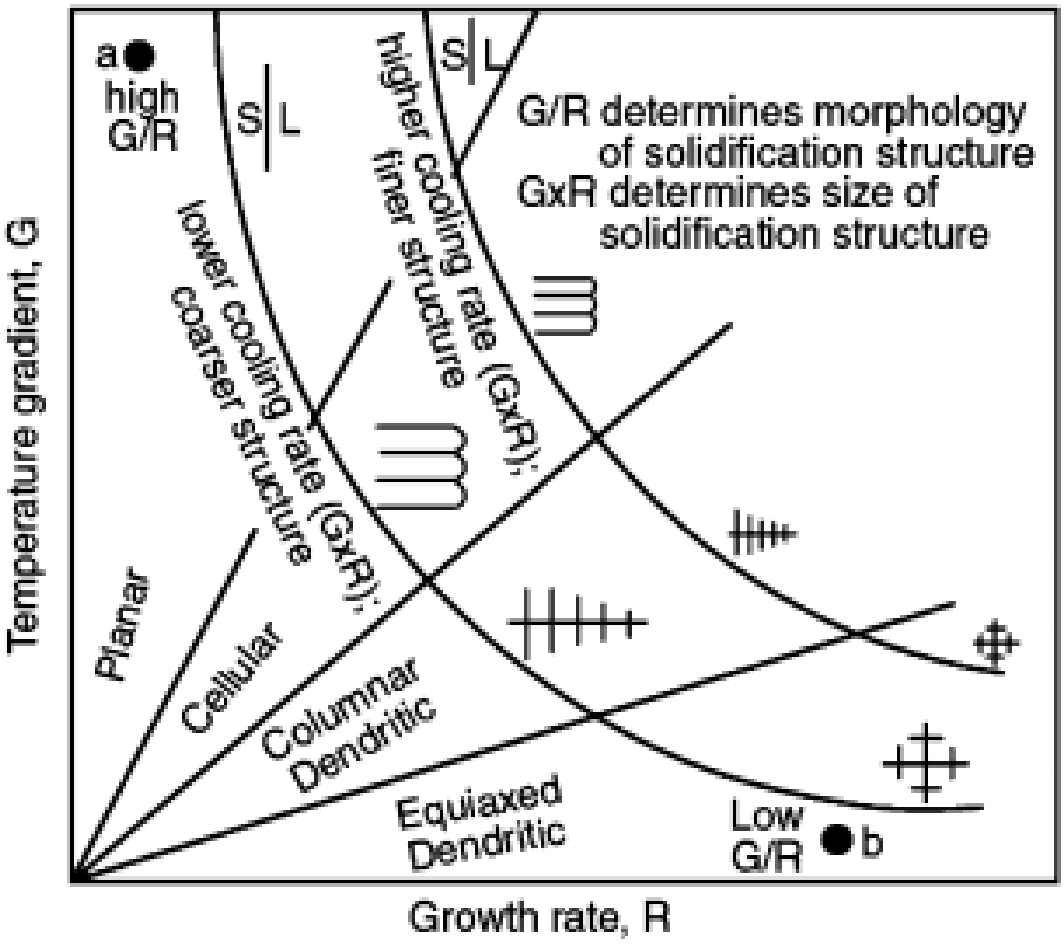

Figure 1.23. Diagram of solidification morphology according to the temperature gradient and growth rate.[51]

The relationship between these interfacial energies are described by Young's equation and they are related by the wetting angle, θ, between the nucleating solid and the heterogeneous substrate surface. The Gibbs free energy for heterogeneous nucleation can then be described by the ΔG_{hom} and the wetting angle of the nucleating particle. The relationship is described by Eq. (7) and assumes a spherical cap shape of the nucleating solid particle. The $f(\theta)$ value ranges from 0 to 1, meaning that heterogeneous nucleation will be encourage by a low wetting angle. When the contact angle is 180°, $f(\theta)$ is equal to one and no wetting takes place, $\Delta G_{het} = \Delta G_{hom}$.[52]

$$\Delta G_{het} = \Delta G_{hom} * f(\theta), \text{ where } f(\theta) = (2 + cos\theta)\frac{(1-cos\theta)^2}{4} \quad (7)$$

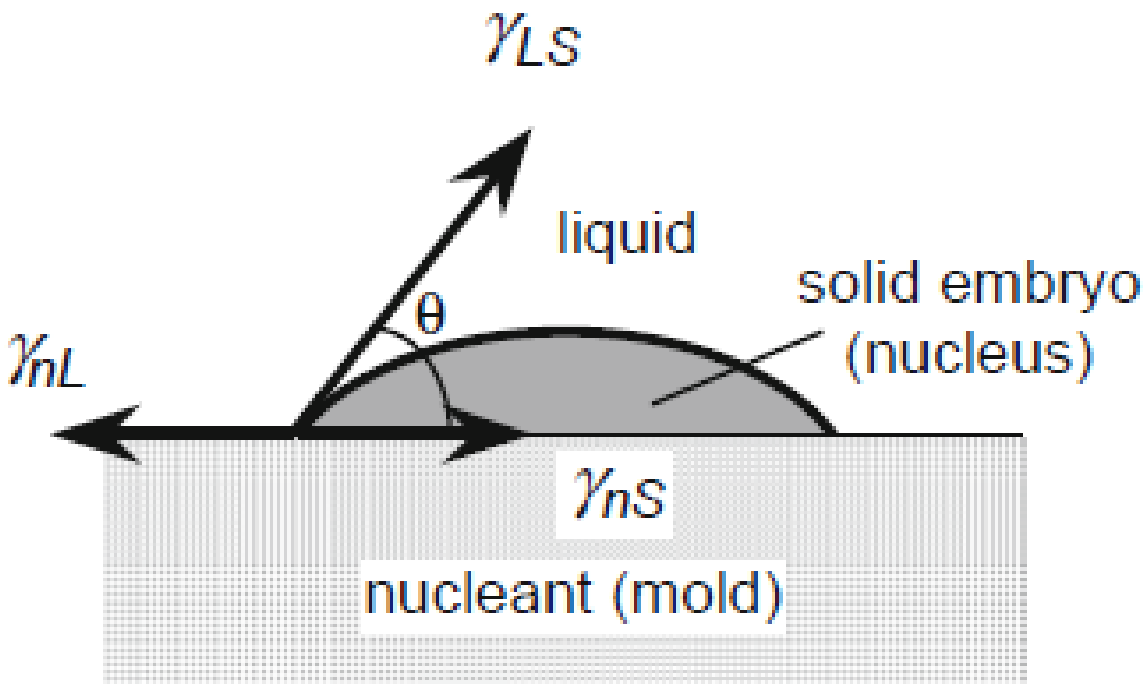

Figure 1.24. Interfacial energies for the heterogeneous nucleation of a solid particle from the liquid on the surface of a nucleant particle in contact with the liquid.[52]

1.4.3. Grain Refinement of Steels. Grain refinement methods using an inoculation process to create heterogeneous nucleation sites for the solidifying metal is commonly used to control of the size and morphology of the solidification structure. This process leads to the improvement both strength and toughness, and a decrease in the amount of segregation and microporosity. Grain refinement is a well-stablished foundry practice refining aluminum and magnesium-alloys, however, knowledge and applications of these techniques for steels are quite limited. It has been shown that a fine equiaxed grain size can contribute to the castability, decrease in macro and microsegregation, and improvement in strength, ductility, and toughness of the material.[50,53,54] The segregation tends to occur in the liquid between grains, for a smaller grain size there is a higher density of grain boundaries and segregation spread more evenly over the microstructure of the casting, decreasing the overall micro and macrosegregation.

The improvement in strength and ductility is related to the interaction between dislocations and grain boundaries. Deformation occurs by shear of atoms along specific slip planes. A decrease in the grain size and in the number of high angle grain boundaries leads to a decrease in the mean free path of dislocations and a higher yield strength. In addition, decreasing the grain size leads to a higher amount of grain boundary area and therefore an increase in the fracture energy because a propagating crack must continuously reorient itself when it encounters a high angle grain boundary. Grain boundaries also offer resistance to dislocation motion, leading to pilling up of dislocations and an increase of the necessary stress to move the dislocation across the boundary. This ultimately increases the strength of the material. The effect of grain refinement on the yield strength (σ_Y) of steels has been demonstrated by Hall-Petch

relationship in terms of the average grain diameter (d), Peierls-Nabarro stress (σ_o), and a grain boundary hardening constant (k_y), in Eq. (8).

$$\sigma_Y = \sigma_0 + k_y d^{-1/2} \tag{8}$$

Grain refinement can be achieved by different methods. For steels, the most common way of grain refinement by recrystallization during deformation at high temperature and is applicable only for hot rolling and forging processes. Another method is by polymorphic solid-state transformations that occur during heat treatment or by refining the as-cast grain size by increasing the nucleation rate during solidification of the liquid metal. For FeMnAlC steels, the material is currently produced as net shaped castings or ingots for further hot rolling or forging into useful shapes. Additionally, there are no polymorphic phase transformation that occur during heat treatment that can refine the austenitic grain size. Therefore, the use of inoculation methods to refine as-cast structure during solidification is the most viable method for grain refinement.

Grain refinement of the as-cast structure is accomplished by increasing the nucleation rate and is done with the addition of engineered solid particles or dispersoids to the liquid. The dispersoids act as nucleation sites during the beginning of solidification. A large number of dispersoids distributed within the liquid creates a large number of randomly oriented nuclei that then grow in the liquid until they impinge upon themselves giving a very fine final grain size. The dispersoid works as a nucleation site by decreasing the Gibbs free energy for nucleation of a solid particle in the liquid as previously described in Eq. (7). The inoculant particle or dispersoid is thus more efficient if it has a low wetting angle with the nucleating solid. For a dispersoid to be considered a good inoculant for the steel, it should have a low wetting angle with the nucleating solid.

The dispersoid should also be solid at or above the liquidus temperature of the steel, it must be thermodynamically stable. The dispersoid should also expose a large area to the liquid to favor nucleation on its surface. Furthermore, to appropriately refine the microstructure, a dispersoid needs to have a high volumetric density and be homogeneously dispersed in the liquid to yield a large number of nuclei.[52]

The nucleation rate for heterogeneous nucleation (I_{Het}) has been derived in Eq. (9) in terms of number of surface atoms of nucleation sites per unit volume (n_a), the Gibbs free energy for heterogeneous nucleation (ΔG^*_{Het}), the nucleation temperature (T), Boltzman's constant (k_B), and a vibrational factor (υ). An effective grain refiner will therefore have a low surface interfacial energy between the solid and the nucleating particle and a fine dispersion and to maximize surface area for nucleation.[52]

$$I_{Het} = n_a v \, exp\left[-\frac{\Delta G^*_{Het}}{k_B T}\right] \tag{9}$$

The energy barrier for nucleation goes to zero for a complete wettability, $\theta = 0$, of the nucleating solid on the substrate. Young's equation $\gamma_{nL} = \gamma_{nS} + \gamma_{LS} \cos\theta$ shows that it occurs for low surface energy between the nucleant and the substrate. In reality, measurements of the surface energy between two phases is very difficult to be determined and a similar crystal structure with a low lattice disregistry is taken as a reference to identify potential inoculants. The lattice disregistry can be calculated by the Bramfitt's planar lattice disregistry model, in Eq. (10), as an indicator for low interfacial energy. Values below 12% and 6% are used by different authors as a reference value.[55-59]

$$\delta_{(hkl)_n}^{(hkl)_s} = \sum_{i=1}^{3} \frac{1}{3}\left[\frac{\left|\left(d_{[uvw]_s^i}\, cos\gamma\right) - d_{[uvw]_n^i}\right|}{d_{[uvw]_n^i}}\right] x\ 100\% \qquad (10)$$

In Eq. (10), $(hkl)_s$ is a low-index plain of the substrate, $[uvw]_s$ is a low-index direction in $(hkl)_s$, $(hkl)_n$ is a low-index plane in the nucleated solid, $[uvw]_n$ is a low-index direction in $(hkl)_n$, $d_{[uvw]n}$ is the interatomic spacing along $[uvw]_n$, $d_{[uvw]s}$ is the interatomic spacing along $[uvw]_s$, and γ is the angle between $[uvw]_s$ and $[uvw]_n$.

For a Fe – 30%Mn – 9%Al – 1%C – 1%Si, the lattice parameter is a_γ was the experimentally determined to be 0.3686nm as given in Eq. (11).[4]

$$a_\gamma = 0.3570 + 0.000065\ \%Mn + 0.00095\ \%Al + 0.0021\ \%C - 0.00101\ \%Si \qquad (11)$$

The inclusions that can be considered potential grain refiners for FeMnAl were identified by calculating lattice disregistry. The inclusions considered were chosen from the inclusions most commonly studied as grain refiners for steel, common inclusions in the FeMnAl system, and inclusions recently developed for grain refinement. They are $AlCeO_3$, Al_2MgO_4, AlN, CeO_2, CeS, La_2O_3, La_2SO_2 MgO, NbC, NbN, TiC, and TiN. The lattice misfit at room temperature between the austenite and ferrite and the listed inclusions was calculated using Eq. (10). The composition of Fe – 30%Mn – 9%Al – 1%C – 1%Si was used as a reference for the lattice parameters. The lattice misfit was calculated for three directions on a specific plane of each crystal structure and results are listed in Table 1.2 for austenite and Table 1.3 for ferrite.

The calculations of lattice disregistry show a more favorable refinement of δ-ferrite than γ-austenite. For austenite the only inclusion below the 6% threshold was $AlCeO_3$. In contrast for δ-ferrite the only inclusion that had disregistry above 12% was CeO_2. This a good indicator that refinement of austenite is more complicated than

austenite. A study of grain refinement in stainless steels by addition of TiN observed that refinement of fully austenitic alloys was less efficient than that for ferritic steels, however, refinement was achieved in both situations.[60]

There are numerous studies on grain refinement during inoculation for steels, but due to the difference in compositions and different phases forming at nucleation, ferrite and/or austenite, the same refiner might not work for every steel. Steels with primary solidification as ferrite and as austenite might both be a good reference for FeMnAlC steels since different alloys of FeMnAlC are usually fully austenitic or dual-phase. In the FeMnAlC steels system, research is limited to a single study on the use of cerium for refinement in a Fe-30Mn-9Al-1Si-0.9C-0.5Mo nominal composition steel.[66] This study used a Ce-based inoculant for grain refining, achieving one order of magnitude of refinement with 0.1% Ce. Inclusion analysis showed that cerium formed complex inclusions consisting of phosphides, oxides, and sulfides.[67] The Hadfield steels have high manganese additions and carbon additions and have austenitic solidification. Successful trials were made with Ce levels above 0.05%. In contrast, addition of Ti for targeted formation of Ti(C,N) did not produce grain refinement.[64,68]

In peritectic low alloyed steels, with solidification as primary δ-ferrite followed by a peritectic reaction, studies explored the use of Nb(C,N) and Ti(C,N), for grain refinement of both δ-ferrite and austenite. Ohno et al. showed that Nb addition of 0.5% reduced austenite grain size by one order of magnitude, increasing significantly the equiaxed grain zone and removing completely the coarse columnar grain zone.[36] In another study by the same authors, Ti additions from 0.12 to 0.17% suppressed completely the columnar zone and refined grain austenite grain size.[37]

Steel systems that solidify as primary austenite should work as a nice base for development of a grain refiner for the austenitic FeMnAl steels. For a 316 austenitic stainless steel, NbC was evaluated by addition of Fe – 20%Nb – (2-3)%C. Results showed that additions of 3%Nb with no incubation time after additions were able to reduce the grain size by one order of magnitude.[69] The use of Ce additions as grain refiner for austenitic stainless steels was evaluated by addition of a grain refiner in the form of a Mn-Si-Cr-Ce alloy and presented grain refinement for Ce contents between 0.3%-0.5%.[57] Refinement was enhanced for decreasing superheat.[57] Other studies identified $AlCeO_3$ as the desirable form of the cerium inclusions that promote heterogeneous nucleation of austenite during solidification.[70,71]

The above discussion demonstrates the various ways that the inclusion population can be engineering to improve the mechanical properties of FeMnAl steels. Control of inclusions population, especially the AlN, is a possibility for improvement of properties. Inclusion engineering for grain refinement of as-cast structure can further improve mechanical properties, decrease segregation, and decrease the size of porosity.

Table 1.2. Lattice misfit between austenite and selected nonmetallic inclusions at room temperature.

Inclusion	Lattice Parameter (nm)	Face	[uvw] Precipitate	[uvw] Substrate	δ%
TiC	0.4327[59]	(100)TiC//(100)γ-Fe	[010] [110] [001]	[010] [110] [001]	14.8
TiN	0.424[59]	(100)TiN//(100) γ-Fe	[010] [110] [001]	[010] [110] [001]	13.1
TiO_2	a-0.4592 c=0.2959[59]	(110)TiO_2//(100) γ-Fe	[100] [111] [110]	[010] [110] [001]	14.7
$AlCeO_3$	0.3767[61]	(111)$AlCeO_3$//(111) γ-Fe	[010] [110] [001]	[010] [110] [001]	3.4
CeO_2	0.5411[61]	(100)CeO_2//(100) γ-Fe	[[010] [110] [001]	[010] [110] [001]	32.9
CeS	0.5778[61]	(100)CeS//(100) γ-Fe	[010] [110] [001]	[010] [110] [001]	36.2
La_2O_3	a=0.393, c=0.613[62]	(0001)La_2O_3//(100) γ-Fe	$[\bar{1}\bar{2}\bar{1}\bar{0}]$ $[10\bar{1}0]$[$\bar{2}110$]	[010] [031] [001]	16.7
La_2SO_2	a=0.403, c=0.693[62]	(0001)La_2SO_2//(100) γ-Fe	$[\bar{1}\bar{2}\bar{1}\bar{0}]$ $[10\bar{1}0]$[$\bar{2}110$]	[010] [031] [001]	18.7
NbC	0.4467[61]	(100)NbC//(100) γ-Fe	[010] [110] [001]	[010] [110] [001]	17.5
NbN	0.4391[63]	(100)NbN//(100) γ-Fe	[010] [110] [001]	[010] [110] [001]	16.1
MgO	0.4218[61]	(100)MgO//(100) γ-Fe	[010] [110] [001]	[010] [110] [001]	12.6
Al_2MgO_4	0.404[64]	(100)Al_2MgO_4//(100)γ-Fe	[010] [110] [001]	[010] [110] [001]	8.8
Austenite	0.3686[65]	-	-	-	-

Table 1.3. Lattice misfit between ferrite and selected nonmetallic inclusions at room temperature.

Inclusion	Lattice Parameter (nm)	Face	[uvw] Precipitate	[uvw] Substrate	δ%
TiC	0.4327[59]	(100)TiC//(110)δ-Fe	[001] [011] [0$\bar{1}$1]	[$\bar{1}$10] [001] [$\bar{1}$11]	6.4
TiN	0.424[59]	(100)TiN//(110) δ-Fe	[001] [011] [0$\bar{1}$1]	[$\bar{1}$10] [001] [$\bar{1}$11]	4.4
TiO_2	a=0.4592, c=0.2959[59]	(110)TiO_2//(100) δ-Fe	Ref. 9	Ref. 9	8.5
$AlCeO_3$	0.3767[61]	(100)$AlCeO_3$//(110) δ-Fe	[001] [011] [0$\bar{1}$1]	[$\bar{1}$10] [001] [$\bar{1}$11]	7.6
CeO_2	0.5411[61]	(100)CeO_2//(111) δ-Fe	[001] [011] [0$\bar{1}$1]	[$\bar{2}$10] [$\bar{1}$10] [$\bar{1}$01]	13.9
CeS	0.5778[61]	(100)CeS//(111) δ-Fe	[001] [011] [0$\bar{1}$1]	[$\bar{2}$10] [$\bar{1}$10] [$\bar{1}$01]	7.7
La_2O_3	a=0.393, c=0.613[62]	(0001)La_2O_3//(100) δ-Fe	[1210] [1100] [2110]	[011] [121] [001]	3.1
La_2SO_2	a=0.403, c=0.693[62]	(0001)La_2SO_2//(100) δ-Fe	[1210] [1100] [2110]	[011] [121] [001]	2.2
NbC	0.4467[61]	(100)NbC//(110) δ-Fe	[001] [011] [0$\bar{1}$1]	[$\bar{1}$10] [001] [$\bar{1}$11]	9.3
NbN	0.4391[64]	(100)NbN//(110) δ-Fe	[001] [011] [0$\bar{1}$1]	[$\bar{1}$10] [001] [$\bar{1}$11]	7.7
MgO	0.4218[61]	(100)MgO//(110) δ-Fe	[001] [011] [0$\bar{1}$1]	[$\bar{1}$10] [001] [$\bar{1}$11]	3.9
Al_2MgO_4	0.404[64]	(100)Al_2MgO_4//(110)δ-Fe	[001] [011] [0$\bar{1}$1]	[$\bar{1}$10] [001] [$\bar{1}$11]	0.3
δ-ferrite	0.2866[59]	-	-	-	-

PAPER

I. UNDERSTANDING THE ROLE OF INCLUSIONS ON THE DYNAMIC FRACTURE TOUGHNESS OF HIGH STRENGTH LIGHTWEIGHT FeMnAl STEELS

Rairu Vaz Penna, Laura N. Bartlett, Trevor Constance

Missouri University of Science and Technology
Materials Science & Engineering Dept.
1400 N Bishop, Rolla, MO, U.S.A., 65409

Keywords: high manganese steels, sulfides, nonmetallic inclusions, fracture toughness

ABSTRACT

High manganese lightweight steel alloys in the Fe-Mn-Al-C system are promising alternatives to quenched and tempered Cr and Mo steels for transportation and military applications. The understanding of nonmetallic inclusion formation and their effect on the mechanical properties is of extreme importance for further alloy development. Sharp and brittle AlN forms prior to the liquidus and has been shown to decrease notch toughness. Controlled additions of sulfur may promote soft and globular MnS that precipitates around AlN during solidification, thus mitigating their detrimental effect. The effect of controlled sulfur additions from 0.004 to 0.042%S were studied in a Fe – 30%Mn – 9%Al – 1%Si – (0.9-1.2)%C –0.5%Mo steel. The main inclusions observed were AlN, MnS, and AlN cored - MnS. Impact tests in the solution treated conditions and in aged to hardness of 329-340 HBN, showed that absorbed energy is a function of the overall

inclusion density in solution treated condition. In aged specimens, same was true only for steels with 0.9% carbon, above 1%C the toughness was below 15J for any sulfur content.

1. INTRODUCTION

The need to reduce weight in the transportation industry, as well as in other areas such as the military, created a demand to develop lightweight materials with high strength, good ductility, and high energy absorbing capabilities. In this perspective the steels from the Fe-Mn-Al-C system have presented promising combinations of high strength and toughness. Fe-Mn-Al-C steel castings with a composition of Fe – 30%Mn – 9%Al – 0.9%C – (1-1.4)%Si have been shown to exhibit tensile strengths over 1 GPa and dynamic fracture toughness values of over 400 kJ/m^2 after age hardening.1 The Fe – 30%Mn – 9%Al – 1%C nominal composition alloy has a total weight reduction of 15% when compared to conventional high strength steels.[1]

The fracture behavior and toughness of Fe-Mn-Al-C steels are mainly dependent on composition, heat treatment, and steel cleanliness. For steel with a composition of Fe - 30%Mn - 9%Al – (0.78-1.56)%Si - 0.9%C, a yield strength and tensile strength of 616 and 698 MPa with 17% elongation have been reported in the as-cast condition. Solution treatment for 2h at 1050°C, increases the elongation to up to 70% but it decreases the yield strength to values close to 500MPa. By aging, the yield strength and tensile strength can increase to over 1 GPa, and elongation will be decreased to values from 5 to as much as 35% depending on time and temperature.[2-4]

Aging greatly increases strength but decreases ductility and toughness. In the solution treated condition, the Charpy V-Notch breaking energy was reported to be as high as 214 J for a steel with a nominal composition of Fe - 30%Mn - 9%Al – 1%Si - 0.9%C (0.001%P).[5] However, the breaking energy for this steel decreased to 92 J when age hardened at 530°C to 300 HBN and 38 J after aging to 340 HBN. Bartlett et al.[1] reported on the dynamic fracture toughness (DFT) values of these steels. At a nominal composition of Fe - 30%Mn - 9%Al – 1.56%Si - 0.9%C DFT values as high as 700 kJ/m^2 were recorded for the solution treated castings. After aging to a hardness of 318 and 375 HBN, the dynamic fracture toughness decreased to 265 and 144 kJ/m^2 respectively. However, when compared with cast AISI 4130 quenched and tempered steel with 350 HBN and a DFT of 94kJ/m^2, it is seen that the 4130 steel has a lower toughness then Fe – Mn – Al – C steel at equivalent hardness.

1.1. NONMETALLIC INCLUSIONS IN Fe-Mn-Al-C ALLOYS

Previous studies of nonmetallic inclusions in Fe – Mn – Al – C steels have identified the main inclusions present in these alloys as manganese sulfides and aluminum nitrides. The presence of different oxides was also seen in a few studies, mostly Al_2O_3, MnO, $MnAl_2O_4$.[4,6-8] Small amounts of Ti(C,N), from both residuals in charge material as well as from the deoxidation process have also been observed.[6,7] These inclusions exist as either as single inclusions or complex inclusions that sometimes contain all types.[4]

A few studies have tried to model how Charpy V-notch breaking energy (CVN) and dynamic fracture toughness (DFT) vary according to inclusion population and types

in these alloys. Schulte et al.[9] compared the CVN of steels with a nominal composition of Fe – 30%Mn – 9%Al – 0.9%C – 1%Si under different deoxidation practices, and observed no relation with total nonmetallic inclusion average diameter nor total inclusion density. However, at – 40°C, the CVN decreased from 38 J to below 20 J when AlN density increased from 4 to 50 particles/mm^2. The same was observed at room temperature for a steel with nominal composition of Fe – 30%Mn – 9%Al – (0.9-1.6)%C – 0.9%Si.

Dynamic fracture toughness describes the high strain rate dependence of a material in the presence of a sharp crack or flaw and has been shown to be dependent on the size, shape, number, and distribution of non-metallic inclusions in a variety of high strength steels.[4,6,9] It has been observed that in Cr-Mo quenched and tempered steels deoxidized with titanium, the DFT decreases by about 60kJ/m^2 when compared with Al deoxidized steels at equivalent total inclusion contents.[4] Therefore, additionally to the effect of inclusion density on the DFT, the presence of brittle inclusions like Ti(C,N) lowers toughness even further. The same behavior may be expected from hard and angular AlN in Fe-Mn-Al-C steels. In a recent study of a Fe - 30%Mn – (9-9.5)%Al – 0.95%Si – (0.9-1.05)%C DFT was shown to decrease from 380 to 60kJ/m^2 for AlN density increasing from 10 to 40 particles/mm^2.[6] The DFT also showed linear relationship to volume fraction ($V_f^{-1/3}$) and inclusion spacing. The types and amounts of nonmetallic inclusions play, thus, an important role in the properties of the Fe-Mn-Al-C steels. Special attention has been given to AlN as it has been proposed by more than one study to have strong effect the toughness.[4,6,9]

The AlN inclusions are hard and brittle and present faceted morphology in steels, this leads to stress concentration in corners. In addition, the AlN inclusions have a lower thermal expansion coefficient than the austenite and this difference leads to the development of stress in the austenite surrounding the AlN during cooling.[10-12] The amount of AlN must be then minimized or modified to mitigate these detrimental effects. One method is to control nitrogen using vacuum induction melting however, this is an expensive method and not possible for many foundries. Another option to diminish the detrimental effect of AlN would be to limit the contact of AlN and the matrix. This can be achieved by coprecipitation of a soft globular inclusion such as MnS on the surface of AlN. To be effective at coating AlN, the inclusion must nucleate at lower temperatures than AlN and have a low surface energy with it. Manganese sulfides are soft easily deformable inclusions, with similar thermal expansion coefficient to the matrix, therefore, potentially able to counter the effect of AlN.

The MnS inclusions can be found in different morphologies. Sims divided into three types: globular (Type I), dendritic/eutectic films (Type II), and faceted (Type III).[13] The type of the sulfide formed is an important factor in its effects to the materials mechanical properties. It is widely accepted that sulfide films forming on grain boundaries are the most detrimental.[14] Even though Type I and Type III have similar behavior, crack formation on the edges on the angular Type III sulfides have been observed.[15] A review on the effect of Type I sulfides in bearing steels and showed that manganese sulfide has no effect on yield strength, ultimate tensile strength, and work hardening exponent.[16] However, this relationship is not observed in wrought steels. The neutrality of sulfides on this properties was explained by the absence of thermal stress

around MnS inclusions and coating of hard inclusions. In fatigue loading, larger inclusions are more detrimental to the properties, the same is true for hard and brittle inclusions when compared to deformable ones. The role of sulfide inclusions on toughness is more complex. Studies on sulfides in AISI 4340, 4130, and 300M steels have shown that manganese sulfides decrease the plane strain fracture toughness, KIC, by approximately 30% with just 0.015%S added. However, this effect was decreased by controlling inclusion morphology to lower aspect ratios, by controlled rolling.[16]

Different explanations for the morphology and formation mechanism for MnS inclusions have been proposed by different authors. Herring[17] attributes the deoxidation method as the primary factor responsible for sulfide morphology. In silicon semi-killed steels, Type I sulfide inclusions are predominant. As the active oxygen content is reduced with more effective deoxidation such as in aluminum-killed and Ti deoxidized melts, the sulfide morphology transitions into Type II, and III morphologies. In a study by Oikawa et al[18] of high sulfur steels (%S>1), they observed the sulfide morphology transitioning from Type I to II then to III by increasing Si and Al to up to 5%, in steels with nominal composition Fe - 2.5%Mn – 1%S - (2-5)%Al - (2-5)%Si. These high Al and Si levels could be considered as over-killing the steel. In fact, Marich and Player[19] proposed that low dissolved oxygen (<10ppm) is the sole reason for Type III formation. Similarly, Liu et al[7]studied sulfide formation in Fe-Mn-Si-Al TWIP steels with low total oxygen (5ppm) and observed Type III manganese sulfides when the inclusions were not modified by Ca, and Type I when modified. Bigelow and Flemings[20] extensive research on sulfide inclusions has data indicating that for sulfur levels up to 0.2%, both

carbon and silicon lead to the formation of Type III inclusions. For even higher sulfur content, the morphology changes to a faceted dendritic structure.

Concerning the formation mechanism, Bigelow and Flemings suggested that Type III sulfides are formed as a primary phase when the additions decrease the liquidus temperature to a point where interface kinetics are slow enough for faceted growth, however other opinions exist in the literature. Some authors describe it as a primary solidification phase, and precipitation of AlN on Type I Mn(S,Se) was suggested in high manganese and aluminum steels.[8,18] In addition, a decrease in Type I and III sulfides on steels quenched from temperatures right below solidus temperature is an indication that MnS precipitates after steel solidification.[21] This claim has been supported by many authors and precipitation of MnS on the surface of oxides and nitrides was observed in different steels.[4,17,22]

In this context, the current study evaluates the effect of different sulfur additions on the types of nonmetallic inclusions formed and the corresponding influence on the microstructure and fracture properties of Fe-Mn-Al-C alloys. At the same time, at the different sulfur contents it will study the MnS morphology in these steels.

2. METHODOLOGY

Two similar heats were prepared in a 100lb induction furnace with a nominal chemistry of Fe – 30%Mn – 9%Al – 1%Si – (0.9-1.2)%C –0.5%Mo-X%S. Molten metal was kept under argon cover by flowing 50scfm of argon on top of the furnace. The crucible inside the furnace was MgO-based. The furnace was initially charged with high

purity induction iron, graphite, ferrosilicon, and ferromolybdenum. After the initial charge was melted, the remaining induction iron, 1020 aluminum, and electrolytic manganese were added and allowed to fully melt. Calcium wire treatment was done by plunging 15" of a 25% calcium cored wire into the melt. In the second heat only, argon stirring was done after Ca-treatment using an argon lance with the flow of 15scfm with the intent to float inclusions created during refining treatments. Floating slag was then physically removed and the melt was heated up to 1640°C and tapped to a MgO ladle. Each steel was bottom-poured into a no-bake modified Y-block sand molds with the casting geometry shown in Figure 1. A base heat was poured directly after being tapped into the ladle. Consecutive sulfur additions were made by plunging steel bags containing iron pyrite into the melt before the second and before the third pour to modify sulfur content. The second heat was produced because primary results from first heat showed that optimal sulfur content was likely in-between two of the sulfur addition from first heat.

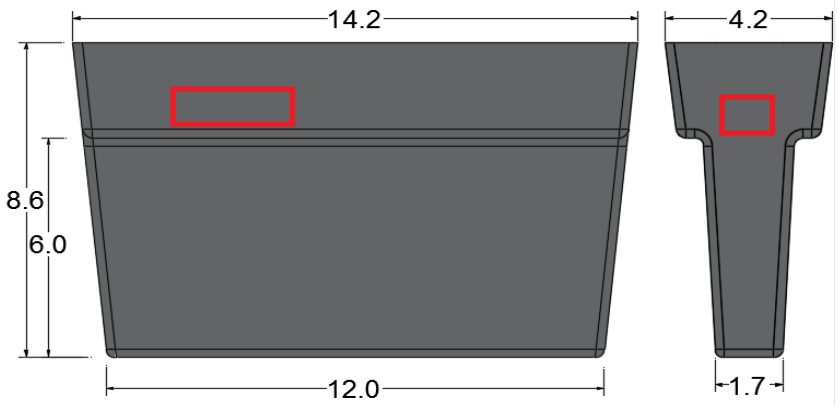

Figure 1. Schematic of the modified Y-block cast showing two orthogonal views. The regions marked in red show the location of inclusion analysis and chemistry samples. Units are in centimeters.

The modified Y-block castings were sectioned using a water cooled abrasive saw to produce chemistry and mechanical test specimens. Samples for chemistry and inclusion analysis were taken from the region marked in red in Figure 1.

Rectangular bars were taken from the lower part of the modified Y-block with its length oriented vertically. Bars were machined to dimensions of 55x10x10 mm as per the Charpy V-Notch specification in the ASTM E23 standard.[23] Dynamic fracture toughness (J_{Id}) was measured by a single-specimen technique using the methodology described by Schindler, ASTM 1820, and ASTM E399.[24-26] The load versus displacement curve obtained were smoothed by a method of moving averages, as described by Kalthoff and Gregor.[27] The J_{Id} for specimens with Type IV, III and II fractures was calculated by the Schindler models, and ASTM E1820 while Type I fracture was calculated with LEFM approach according to ASTM E399 as explained in details by Bartlett.[4,24-26] The bars were notched using a water cooled abrasive saw with a 0.25 mm blade. The fatigue pre-cracks were produced in load-controlled 3-point bending using an R = 0.1. On solution treated bars, an initial load (P_m) of 6000 N was used on the first half of growth. A load of 4000 N was used for the second half of crack propagation. On age hardened bars, loads of 8000 and 5000 N were used for the two stages, respectively. The loads were calculated as defined by ASTM 1820 in Eq. (1) and (2), where P_m is the maximum force applied and σ_Y is the effective yield strength.[25]

$$P_m = \frac{0.5Bb_0^2\sigma_Y}{S} \quad (1)$$

$$\sigma_Y = \frac{(\sigma_{YS} + \sigma_{TS})}{2} \quad (2)$$

The tensile properties used in calculation were taken from a steel with similar composition of Fe – 29.3%Mn – 8.76%Al – 1.22%C – 0.99%Si and hardness of 250 HBN after solution treated.[28] Dynamic fracture toughness tests were conducted utilizing a Tinius Olson Charpy model 84 impact machine fitted with an MPM instrumented striker at room temperature.

In the above equations B is the thickness, b_0 is the unbroken ligament or (W – a_0),W is the width, a_o is the total crack length, obtained as the sum of notch length and pre-crack length, σ_Y is the effective yield strength, S is the span, σ_{YS} is the yield strength, σ_{TS} is the ultimate tensile strength.

Steels were tested in different heat treatment conditions. All the heat treatments were conducted prior to final geometry adjustment, notching, and pre-cracking. Specimens were solution treated inside stainless steel bags at 1050°C for 2 h and then water quenched to avoid carbide precipitation on grain boundaries. Subsequent aging was conducted in a salt pot furnace at a temperature of 530±5°C to reach hardness levels in the range of 320-340 HBN. Specimens were water quenched after aging to halt further phase transformations. Age hardening curves were developed for each base heat by aging from 1h to 100h specimens previously solution treated and then measuring the hardness of each specimen. Hardness measurements were taken according to ASTM E18 utilizing the Rockwell B and C scale and converting to an appropriate Brinell hardness number using conversion tables from ASTM E140.[29,30]

Inclusion analysis was performed using a SEM ASPEX PICA 1020 equipped with BSED, EDS detector, and Automatic Feature Analysis software. The samples were taken from the original casting and from just underneath the fracture surface of the broken test

bars. For each steel at least three surface scans were conducted, for a total area 15 to 30 mm^2. Inclusions were classified in nine different groups: AlN, AlN-MnO, AlN-MnS, MnS, Ca complex inclusions, Mn-Al-S-O, Ti complex inclusions, and porosity.

The chemistry analyses were done by optical emission arc spectroscopy (OES) in a Foundry-Master arc spectrometer from Oxford Instruments. Standards of comparable Mn and Al contents were used for calibration. The oxygen/nitrogen and carbon/sulfur contents were measured by combustion methods using a LECO O-N analyzer and LECO C-S analyzer respectively. Samples for inclusion analysis and optical microscopy were prepared utilizing standard metallographic techniques. For acquiring optical microscopy images, 10% Nital was used as etchant. Analysis of the fracture surfaces of broken specimens was conducted utilizing a HITACHI S4700 and FEI HELIOS Nanolab 600 scanning electron microscope (SEM).

3. RESULTS

3.1. MATERIAL CHARACTERIZATION

The chemistry results for each steel are shown in Table 1. All chemistry values in this study are expressed in weight percent. The lower limit of phosphorus quantification in the OES used is 0.005%, thus a precise quantification of phosphorus was not possible. However, it can be considered a low phosphorus steel with less than 0.005%P.

The presence of ferrite and of a phase consistent with κ-carbide was observed in the ferrite-austenite interface of as-cast steels, as shown in Figure 2. Ferrite amount was quantified by optical microscopy as less than 5% in all steels. After solution treatment,

heat 1 presented a persistent phase on austenite grain boundaries consistent with κ – carbide. In contrast, heat 2 only presented small particles widely dispersed along austenite grain boundaries, as shown in Figure 3. This difference has impacts on the mechanical properties of those steels. As it will be shown later the persistent κ-carbide present on grain boundaries of steels from heat 1 decreases the toughness. Aged microstructures presented no optical difference from the solution treated condition, other than the already expected higher concentration of κ-carbide identified by a faster and more intense etching.

3.2. NONMETALLIC INCLUSION ANALYSIS

The nonmetallic inclusion population was analyzed by automated feature analysis (SEM-AFA). For each steel, more than 3000 inclusions were analyzed. The results are reported as the number of inclusions normalized by the scan area of each sample. The results are listed in Figure 4. One notable result is that the amount of oxides is very low and the presence of oxygen peaks in the EDS spectra during analysis was rarely detected. The low amount of oxides in Fe – Mn – Al – C steels have been reported by other authors and this may be caused by to floatation and removal.[4,6]

On the steels without sulfur addition, 1-A and 2-A, inclusions containing AlN are about 80% of the inclusions. On steel 2-C with 0.020%S, this number is close to 60% and in 1-C with 0.042% it is 40%, the balance is mostly MnS when sulfur is added. The inclusion density of 1-A with no sulfur added is less than half the density present after addition of 0.042%S. This indicates an exaggerated addition of sulfur in this steel since

the objective was to coat the AlN with MnS without a large increase in the inclusion population.

Table 1. Chemistry of Cast Steels with Different Sulfur Additions, wt.%.

Steel	Fe	Mn	Al	C	Si	Mo	S	Cu	Ni	P	N(ppm)	Total O(ppm)
1-A	bal.	29.0	8.70	1.15	1.14	0.34	0.004	0.06	0.03	<0.005	81±40	26±26
1-B	bal.	29.7	8.72	1.13	1.12	0.38	0.019	0.06	0.03	<0.005	42±6	20±10
1-C	bal.	30.2	8.85	1.11	1.10	0.40	0.042	0.06	0.03	<0.005	68±29	29±27
2-A	bal.	29.8	8.44	0.94	1.21	0.55	0.005	0.01	0.02	<0.005	51±7	9±9
2-B	bal.	29.8	8.47	0.96	1.24	0.51	0.007	0.01	0.02	<0.005	60±1	19±4
2-C	bal.	29.8	8.36	0.93	1.21	0.52	0.020	0.01	0.02	<0.005	51±7	8±1

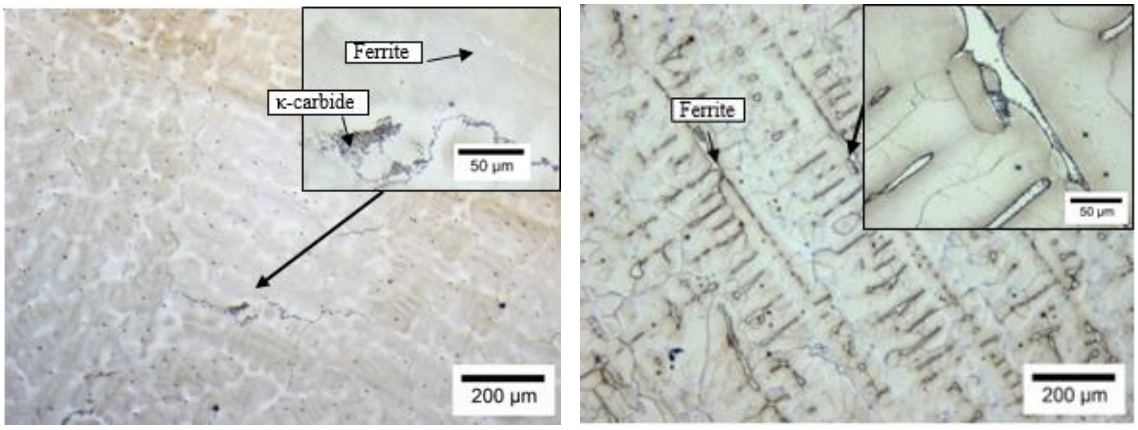

(a) (b)

Figure 2. The microstructures of steels in the as-cast condition. (a) Steel 1-C showed a small fraction of ferrite inside an austenitic matrix and intense κ-carbide precipitation on austenite grain boundaries. (b) Steel 2-C, showed a larger fraction of primary ferrite (less than 5%) at the center of austenite dendrites with κ-carbide precipitated on austenite-ferrite interface. Etched with 10% Nital.

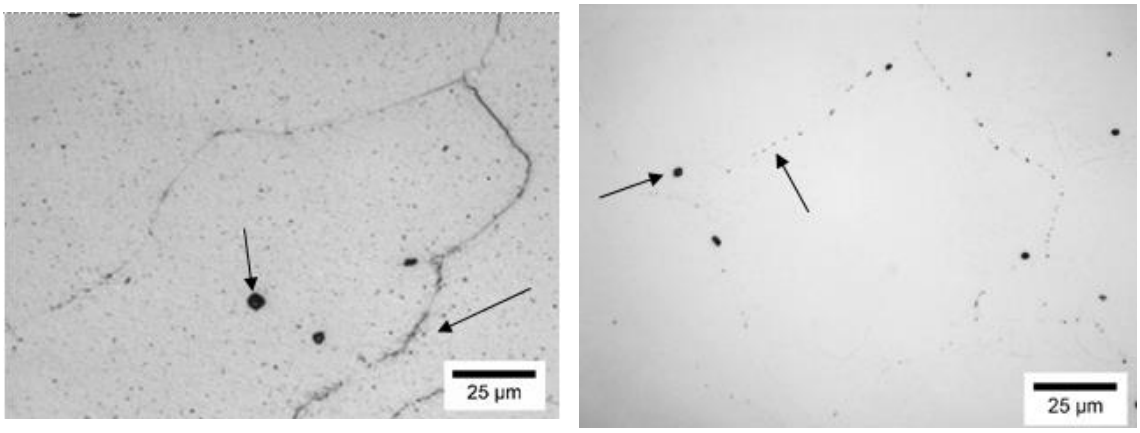

(a) (b)

Figure 3. Representative micrographs from steels (a)1-B and (b)2-C in the solution treated condition. (a) A phase consistent with a κ-carbide or an intermetallic phase was present on some austenite grain boundaries, of steels from heat 1. (b) For heat 2, the less occurrence of this phase was observed with only some isolated particles on grain boundaries. The larger dark-contrasted phases also denoted in these images are MnS that were etched away. Etched with Nital.

As the sulfur content increases, the only inclusion type that increases in quantity is MnS, either as a singular inclusion or as AlN-MnS cored inclusions. The ternary diagrams in Figure 5 shows the main three elements in the chemical composition of the nonmetallic inclusions, both diagrams contain over 95% of the nonmetallic inclusions recorded in the steel. The ternary shows initially 1-A contained mostly AlN, with Mn readings from the matrix underneath it. After sulfur increased from 0.004% in 1-A to 0.042% in 1-C a large number of inclusions with 15-35 wt.% of sulfur, and Al as high as 50% appeared. Figure 6 shows examples of MnS, AlN-MnS, and AlN inclusions with respective chemistries. Both AlN and MnS presented an angular morphology. The Type III faceted MnS were formed in all steels independent of sulfur content. The only Type I MnS seen had significant amount of Ca in its composition.

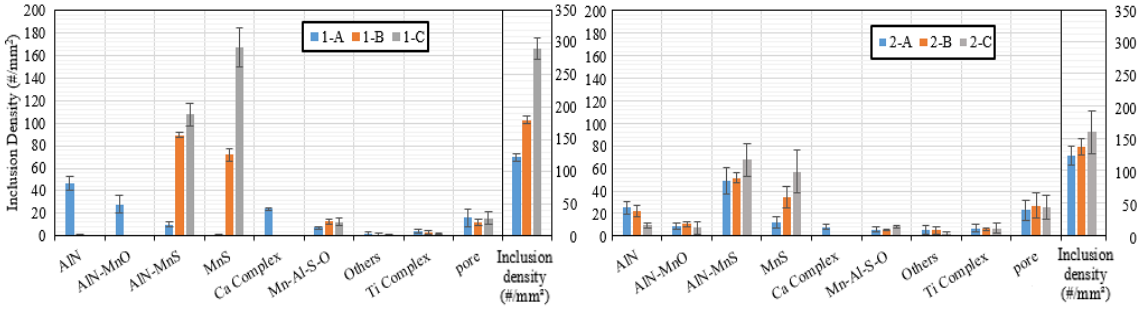

Figure 4. Inclusion population of each steel. Heat 2 shows less increase in coating effect on AlN by MnS. Others are oxides and complex Ti-rich carbides or unclassified inclusions. Results are an average of 3-4 analysis with at least 1000 inclusions each.

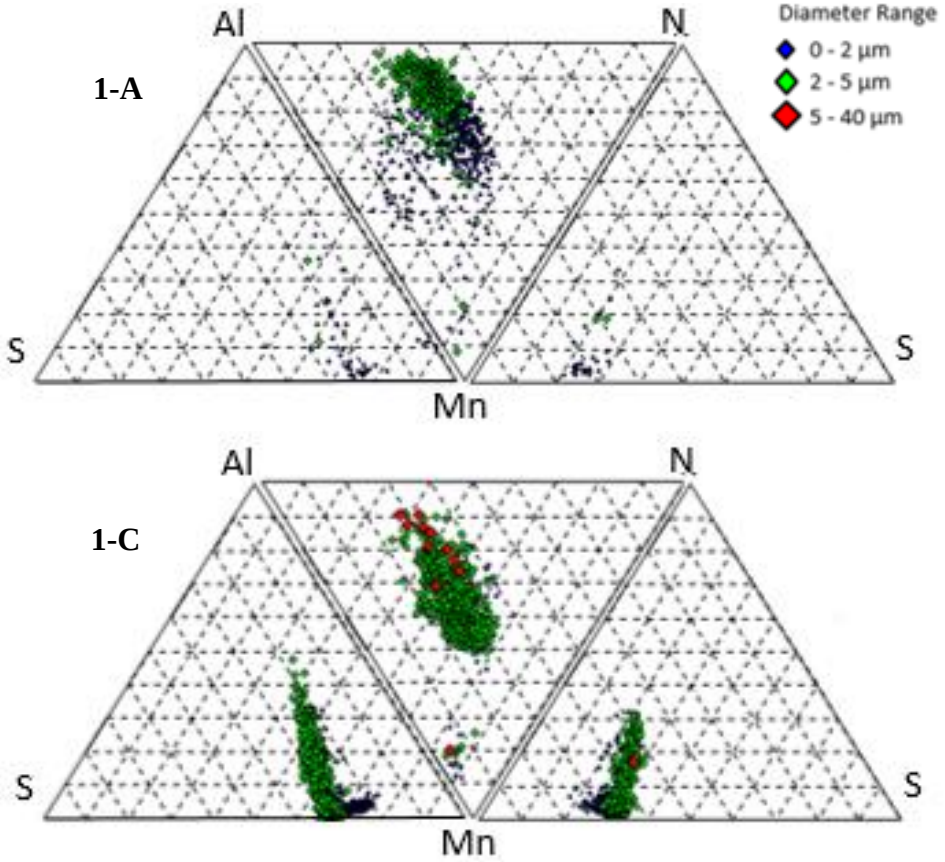

Figure 5. Composition of ternary diagram containing the inclusions which the major three elements are the ones in each diagram. Increasing the sulfur in 1-A from 0.004% to 0.042% in 2-C, only increased general size and the amount of high Mn and S inclusions

The inclusions classified as “others” were mainly particles that recorded sulfur and nitrogen too low to be classified as either AlN or MnS, and those were not more than 5% for any scan. Some Mg-based inclusions were observed and are believed to be from reaction with the MgO crucible or the argon lance used. Titanium bearing inclusions often contained nitrogen and carbon and were shown agglomerated with MnS inclusions. The amount of “others” was higher in the first mold poured in each heat due to a higher presence of calcium modified sulfides, which tend to float and be poured first in lip poured ladles.

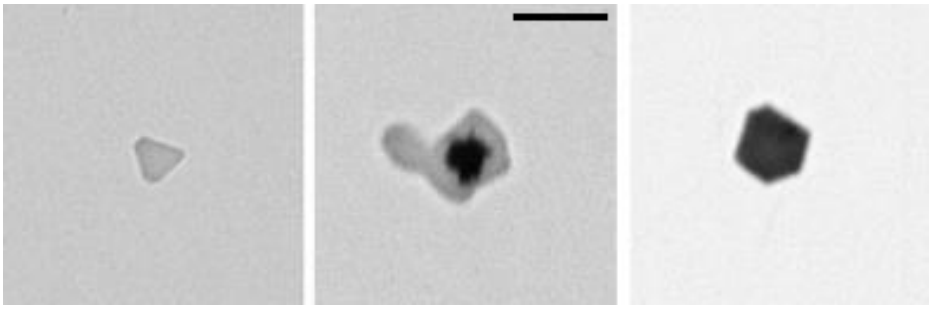

Weight %	MnS (A)	AlN-MnS (B)	AlN (C)
Al	2	25	52
Mn	64	36	7
N	9	21	41
S	25	18	0

Figure 6. SEM BSE example images of the majority of nonmetallic inclusions present in the steels and corresponding nominal chemistries, MnS (A), AlN-MnS (B), and AlN (C).

The total inclusion density was the lowest of 70 mm^{-2} for the lowest sulfur content seen in steels 1-A. Addition of sulfur to 0.02% in 1-B and 2-C raised it to 180 and 159 mm^{-2}, respectively. The difference in inclusion density although not small is within the standard deviation of the values. The highest inclusion density of 291 mm^{-2} was for the highest sulfur content of 0.042% in 1-C.

The total inclusion area fraction follows the same trend with the sulfur additions. The inclusion density of single AlN inclusions decreases with increasing sulfur additions. In heat 1-A (0.004%S) the amount of single AlN is the highest with 47mm^{-2}. In heat 2, even for similar sulfur of 0.005 and 0.007% in 2-A and 2-B respectively, the amount of AlN is much smaller, below 30 mm^{-2}, this is due to more AlN being coated by MnS as shown by the amount of AlN-MnS next to 50 mm^{-2} in 2-A while less than 10 mm^{-2} in 1-A. In steel 2-C with 0.02% S, the amount of single AlN is less than 10mm^{-2}. In steels 1-B also with ~0.02% S and 1-C with 0.042%, the amount of AlN was less than 1 mm^{-2}. It is then clear that the addition of sulfur is leading to the formation of MnS in the surface of free AlN. As expected, most of the AlN is coated with MnS with higher sulfur additions (>0.02%).

Addition of sulfur in general slightly increased the sizes of all inclusions, the average diameter of the inclusions of each steel is shown in Figure 7. Average size increased from 2.3 μm in 1-A and 2-A to 2.6 and 2.8 in 1-C and 2-C respectively. Increase in inclusion size was mainly the result of an increase in size of MnS and AlN-MnS. However, the average increase in all cases was no more than 1.1 μm when comparing any two steels.

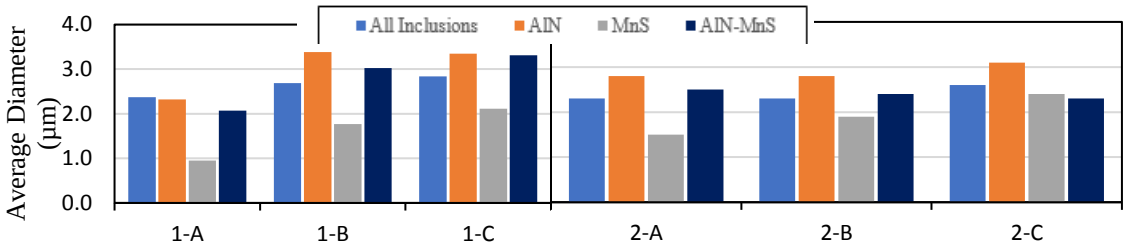

Figure 7. Average inclusion diameter for cast steels. All inclusions tend to increase in size with increasing sulfur addition as well as time hold in the ladle.

3.3. MECHANICAL TESTING

Hardness was measured in the as-cast, solution treated, and aged bars, results are listed in Table 2. The higher carbon content in steels from heat 1 increase the matrix hardness compared to heat 2. Heat 1 had an average hardness of 343 HBN and 256 HBN, in as-cast and in solution treated conditions, respectively. An 86 and 39 HBN increase when compared to heat 2.

Charpy V-notch (CVN) toughness' are listed in Table 2. In the solution treated condition, the highest breaking energy was measured for the steels with less sulfur 1-A and 2-A, with values of 179 J and 152 J. After aging, breaking energy decreased significantly for both heats, for steels 1-A, 1-B, and 1-C, breaking energy was around 10J despite the differences in sulfur. For heat 2, toughness decreased to values between 30-45 J with lower results for higher sulfur additions.

The highest dynamic fracture toughness (DFT) in the solution treatment condition was 670 kJ/m^2 of steel 1-A. At 0.019%S, the DFT of solution treated bars of steel 1-B decreased to 422 kJ/m^2. However, further sulfur increase in steel 1-C the solution treated DFT was 508 kJ/m^2, slightly higher. After aging specimens from heat 1 to a hardness of

329-336 HBN, the time to fracture during the impact was too small and insufficient for data to be instrumented output leading to errors in calculation of instrumented energy. When aged to 333 HBN, steel 2-A had a DFT of 137 kJ/m^2 and after increase in sulfur from 0.005% in 2-A to 0.02% in 2-C the DFT decreased to 43 kJ/m^2 at 340 HBN.

The fracture behavior during DFT testing can be very important on high energy absorbing applications, like in the military or shock absorbing structural applications. In these situations, a Type III or IV fracture is preferred.[4] The Type I fracture is characterized for a crack initiation at maximum load and unstable crack growth, while Type II is when there is a small plasticity at crack tip followed by failure at maximum load.[4, 25]

The fracture behavior during the dynamic fracture toughness testing was Type IV in solution treated condition for all steels, characterized by stable crack growth by ductile tearing.[4, 6] As mentioned before the time to fracture after aging was too short for calculating the DFT in steels from heat 1, therefore, a Type I fracture with a sharp load peak followed by unstable crack was recorded. On steel from heat 2 the fracture behavior was a Type II/I fracture at 0.005%S and Type I only at 0.007% and 0.020%S.

4. DISCUSSION

The manganese sulfides formed were in general faceted Type III inclusions despite different sulfur contents. The Type III morphology of the manganese sulfides is in agreement with studies by Oikawa et al.[18] that suggests this type is formed in overkilled steels. The sulfides morphology is also supported by previous studies proposing low

dissolved oxygen (<10 ppm) leads to Type III formation.[7, 19] Even though the dissolved oxygen was not measured, total oxygen content was below 30 ppm in all steels, and as low as 8ppm in 2-C, it implicates that dissolved oxygen is even lower since oxides, even in small amounts were present in all steels, as in Figure 4.

The nitrogen contents are between 42 and 81 ppm, however, standard deviation is as high as 40 ppm and no definite difference can be determined. The total AlN density, obtained as the sum of the densities of AlN, AlN-MnO and AlN-MnS, is very stable throughout the steels with its minimum as 83 in 1-A and 108 mm^{-2} in 2-C. The same is true for oxygen and respective oxides. Values are shown in Figure 8. In Figure 7, the sizes of AlN were similar to AlN-MnS within each steel, while single MnS were generally smaller. This indicates that smaller AlN are preferentially coated with MnS. Also the size of all inclusions increase with sulfur addition. However, this may not be solely attributed to sulfur additions since steels with higher sulfur were also hold in the ladle for longer time possibly leading to clustering and growth of preexisting AlN and other inclusions.

Inclusions that attach to each other can form a continuous inclusion cluster during solidification. This will cause the average diameter to go up but number of inclusions to go down, since it is counted as a single inclusion. However, the close-spaced inclusions can be quantified and were recorded as a density of clusters per area. Clusters were identified as groups of two or more inclusions spaced by less than twice the diameter of the larger one. Figure 9 shows a clear linear relation between sulfur content and the number of cluster per area for both heats.

Table 2. Summary of hardness, CVN toughness, DFT, inclusion area fraction, and total inclusion density for each steel. Hardness Measurements were Taken in HRB and HRC and Converted to HBN.

	Condition	Hardness (HBN)	CVN Breaking Energy (J)	Dynamic Fracture Toughness, J_{ID} (kJ/m^2)	Fracture Type	Inclusion Area Fraction (ppm)	Total Inclusion density (mm^{-2})
1-A	**As-Cast**	334 ± 24	-	-	-	372 ± 37	122 ± 6
	Sol. Treated	259 ± 8	179 ± 10	670 ± 129	Type IV		
	Aged for 2h	329 ± 14	11 ± 3	*	Type I		
1-B	**As-Cast**	349± 5	-	-	-	951 ± 43	180 ± 6
	Sol. Treated	255 ± 12	151 ± 9	422 ± 94	Type IV		
	Aged for 2h	336 ± 9	9 ± 2	*	Type I		
1-C	**As-Cast**	345± 7	-	-	-	1842 ± 247	291 ± 16
	Sol. Treated	254 ± 9	113 ± 6	508 ± 30	Type IV		
	Aged for 2h	335 ± 7	10 ± 3	*	Type I		
2-A	**As-Cast**	263 ± 7	-	-	-	550 ± 60	123 ± 24
	Sol. Treated	218 ± 4	152 ± 13	411 ± 57	Type IV		
	Aged for 17h	333± 12	44 ± 4	137 ± 41	Type II/I		
2-B	**As-Cast**	252 ± 6	-	-	-	690 ± 37	136 ± 15
	Sol. Treated	215 ± 3	136 ± 3	661 ± 166	Type IV		
	Aged for 17h	334± 8	30± 2	126 ± 24	Type I		
2-C	**As-Cast**	255 ± 4	-	-	-	841 ± 278	159 ± 38
	Sol. Treated	217 ± 3	139 ± 11	628 ± 127	Type IV		
	Aged for 17h	340± 16	30± 3	43 ± 3**	Type I		

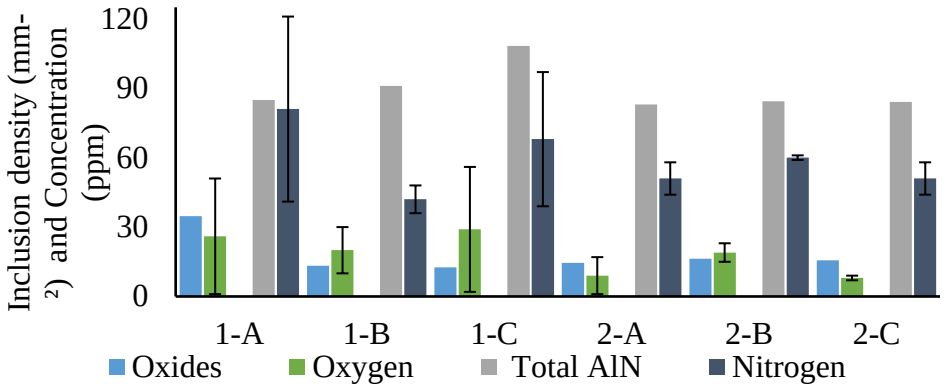

Figure 8. The inclusion density of nitrides (as any form of AlN) and oxides presented a good relation with the measured total oxygen and nitrogen.

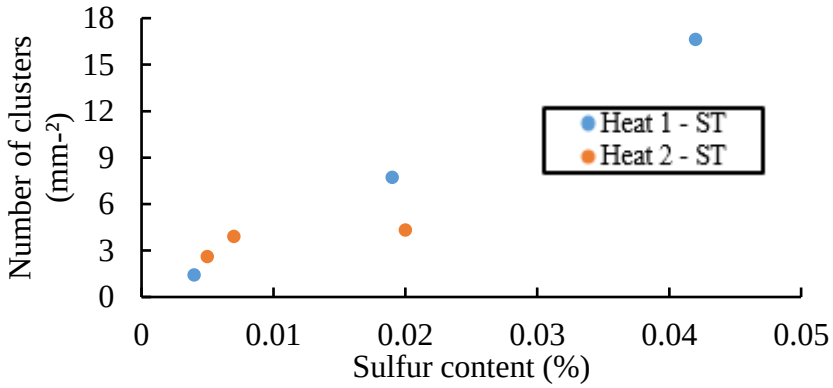

Figure 9. Number of clusters per area had a strong linear relation with sulfur content for both heats.

Figure 10 shows the breaking energy results for each steel in the solution treated and age hardened condition. The sulfur additions affected the CVN breaking energy in different ways depending on the heat treatment condition and amount and type of inclusion formed. Previous studies on Fe – Mn – Al – C showed an inverse relationship to the amount of AlN inclusions and the breaking energy.[6, 8] This trend was not observed by the steels tested in this study.

The addition of sulfur modified the AlN inclusions by coprecipitation of MnS on it. With the addition of 0.019% sulfur, the coprecipitation of MnS on the surface of AlN decreased the amount of single AlN inclusions to virtually zero on steel 1-B.

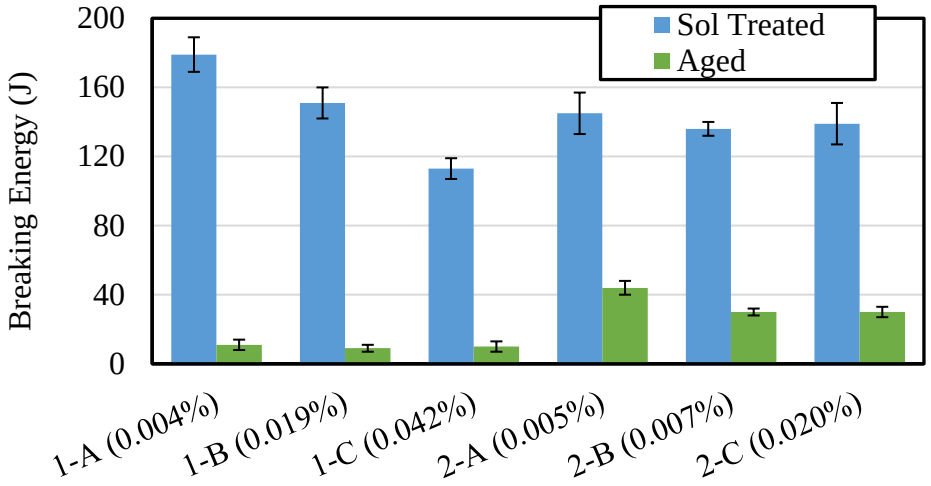

Figure 10. Charpy V-notch breaking energy in the solution treated and in the age hardened conditions. Increasing sulfur content (in parenthesis) decreased the breaking energy, except for age hardened steel from heat 1.

Thermodynamic simulation using software ThermoCalc 2017a with database TCFE9 were done to predict the amount of nonmetallic inclusions to be formed upon solidification. Simulations were done to a steel with composition similar composition to the ones cast, shown in Figure 11. To form the inclusions it was considered 30ppm of oxygen, 60ppm of nitrogen and the sulfur was varied according to 1-A, B and C. It was predicted that AlN inclusions nucleate at high temperature while at 0.004%S the MnS only nucleates from the solid. At that chemistry 0.017%wt. of AlN is expected to form.

For inclusions with an average radius, R, to be coated by a thickness of R/2 of sulfur, the amount of sulfur formed needs to be 1.25 times more. At 0.004%S, the amount of MnS formed is half the amount of AlN, while at 0.02%S it is formed 3 times more. Since not all MnS nucleates on AlN and the thickness of the layer is variable 0.02% appears to be a good addition for the nitrogen levels on these steels.

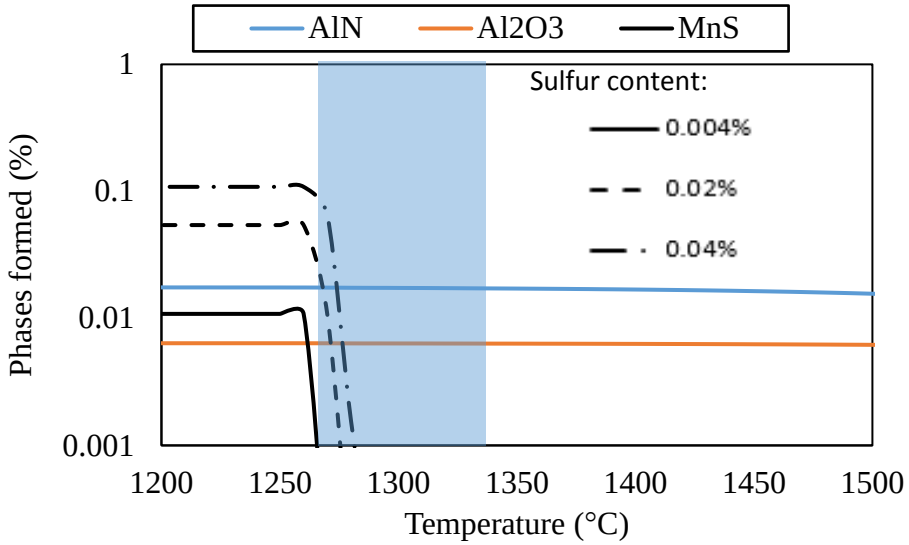

Figure 11. Thermodynamic simulation in equilibrium condition of the amount of nonmetallic inclusions formed upon solidification to a chemistry of Fe-30Mn-9Al-1C-1Si-0.5Mo with 30ppm of oxygen, 60ppm of nitrogen and the sulfur from 0.004% to 0.04%.

However, in the solution treated condition, the highest breaking energy for each trial was obtained from base chemistry steels without sulfur additions (1-A and 2-A) with values of 179 and 145 J, respectively. In the aged condition, in both heats, addition of sulfur decreased the breaking energy at the same time it decreased the single AlN

inclusions, the effect was stronger in heat 1. It appears then that the coating of AlN by MnS did not improve the toughness. It was actually the steels with less sulfur that presented the higher CVN toughness. It is important to notice that coprecipitation of MnS on the surface of AlN increases the average diameter of the inclusions leading to a detrimental effect on impact properties From 2-B to 2-C, however, the amount of single AlN decreased from 30 to 10 mm^{-2}, while MnS increased only from 35 to 55 mm^{-2}. In this case the breaking energy did not decrease as sulfur increased from 0.007% to 0.02%, for both heat treatment conditions tested. This is an indication that the beneficial effect of AlN coating by MnS on the breaking energy is being masked by the effect of increased inclusion density, area fraction and size.

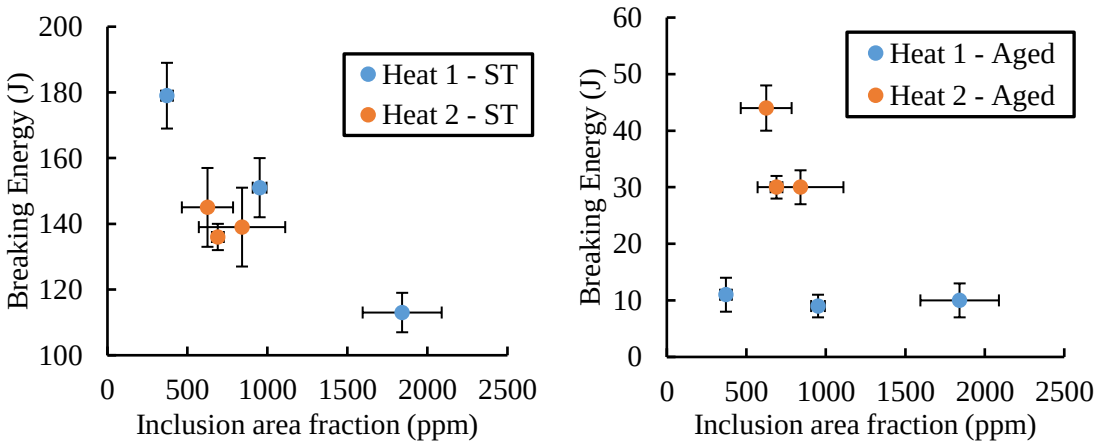

Figure 12. The relationship between Charpy V-Notch breaking energy and area fraction of nonmetallic inclusions in the solution treated and in aged conditions. There is an inverse relationship between inclusion area fraction and breaking energy, except for the aged steels with 1.15%C from Heat 1.

Figure 12 shows the relation between the CVN breaking energy and total inclusion area fraction, in the solution treated and aged conditions. The inclusion area fraction is directly associated with the sulfur addition, in both conditions. In other words, the highest inclusion area fractions are for the highest sulfur addition. As it can be seen, there is an inverse linear relation between breaking energy and inclusion area fraction. The highest breaking energies were in solution treated condition for steels 1-A and 2-A, with 0.004% and 0.005%S, respectively. The breaking energy of 179 J decrease by 66 J when sulfur increased to 0.045% in 1-C. This corresponds to a decrease in breaking energy of 40 J for an increase in inclusion area fraction of 1000 ppm.

Inclusion area fraction increases by 1470 ppm from 1-A to 1-C while it only increases by 216 ppm from 2-A to 2-C. Because of it, the effect of the nonmetallic inclusion area fraction in the breaking energy is much more evident in steels from heat 1. The fracture surfaces in Figure 13(a and b) for steels 1-A and 1-C in the solution treated condition shows how the increased inclusion population modifies the fracture decreasing the absorbed energy. On 1-A voids nucleate on the matrix or on the few inclusions present, while in 1-C it nucleates on large and close-spaces inclusions clusters leading to faster void coalescence and final rupture.

The breaking energy values of 179 J and 145 J for the low sulfur steels are comparable to results published for same nominal composition and heat treatment, of 124 J at 0.006%P and 199 J at 0.001%P.[1] For comparable sulfur contents, the breaking energies were lower in heat 2, when solution treated even with a hardness ~40HBN below heat 1. Two factors are the likely responsible for it, Figure 4, shows a higher porosity on steels from heat 2, of up to 60% more number density. And by comparing the

chemical composition of steels in Table 1, it is shown that steels from heat 2 have lower C of 0.95 % while heat 1 has 1.13% on average. The higher carbon have been shown for a composition of Fe – 30Mn – 9Al – (0.9-1.2)C to increase breaking energy by 20 kJ/m^2 from 0.9 to 1.2%C when solution treated.[6]

On the age hardened bars, a decrease in the CVN breaking energy with increasing inclusion area fraction and sulfur content is observed only for heat 2. This suggests that fracture in the aged condition is not controlled by the overall inclusion density. For test bars from heat 2, aged to a hardness of 333-340 HBN, the breaking energy decreases by approximately 14 J, from 2-A to 2-C, with an increase of 216 ppm in inclusion area fraction.

The carbon content of heat 1 is nominally 1.15%C, and this decreases the breaking energy in aged specimens to such a low level that it is not related to inclusion population anymore. As described in the literature, above 1%C the precipitation of κ-carbides occur in the grain boundaries.[31] Also for Fe – 30%Mn – 9%Al – (0.4-1.2)%C, solution treated at 1150°C and aged at 550°C for 16h, literature shows that above 0.75%C the steel K_{CU} continuously decrease by over 100 J/cm^2 when at a value of 1.2%C.[32] The low fracture energy on steels from heat 1, indifferent to the inclusion population, is also represented by the fracture type shown in Figure 13(c), a completely intergranular fracture, without any void nucleation. Steels with a lower carbon content in heat 2 presented a partially ductile fracture even after age hardening, as in Figure 13(d) This indicates that with increased age hardening, fracture is affected less by the inclusion population and depends mainly on κ-carbide precipitation on both grain boundaries and in the austenite matrix.

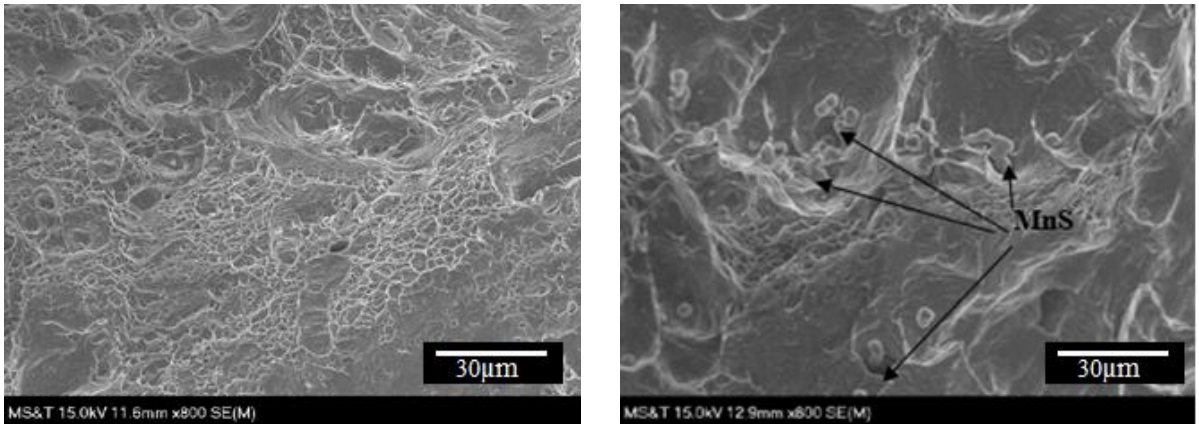

(a) (b)

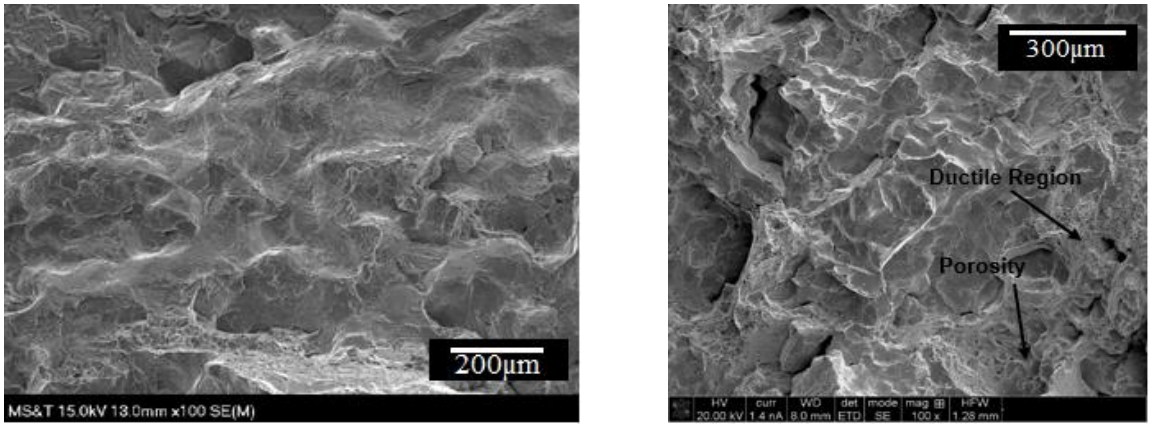

(c) (d)

Figure 13. Secondary electron images of fracture surfaces of Charpy bars after impact test. In the solution treated condition, (a) steel 1-A with 0.004%S had a ductile fracture, few inclusions were seen inside the voids. With increased sulfur to 0.044% (b) steel 1-C maintained the ductile fracture but voids nucleated on larger inclusions that were more numerous. After aging at 530°C to a hardness of 320-340 HBN, (c) steels from heat 1 had a low energy intergranular fracture and (d) steels from heat 2 had a mixed ductile-intergranular fracture.

The inclusion spacing was measured as the average space between each inclusion center and it is nearest neighbor center and is referred as the nearest neighbor distance (NND). The CVN impact test results had a linear relation with the NND for solution

treated steels, for NND from 27 to 40 µm the breaking energy increases from 113 to 179 J, in Figure 14. Similar trend was observed in another study for the DFT of Fe – 30%Al – (3-9)%Al – 0.95C also solution treated at 1050°C for 2h.[6] However, in the present study it only occurred for the CVN impact test.

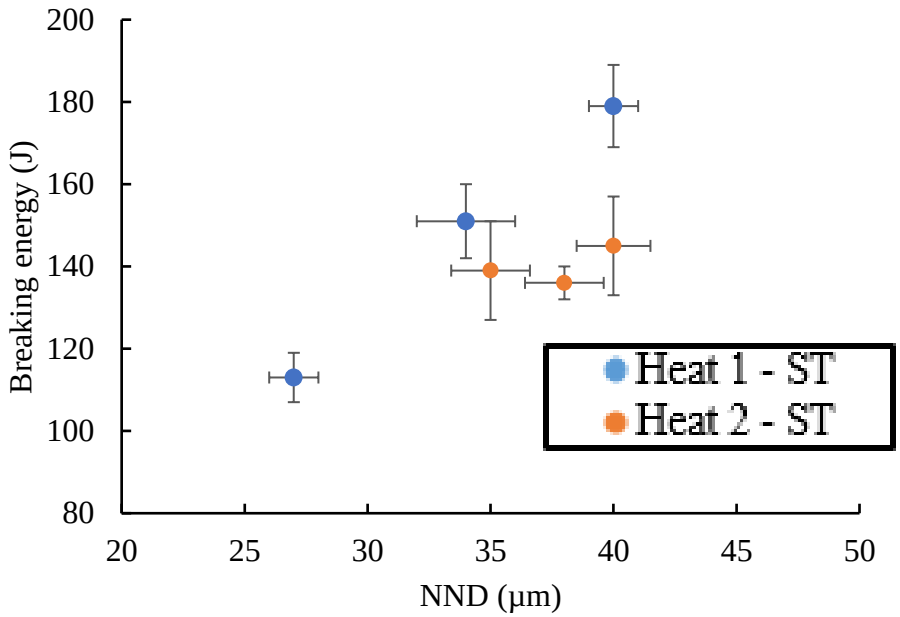

Figure 14. The CVN breaking energy shows a linear relationship with the NND in the solution treated condition.

The DFT results did not correlate to the inclusion population as well as the Charpy V-notch impact toughness. The result for steel 2-A in solution treated condition was significantly lower than 2-B and 2-C, which could indicate a beneficial effect of the MnS, however steel 1-A was significantly tougher than 1-B and 1-C. Although, as shown in Figure 15, when comparing same nominal composition steels and different

sulfur content there is an overall decrease in DFT with increasing inclusion density. After aging, heat 2 presented a direct but not strong relation between these properties. The relation is sustained by the fracture type as determined by the load-displacement curves, which change from Type II to Type T after sulfur addition. The intense decrease in breaking energy observed for increasing carbon over 1% was also confirmed in the DFT tests. Heat 1 with 1.2%C had fracture with such a low energy that data recorded was insufficient for the DFT calculation.

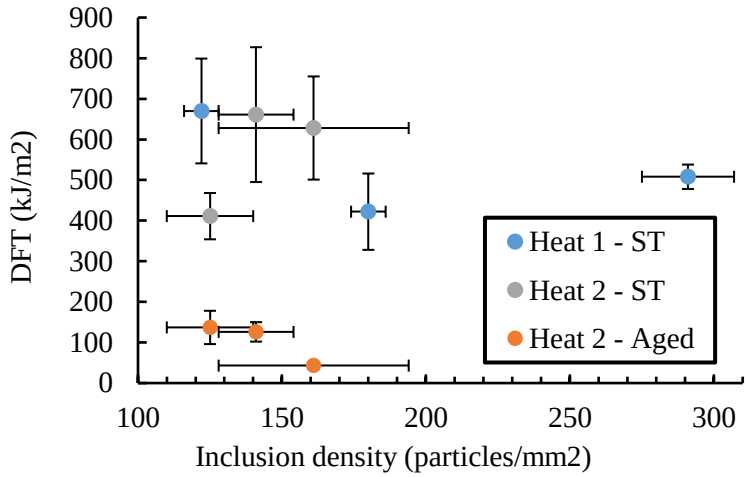

Figure 15. An overall decrease in DFT with increasing inclusion density is observed.

In a previous investigation, for compositions in the range Fe – 30%Mn – (3-9)%Al – (0.9-1.6)%C – 0.9%Si, the fracture behavior was Type IV in all the solution treated bars regardless of the aluminum or carbon contents. With aging, the fracture behavior gradually changes to Type III and II, and finally Type I.[6] These changes occurred for increasing hardening times or carbon contents.

Previous studies observed a correlation between DFT in solution treated condition and inclusion density.[4, 6] Both studies also showed that other factors like deoxidation practice and carbon and aluminum content have even stronger influence on it. The effect of deoxidation on the DFT fracture reported is an evidence that the type of inclusion formed is an important factor on its influence on the DFT. The inclusion analysis in Figure 4, and DFT results in Figure 15 shows no evidence of any improvement in DFT properties by coating of AlN inclusion by MnS. The DFT testing was also shown to have large variability of results on the alloy and conditions tested even following the specifications determined by ASTM E1820.

5. CONCLUSION

AlN is a brittle and angular inclusion that has been previously reported to greatly reduce impact toughness of high manganese and aluminum steels. In this study sulfur additions were used to modify AlN inclusions in a Fe-30Mn-9Al-1Si-(0.9-1.2%)C-0.5%Mo steel. Sulfur additions of 0.02%S in comparison 0.007%S decreased unmodified AlN from 30 to 10mm^{-2} and in the solution treated condition, slightly improved the breaking energy, despite an increased area fraction and average size of inclusions. However, results showed that sulfur additions generally decreased toughness and produced a large amount of coarse and clustered Type III MnS. It was shown that the CVN breaking energy of solution treated specimens decreased by approximately 40 J for every 1000 ppm increase on inclusion area fraction, close to 20% decrease. In the

conditions tested, minimizing sulfur and consequently MnS inclusions optimized the CVN breaking energy.

Increasing amount of carbon in solid solution from 0.9% to about 1.1%C increased the solution treated toughness from 159 to 179 J for steels with the lowest sulfur contents. After age hardening at 530°C to a hardness in the 310-340 HBN range, it was shown that breaking energy was mainly a function of carbon content. Increasing carbon, greatly increased the age hardening kinetics and resulted in κ-carbide precipitation on grain boundaries. This produced brittle intergranular fracture and impact toughness values as low as 10J on steels with about 1.1%C.

Dynamic fracture toughness generally decreased with an increase in the amount of inclusions. No clear relation can be withdrawn from the results due to fairly large standard deviation on the results despite being done according to ASTM E1820.

ACKNOWLEDGMENTS

This work was supported in part by a grant from the Association for Iron and Steel Technology, AIST, Foundation as part of the Kent D. Peaslee Junior Faculty Award. The authors are very grateful to AIST for this award. The authors also gratefully acknowledge Dr. Simon Lekakh for helpful discussion and all graduate students from MS&E Department at Missouri University of Science and Technology for assistance in conducting experiments.

REFERENCES

1. Bartlett, L., and Van Aken, D., "High Manganese and Aluminum Steels for the Military and Transportation Industry." *The Journal of The Minerals, Metals & Materials Society,* vol. 66(9), pp. 1770-1784 (2014).

2. Bartlett, L., Howell, R.A., Schulte, A., Van Aken, D.C., and Peaslee, K.,"A Review of the Physical and Mechanical Properties of a Cast High Strength and Lightweight Fe-Mn-Al-C," *Materials Science and Technology Conference*, pp. 1941–1953 (2010)

3. Van Aken, D., Howell, R., Bartlett, L., Schulte, A., Lekakh, S., Medvedeva, J., Richards, V., and Peaslee, K., "Casting P900 Armor with Lightweight Steel," *63rd Steel Founders' Society of America Technical and Operating Conference, (D*ecember 2009).

4. Bartlett, L., Dash, A., Van Aken, D., Richards, V., and Peaslee, K. "Dynamic Fracture Toughness of High Strength Cast Steels," *International Journal of Metalcasting,* vol. *7*(4), pp, 17-33 (2010).

5. Bartlett, L.N., Van Aken, D.C., Lekakh, S., and Peaslee, K.D., "Mechanical Properties of Cerium-Treated Fe-Mn-Al-C Steel Castings," *AFS Transactions,* vol. 119, paper 11-035 (2011)

6. Bartlett, L.N., and Van Aken, D.C., "On the Effect of Aluminum and Carbon on the Dynamic Fracture Toughness of Fe-Mn-Al-C Steels," *AFS Transactions,* vol. 121(13-1343), (2013).

7. Liu, H., Liu, J., Michelic, S. K., Shen, S., Su, X., Wu, B., and Ding, H., "Characterization and Analysis of Non-Metallic Inclusions in Low-Carbon Fe-Mn-Si-Al TWIP Steels," *Steel Research International,* vol. 87(12), pp. 1723-1732 (2016).

8. Park, J. H., Kim, D., & Min, D. J., "Characterization of Nonmetallic Inclusions in High-Manganese and Aluminum-Alloyed Austenitic Steels," *Metallurgical and Materials Transactions A,* vol. 43(7), pp. 2316-2324 (2012).

9. Schulte, A. M., Lekakh, S. N., Van Aken, D. C., and Richards, V. L., "Phosphorus mitigation in cast lighweight Fe-Mn-Al-C steel," *Transactions of American Foundry Society,* vol.118, pp. 451 (2010).

10. Werdecker, W., and Aldinger, F., "Aluminum Nitride-An Alternative Ceramic Substrate for High Power Applications in Microcircuits*," IEEE Transactions on Components, Hybrids, and Manufacturing Technology,* vol. 7(4), pp. 399-404 (1984).

11. Onink, M., Brakman, C., Tichelaar, F., Mittemeijer, E., Van der Zwaag, S., Root, J., and Konyer, N., "The lattice parameters of austenite and ferrite in Fe-C alloys as functions of carbon concentration and temperature," *Scripta Metallurgica et Materialia,*, vol.29(8), pp. 1011-1016 (1993).

12. Ånmark, N., Karasev, A., and Jönsson, P., "The Effect of Different Non-Metallic Inclusions on the Machinability of Steels," *Materials*, vol. 8(2), paper 751-78. (2015).

13. Sims, C.E., Saller, H.A., and Boulger, F.W., "Sulfide Inclusions in Steel," *Transactions of American Founders' Society,* vol. 57, pp. 233 (1949).

14. Thornton, P. A., "The influence of nonmetallic inclusions on the mechanical properties of steel: A review," *Journal of Materials Science,* vol. 6(4), pp. 347-356 (1971).

15. Volchok, I.P., Kovchik, S.E., Panasyuk, V.V., and Shulte, U.A., "Effect Of Non-Metallic Inclusions On The Propagation Of Cracks In Low Alloy Steel 45 L," *Fiz Khim Mekhan MAT,* vol. 3(4), pp. 440-443 (1967)

16. Maciejewski, J., "The Effects of Sulfide Inclusions on Mechanical Properties and Failures of Steel Components," *Journal of Failure Analysis and Prevention,* vol. 15(2), pp. 169-178 (2015).

17. Herring, Daniel. "Steel cleanliness: Inclusions in steel," The Heat Treat Doctor, (n.d.), http://www. heat-treat-doctor.com/documents/Inclusions%20in %20Steel.pdf (27 October 2017).

18. Oikawa, K., Ohtani, H., Ishida, K., and Nishizawa, T., "The Control of the Morphology of MnS Inclusions in Steel during Solidification*," ISIJ International,* vol. 35(4), (1995).

19. Marich, S., and Player, R., "Sulfide inclusions in iron," *Metallurgical Transactions,* vol. 1(7), pp. 1853-1857 (1970).

20. Bigelow, L. K., and Flemings, M. C. "Sulfide inclusions in steel," *Metallurgical Transactions B,* vol. 6(2), pp. 275-283 (1975).

21. Ito, Y., Masumitsu, N., and Matsubara, K. "Formation of Manganese Sulfide in Steel," *Transactions of the Iron and Steel Institute of Japan,* vol. 21(7), pp. 477-484 (1981).

22. Valdez, M. E., Wang, Y., and Sridhar, S. "MnS Precipitation Behavior in Re-Sulfurized Steels with Intermediate Levels of Sulfur," *Steel Research International,* vol. 76(4), pp. 306-312 (2005).

23. ASTM International. "ASTM E23-16b Standard Test Methods for Notched Bar Impact Testing of Metallic Materials," (2016).

24. Schindler, H.J., “Estimation of the Dynamic J-R Curve from a Single Impact Bending Test,” Mechanics *of Damage and Failure: proceedings of the 11th ECF*, pp. 2007–2012 (1996).

25. ASTM International. “ASTM E1820-16 Standard Test Method for Measurement of Fracture Toughness,” (2016).

26. ASTM International. “ASTM E399-12e3 Standard Test Method for Linear-Elastic Plane-Strain Fracture Toughness KIc of Metallic Materials,” (2012).

27. Kalthoff, J.F., Gregor, M., “Instrumented Impact Testing of Subsize Charpy V-Notch Specimens,” *STP37985S Small Speciment Test Techniques*, pp. 98-109 (1998).

28. Bartlett, L., "On the effect of silicon and phosphorus during the precipitation of k-carbide in Fe-Mn-Al-C alloys," PhD diss., Missouri University of Science and Technology (2013).

29. ASTM International. ASTM E18-16 Standard Test Methods for Rockwell Hardness of Metallic Materials,” (2016).

30. ASTM International. “ASTM E140-12be1 Standard Hardness Conversion Tables for Metals Relationship Among Brinell Hardness, Vickers Hardness, Rockwell Hardness, Superficial Hardness, Knoop Hardness, Scleroscope Hardness, and Leeb Hardness,” (2012).

31. Howell, R, "Microstructural influence on dynamic properties of age hardenable FeMnAl alloys," PhD dissertation, *Missouri University of Science and Technology*, (2009).

32. Kalashnikov, I., Acselrad, O., Shalkevich, A., and Pereira, L., “Chemical Composition Optimization for Austenitic Steels of the Fe-Mn-Al-C System,” *Journal of Materials Engineering and Performance,* vol. 9(6*)*, pp. 597-602. (2000).

II. PROGRESS IN GRAIN REFINEMENT OF FeMnAl CASTINGS. PART 1. FULLY AUSTENITIC FeMnAlC STEEL TREATED BY COMPLEX TiN BEARING MASTER ALLOY

Rairu Vaz Penna, Laura N. Bartlett

Missouri University of Science and Technology
Materials Science & Engineering Dept.
1400 N Bishop, Rolla, MO, U.S.A., 65409

Keywords: high manganese steels, inoculation, nonmetallic inclusions, grain refinement, titanium

ABSTRACT

The effect of different grain refining additions on the solidification structure of lightweight Fe-30Mn-5.5Al-1.5C-1.2Si steel castings was analyzed by thermodynamic calculations and experimental heats. Thermodynamic simulations and lattice disregistry calculations were utilized to predict the inclusions most likely to serve as heterogeneous nucleation sites for primary austenite solidification in the Fe-Mn-Al-C system. TiN as a grain refinement addition was considered because of the success of this inoculant in other austenitic steel systems. Addition of TiN was performed through the use of a pre-made master alloy (MA) containing a large fraction of fine TiN particles.

Experimental castings were produced from cylindrical phenolic resin bonded sand molds with a bottom chill to introduce directional solidification. Additions of 0.5 and 1.5% TiN containing MA (up to 0.29 wt.% Ti in casting) did not yield detectable grain refinement of the macro structure when compared to the base heat. Scanning electron microscopy identified the inclusions present in the resulting castings consisted mainly of

Ti(C,N) with up to a 0.4% area fraction. Comparison with other studies that used TiN inoculation suggests that manganese and sulfur may be influencing the adsorption energy of Fe or producing a nanoscale reaction layer that may be less favorable for nucleation.

1. INTRODUCTION

1.1. GRAIN REFINING INOCULATION OF AUSTENITIC STEELS

The need to reduce weight in the transportation industry as well as for military ordnances has created a demand for lightweight materials with high strength, good ductility, and high energy absorbing capabilities. Steels that belong to the Fe-Mn-Al-C system, especially within the compositional range of (15-30)Mn – (3-12)Al – (0.5-1.2)C – 1Si, are promising candidates for lightweighting of vehicles and structures. The density of austenitic Fe-Mn-Al-C steels is decreased by 1.25%/wt% added Al and by 5%/wt%C compared to pure FCC iron. All compositions in the following text are in weight percent unless otherwise noted. Most studies have centered around the Fe – 30Mn – 9Al – 0.9C nominal composition, which has a total weight reduction of 14.8% when compared to high strength low-alloy steels.[1,2] The mechanical properties of these alloys can range from 700-1300 MPa in ultimate tensile strength, UTS, and 10-90% elongation depending on heat treatment.[2]

Difficulties can arise during casting and hot rolling of high Mn and Al steels because of a coarse as-cast grain structure and high amounts of segregation. Generally, refinement of the as-cast solidification structure by melt inoculation reduces microsegregation and macrosegregation, promotes a more uniform response to heat

treatment, reduces anisotropy, and improves both strength and ductility.[3,4] Grain refinement of the as-cast microstructure can be accomplished by an inoculation treatment where particles or inclusions are utilized to promote heterogeneous nucleation of austenite during solidification. Grain refining additions are commonly performed by one of two methods: (1) by forming the appropriate dispersoids in-situ, which can be done by controlling the deoxidation, desulfurization, and alloying practices to promote the formation of specific inclusions, or (2) by adding particles in a master alloy containing the desired dispersoids.[5,6]

Very few studies have focused on grain refinement during solidification of austenitic Fe-Mn-Al-C steels. One study of an Fe-18Mn-1C-2.5Cr austenitic steel showed a grain size reduction from 1mm to 0.23mm with a 0.05%Ce addition accompanied by 0.02%B. Inclusions observed in that study consisted mainly of CeO_2 and Ce_2OS_2 precipitates, however, it was suggested that mainly $CeAlO_3$ contributed to the grain refinement of austenite.[7] In another study, the authors achieved an order of magnitude reduction in grain size and suppression of the columnar structure by the addition of 0.1%Ce in a Fe-30Mn-7.5Al-1.1C-(0.7-1.1)Si-0.5Mo steel. The addition of cerium led to the formation of complex cerium sulfides, oxides, and phosphides.[8] However, not all of the Ce based inclusions contributed to grain refinement and it was also suggested in this study that $CeAlO_3$ inclusions may have been responsible for grain refinement during solidification.[8] Unfortunately, the large amount of cerium oxide and sulfide inclusions reduced the notch toughness in the solution treated steel despite the reduction in grain size.[8] Therefore, both the cerium addition and the amount of residual elements such as

sulfur must be tightly controlled in order to avoid generating a large number of inclusions that can degrade fracture toughness.

A survey of grain refining additions in other austenitic steels could be helpful to better understand their potential as potential inoculants for Fe-Mn-Al-C steels. Additions of Nb, B, Ti, V, Zr, Hf, Ce, and La produce carbides, nitrides, or oxides and have been considered as candidates in Ni-Cr austenitic steels and medium carbon steels with a primary austenitic solidification mode.[5,9-13] The authors showed that TiN inclusions were effective at producing grain refinement in a cast equivalent of AISI 319L austenitic steel.[3] However, recent studies show that the effectiveness of TiN as an inoculant depends on the solidification mode of the alloy.[5] During solidification, austenite or δ-ferrite may form as the primary phase depending on the effect of composition on the shift of the peritectic reaction. TiN was found to be an effective nucleating agent for steels that solidify as primary austenite or primary ferrite. However, steels with a dual solidification path showed less grain refinement than castings that solidified purely as ferrite or austenite.[5]

1.2. HETEROGENEOUS NUCLEATION THEORY

Classical nucleation theory predicts that a low lattice disregistry and a low interfacial energy between the nucleating solid and the heterogeneous nucleus enhances nucleation by decreasing the critical nucleation barrier or activation energy. Assuming a spherical cap shape for the nucleating solid, the critical nucleation barrier for heterogeneous nucleation, ΔG^*_{Het}, can be described by Eq. 1, where θ is the wetting angle of the nucleating solid phase on the heterogeneous nucleation site

$$\Delta G^*_{Het} = \frac{(2+\cos\theta)(1-\cos\theta)^2}{4} * \Delta G^*_{Hom} = f(\theta) * \Delta G^*_{Hom} \quad (1)$$

ΔG^*_{Hom} is the critical nucleation barrier for homogenous nucleation,[14] where

$$\Delta G^*_{Hom} = \frac{16\,\pi\,\gamma_{LS}^3}{3\,\Delta G_V^2} \quad (2)$$

and

$$\gamma_{nL} = \gamma_{nS} + \gamma_{LS}\cos\theta \quad (3)$$

Thus, for high solid-liquid interfacial energies, a large amount of undercooling is required for nucleation. As shown in Figure 1, the wetting angle is defined by the interfacial energy balance between the nucleating solid, substrate, and liquid phase and is influenced by several factors including the similarity of chemical bonding, topographic features, surface area of the substrate and the lattice disregistry.[15,16] Eq. 1 demonstrates that the energy barrier for nucleation decreases as the wetting angle decreases.

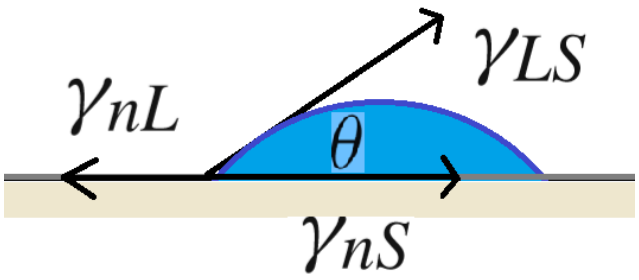

Figure 1. The wetting angle for heterogeneous nucleation is defined by the interfacial or surface energy balance between the nucleating solid (S), substrate (n), and liquid phase (L).

In case of complete wetting, **θ** = 0, no nucleation barrier exists. Young's equation, Eq 3, shows that a low contact angle between the solid and nucleant particle is promoted

by a high surface energy between the liquid and the nucleant, γ_{nL}, or a low surface energy between the nucleant and the solid, $\gamma_{nS.}$ In practice, measurement of the interfacial energy is very difficult, and often a low lattice disregistry is use to identify potential inoculants. Lattice disregistry can be calculated by the Bramfitt`s planar lattice disregistry model, shown in Eq. 4, and it is commonly used as an estimation of good wettability.[17-21]

$$\delta_{(hkl)_n}^{(hkl)_s} = \sum_{i=1}^{3} \frac{1}{3} \left[\frac{\left| \left(d_{[uvw]_s^i} cos\gamma \right) - d_{[uvw]_n^i} \right|}{d_{[uvw]_n^i}} \right] x\ 100\% \qquad (4)$$

where $(hkl)_s$ is a low-index plain of the substrate, $[uvw]_s$ is a low-index direction in $(hkl)_s$, $(hkl)_n$ is a low-index plane in the nucleated solid, $[uvw]_n$ is a low-index direction in $(hkl)_n$, $d_{[uvw]n}$ is the interatomic spacing along $[uvw]_n$, $d_{[uvw]s}$ is the interatomic spacing along $[uvw]_s$, γ is the angle between $[uvw]_s$ and $[uvw]_n$.

This method was used in several publications to predict inoculation efficiency of precipitates in austenitic and ferritic steels and was adopted in this article for Fe-Mn-Al steel.[9,18-,21] The focus of this study is to identify potential precipitates in age-hardenable austenitic FeMnAlC steels that can refine the as-cast structure during solidification. The effectiveness and stability of promising candidate inclusions were modeled utilizing thermodynamic simulations as a function of temperature, steel composition, and solidification path. Experimental investigations presented in this paper report on the effectiveness of TiN as a possible grain refining agent in a fully austenitic Fe-30Mn-5.5Al-1.5C-1.2Si steel. In-situ inoculation by co-precipitation of $MgAl_2O_4$ and Ti(C,N) was also considered and the results will be discussed in part two of this study.

2. METHODOLOGY

2.1. EXPERIMENTAL ALLOY DESIGN

The ability of a precipitate to act successfully as a heterogeneous nucleation site appears to depend on the solidification path of the alloy. Some FeMnAlC steels have a dual phase solidification mode in which ferrite will nucleate from the liquid first, followed by austenite at the end of solidification.[3] The authors showed that dual solidification mode steels are difficult to grain refine compared to single phase solidifying steels.[5] ThermoCalc 2017a[22] was used to develop a steel chemistry with single-phase austenite solidification as well as to evaluate the stability of different candidate inclusions in the melt. The alloy composition ranges investigated were Fe-30%Mn-(5-12%)Al-(0.6-2)%C. These compositions are age hardenable and produce at least a 10% density reduction compared to martensitic 4130 steels.[23]

The solidification sequence of different age hardenable austenitic FeMnAlC steels was investigated by evaluating the effect of aluminum and carbon under equilibrium conditions in a Fe-30Mn-1Si steel. Silicon is added to prevent β-Mn formation and promote good fluidity.[24] Aluminum is typically considered to be a ferrite stabilizer and carbon is an austenite stabilizer in steel. The calculated influence of aluminum on the solidification sequence is shown in Figure 2 for a composition of Fe-30%Mn-(5-9)%Al-1%C-1%Si. The amount of each phase at a specific temperature is represented by the fraction of a vertical line drawn that is within each phase region. The Fe-30%Mn-5%Al-1%C-1%Si steel in Figure 2(a) is shown to have 40 wt.% primary δ-ferrite forming first during solidification followed by austenite that forms through a peritectic reaction during

the remaining solidification. The final as-solidified microstructure is predicted to be 100% austenite. Figure 2(b) shows that increasing the aluminum content to 9%Al results in an alloy that solidifies as 40% primary ferrite followed by austenite. However, at the solidus temperature of 1260°C, the 9%Al steel is predicted to contain 20% ferrite and 80% austenite. Thus, varying only aluminum in the composition can modify the amount of ferrite and austenite but solidification remains dual-phase in the 30%Mn-(5-9)%Al-1%C-1%Si steel.

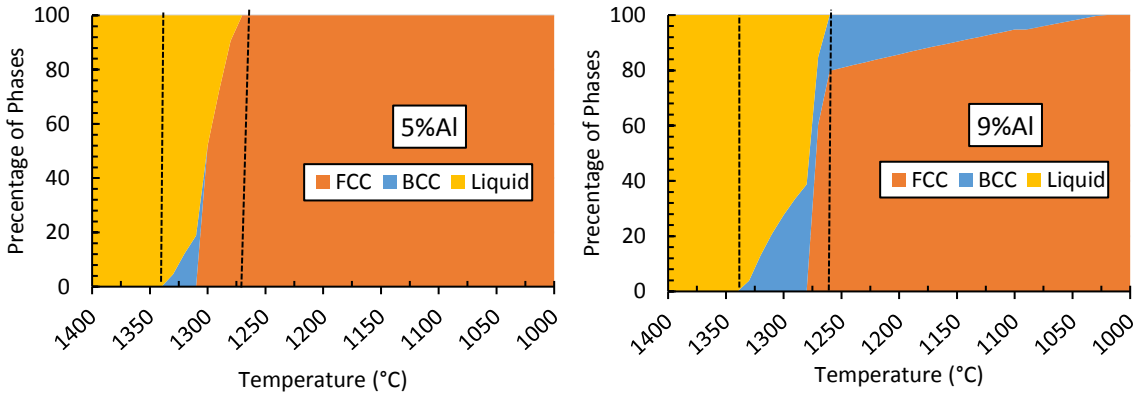

Figure 2. The equilibrium solidification modeling of a (a) Fe-30%Mn-5%Al-1%C-1%Si and (b) Fe-30%Mn-9%Al-1%C-1%Si steel.

Carbon is an austenite stabilizer and the effect of carbon on the solidification sequence of a Fe-30%Mn-5%Al-(1-1.5)%C steel was also determined using thermodynamic modeling. Figure 3 shows that an increase in carbon content stabilizes austenite in the Fe-30%Mn-5.6%Al-(1-1.5)%C-1%Si steel. A carbon content of 1.5%C is

needed to suppress formation of primary ferrite during solidification of the Fe-30%Mn-5.6%Al-1%Si steel as shown in Figure 3(b). At aluminum contents higher than 6%, it is still possible to achieve fully austenitic solidification with higher carbon contents. However, increasing carbon increases the stability of kappa carbide on grain boundaries and reduces the toughness of aged FeMnAl steels.[25] Based on these simulations, a composition of Fe-30%Mn-5.6%Al-1.5%C-1%Si was chosen for experimental grain refinement trials with fully austenitic solidification, low density, and age hardenability.

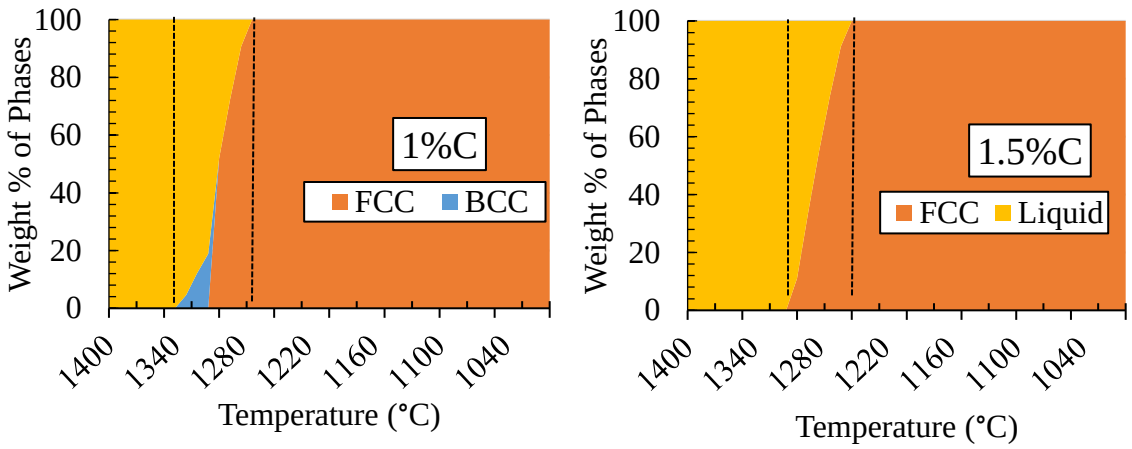

(a) (b)

Figure 3. Thermodynamic equilibrium modeling of the solidification sequence of a Fe-30%Mn-5.6%Al-1%Si steel with (a) 1% and (b) 1.5% C.

2.2. DETERMINATION OF INOCULANT INCLUSIONS

The lattice parameter for austenitic stainless steels reported in the literature ranges from 0.368 to 0.371nm at 1650K and from 0.356nm to 0.359nm at room temperature. A

value of 0.369nm is reported for Fe – 30Mn – 9Al – 0.9C – 1Si steel at room temperature.[3,5,26,27] For a Fe – 30%Mn – 5.6%Al – 1.5%C – 1%Si steel, the lattice parameter a_γ was calculated using the experimental relationship (Eq. 5) to be 0.3664nm at room temperature.[28] The linear expansion from room temperature to solidification temperature (1300-1350°C) will increase a_γ to 0.3772nm.[29]

$$a_\gamma = 0.3570 + 0.000065\ \%Mn + 0.00095\ \%Al + 0.0021\ \%C - 0.00101\ \%Si \qquad (5)$$

The lattice misfit at 1350°C, between austenite and selected inclusions was calculated using Eq. 2. A composition of *Fe* – 30%*Mn* – 5.6%*Al* – 1.5%C – 1%Si was used as a reference for determining the lattice parameters. The lattice misfit was calculated for three directions of each crystal structure and results are listed in Table 1.

Bramfitt suggests that a lattice mismatch below 12% may constitute a potent grain refiner, however, other studies suggest a value of 6% or less.[17,20] The lowest lattice misfits (<12%) with the austenite were calculated for Al_2MgO_4 (7.9%). However, it is important to note, that lattice misfit is merely an indicator of nucleation potential and the actual interfacial energy will depend on several other factors such as the similarity of chemical bonding and the effect of surface active elements that may help or hinder wetting of the liquid.

The current study therefore focuses on TiN as a potential grain refining addition in a composition that solidifies as primary austenite, Fe-30%Mn-5.6%Al-1.5%C-1%Si. The Ti-based inclusions were selected due to successful results in other systems as they have been shown to produce grain refinement in cast 316L.[5,32]

Table 1. Lattice misfit between austenite in a Fe – 30%Mn – 5.6%Al – 1.5%C – 1%Si steel and selected nonmetallic inclusions at 1350°C.[13, 21, 22, 30]

Inclusion	Lattice Parameter (nm)	Orientation Relationship	[uvw] Precipitate	[uvw] Substrate	δ%
TiC	0.4376	(100)TiC//(100)γ-Fe	[010] [110] [001]	[010] [110] [001]	13.8
TiN	0.4297	(100)TiN//(100) γ-Fe	[010] [110] [001]	[010] [110] [001]	12.2
TiO_2	a=0.4653 c=0.2999	(110)TiO_2//(100) γ-Fe	[001] [111] [110]	[010] [110] [001]	21.2
MgO	0.4299	(100)MgO//(100) γ-Fe	[010] [110] [001]	[010] [110] [001]	13.9
Al_2MgO_4	0.407	(100)Al_2MgO_4//(100)γ-Fe	[010] [110] [001]	[010] [110] [001]	7.9
Austenite	0.3772	-	-	-	-

All factors associated with grain refining, including the alloy solidification path, the lattice disregistry of precipitates with the solidified phase, as well as the stability of grain refining precipitates in the molten steel, should be considered. The prospective grain refiner should be stable above the liquidus temperature as a solid particle. This is a common limiting characteristic for several grain refiners such as NbC and $MnSiO_3$ in low alloy steels.[11,31] The stability of possible heterogeneous nuclei for different steel systems has commonly been evaluated by equilibrium thermodynamic simulations at liquid steel temperatures.[3,16,32] Based on the lattice mismatches calculated in Table 1, the stability of Ti(C,N) was modeled as a function of temperature using ThermoCalc software. The residual values for 10 ppm oxygen, 50 ppm nitrogen, and 60 ppm sulfur were selected from previous unpublished studies.

Figure 4 shows that Ti additions will form solid solution carbonitrides. The molar composition of these inclusions ranges from Ti($C_{0.55}$,$N_{0.45}$) to Ti($C_{0.8}N_{0.2}$) depending on the temperature with higher nitrogen at higher temperatures. The addition of 0.10% titanium produced Ti(C,N) at 85°C superheat, which is below pouring temperature. Thus, at this concentration, Ti is unlikely to have any effect on grain refinement unless nitrogen is increased to greater values to increase its stability. For an addition of 0.30%Ti, precipitation of Ti(C,N) occurs approximately 320°C above liquidus temperature. In this case, AlN is suppressed and only occurs at a temperature above 1610°C. Increasing Ti to 0.5% increases the amount of Ti(C,N) to around 0.6% and fully suppresses AlN. The stability of Al_2O_3 and MnS were unchanged by additions, so those were omitted from Figure 4.

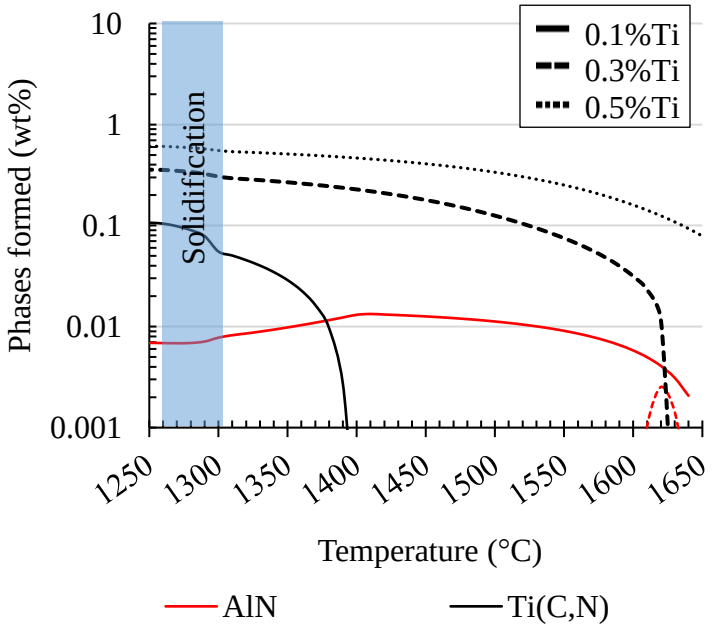

Figure 4. Thermodynamic simulation of equilibrium conditions with the addition of Ti, showing the phases formed in weight percent and the solidification range. The solid lines are for the lower additions and dashed for increasing content.

The models show limitations in the minimum addition needed to produce the desired non-metallic inclusions above the liquidus temperatures. The nucleation rate will depend on the active number of nuclei and a TiN volume fraction of 0.05% was suggested by the authors to be effective for a 319 stainless steel.[3] The titanium additions were shown by thermodynamic calculations to form stable Ti(C,N) inclusions in the liquid steel above at all additions level tested.

2.3. EXPERIMENTAL PROCEDURE

In the current study, inoculation was performed by the addition of preformed TiN inclusions in a master alloy.[33] That master alloy (MA) was developed for the introduction of TiN directly into the melt instead of the addition of ferrotitanium for in-situ formation of the Ti inclusions. An alloy based on Fe-Ni-Cr was produced from high purity charge and nitrided ferrochrome to produce a master alloy with a nominal chemistry of Fe-15%Ti-28%Ni-8.7%Cr-3%Al-1%N. The charge was melted in an induction melt furnace and cast into a no-bake sand ingot mold. The master alloy was then crushed to <1/2in. diameter particles prior to addition. The backscattered electron image of the master alloy is shown in Figure 5. The area fraction of TiN was determined by a SEM analysis as approximately 5%.

A target composition of Fe-30Mn-5.6Al-1.5C-1.0Si was chosen for this study. The steel heats were produced in a coreless induction furnace under a continuous argon flow of 25 scfm in an MgO crucible. The charge material was composed of high purity induction iron, graphite, ferrosilicon, 1020 aluminum, and electrolytic manganese, added in this sequence. The melt procedure was similar in all heats. Prior to tapping, slag was

removed and the melt was transferred to an MgO ladle. The master alloy additions were performed by plunging the addition into the steel melt in the ladle utilizing steel foil bags attached to a steel bar. All stirring, additions, and de-slagging was performed using low carbon steel rods to minimize contamination. The steel heats were lip poured into no-bake silica sand molds at 1530°C, 1517°C and 1484°C, respectively. The chemistries of the steel heats are presented in Table 2.

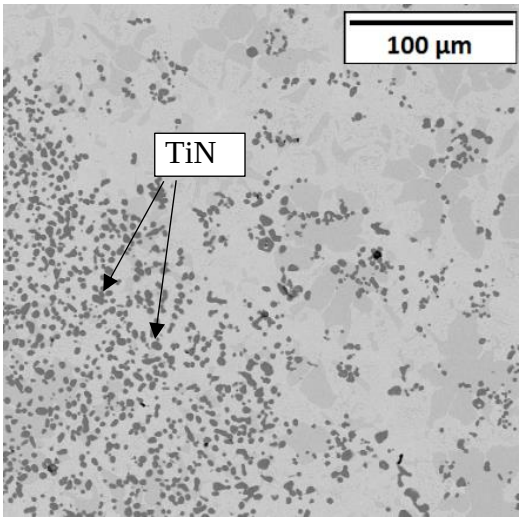

Figure 5. Secondary electron image of the polished microstructure of the master alloy used. The matrix was determined by EDS to be composed of Fe-Cr-Ni-Al-Ti, and the dark gray precipites are TiN.

The casting design is shown in Figure 6. It employed a cylindrical exothermic sleeve as the mold, with a 1" thick steel chill plate at the bottom to induce directional solidification. After filling of the mold, 1" of hot topping compound was added to the top of the mold.

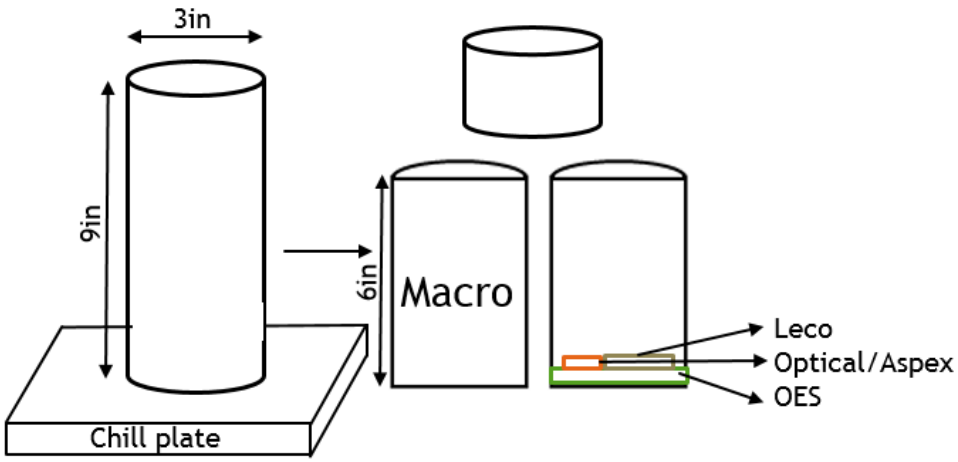

Figure 6. Steels were cast into a 3" diameter cylinder mold on top of a low-carbon steel chill plate and with 1" of hot topping.

The chemistry analyses were performed by optical emission arc spectroscopy (OES) in a Foundry-Master arc spectrometer from Oxford Instruments. Standards of steels with comparable Mn, Al, and Si contents were used for calibration. The total oxygen, nitrogen, carbon, and sulfur contents were measured by combustion methods using a LECO O-N analyzer and a LECO C-S analyzer. Samples for inclusion analysis and optical microscopy were prepared by using standard metallographic techniques. The castings were sectioned longitudinally using a water-cooled abrasive saw. Samples for chemistry and inclusion analysis were taken from the regions marked in orange. Samples for macro etching were obtained from the longitudinal section of the cylinder. A 10% Nital solution was used as an etchant for the microstructural evaluation. Macro etching was accomplished with a solution of 50%vol. HCl, 25%vol. HNO_3 and 25%vol. H_2O for 30-300 s, as recommended for high alloyed steels in ASTM E340-15. Measurements of grain size and secondary dendrite arm spacing (SDAS) were performed by optical

microscopy. The grain size was determined by manual delineation of grain boundaries of all grains in the equiaxed zone of the prepared surface. The software package ImageJ was used to measure the average grain area, and ASTM E112-13 was used to convert the measurement to an average grain diameter. The steels were etched with 10%Nital and, in some cases, followed by Klemm's etchant depending on which procedure created better contrast on the grain boundaries and on the dendritic microstructure.

Inclusion analysis was performed using an ASPEX PICA 1020 scanning electron microscope, SEM, with Automatic Feature Analysis, AFA, software and equipped with a backscattered electron detector, BSED, and an energy dispersive X-ray spectroscopy, EDS, detector. Inclusions were classified into nine different groups: AlN, AlN-MnO, AlN-MnS, MnS, Ca complex inclusions, Mn-Al-S-O, Ti complex inclusions, and porosity. Inclusions that were less than 2% of the total population were grouped into "Others". The overall inclusion population of a steel was taken as the average result of each one of the three locations marked in Figure 6.

3. RESULTS

3.1. CHEMISTRY AND MICROSTRUCTURAL EVALUATION

The chemistries of the steels are listed in Table 2. The results are very close to the calculated chemistry for the Fe-30Mn-5.6Al-1.5C-1Si steel. Total oxygen, nitrogen, and sulfur are good indicators of the number of inclusions in the steel castings. The total oxygen was generally low in all steels with a maximum value of 12ppm. Sulfur content was below 20ppm in the base heat and in the 0.5%MA steel, however, sulfur was

150ppm in the 1.5%MA steels. This is attributed to the larger fraction of electrolytic manganese fines used during melting of the 1.5%MA steel. Nitrogen is directly related to the stability and amount of Ti(C,N) formed. The nitrogen was 50ppm in the base heat and 93 ppm in 1.5%MA steel. Nitrogen is added to the melt during the addition of the master alloy since it has 0.28%N. If both Ti and N had 100% recovery, 20ppm of nitrogen would be added for every 0.1% titanium. The recovery of nitrogen would, therefore, be close to 100% in the 0.5%MA steel and 75% in the 1.5%MA steel.

The as-cast grain structure is shown in Figure 7 for all three steels. Solidification occurs directionally from the chill plate and is characterized by a columnar zone of over 70mm in length, followed by an equiaxed zone in the remaining portion of the casting. The addition of the master alloy did not decrease the columnar zone or refine the as-cast structure.

Table 2. Composition in wt.% and (ppm) as determined utilizing OES and LECO* combustion analysis.

Steel	**Mn**	**Al**	**C***	**Si**	**Ti**	**Cr**	**Ni**	**O***	**N***	**S***
#1 Base steel	29.6	5.58	1.48	1.28	0.01	0.08	0.09	(7)	(50)	(19)
#2 0.5%MA steel	29.9	5.53	1.48	1.27	0.09	0.12	0.18	(11)	(70)	(18)
#3 1.5%MA steel	30.7	5.09	1.43	1.18	0.29	0.20	0.42	(5)	(93)	(147)

The average grain sizes in the equiaxed zone are shown in Figure 8. The average equiaxed grain size of the base heat was 5.65 mm. The addition of the master alloy to the

steel increased the grain size slightly to around 6.90 mm in both the 0.5%MA steel and the 1.5%MA steel. This demonstrated that no grain refinement was achieved by adding the TiN master alloy in concentrations of up to 1.5%.

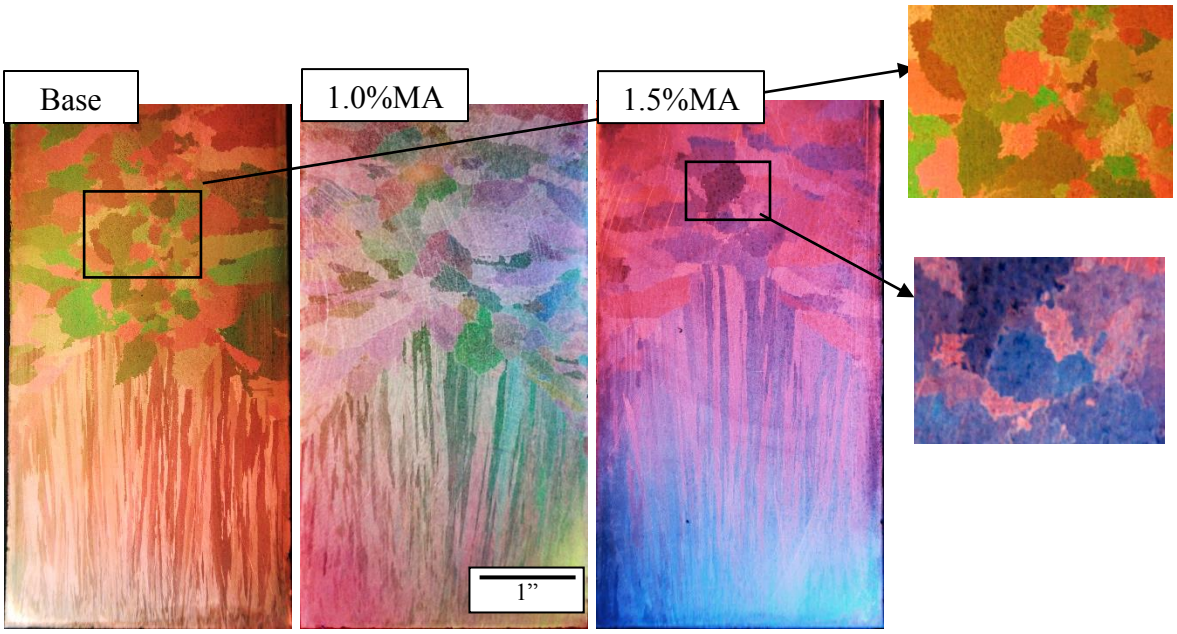

Figure 7. Macroetched structure of base steel (steel #1), 0.5%MA steel (steel #2), and 1.5%MA steel (steel #3) showing no decrease in grain size after MA addition.

Etching the microstructure of FeMnAlC steels with Nital reveals κ-carbide precipitation on grain boundaries and also tints the austenite, as shown in Figure 9 for a specimen sectioned 3” from the chill plate. The microstructure exhibited a coarse dendritic structure in all steels. The presence of retained δ-ferrite was not observed in any of the steels. The inclusion density was observed in optical micrographs to be higher after the master alloy was added, as shown in Figure 9. Isolated porosity was also

observed in small amounts in the interdendritic regions of all steels. As shown in Figure 10, the inclusions are located along grain boundaries as well as inside the grains. The steels displayed precipitation on grain boundaries and sub-grain boundaries and this is consistent with κ-carbide precipitation.

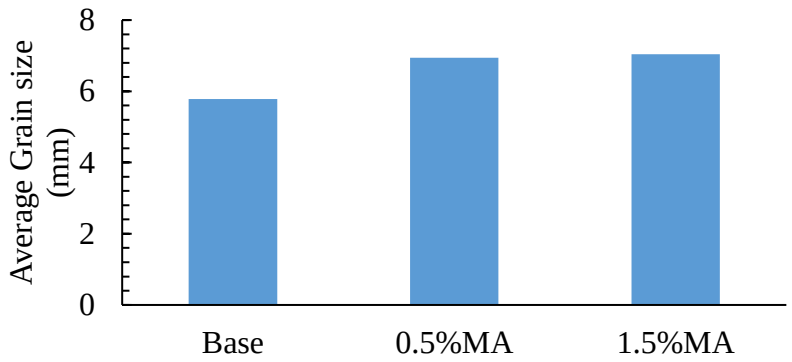

Figure 8. Average grain size measured from all of the equiaxed grains in optical images of the as-cast structure for the three steels.

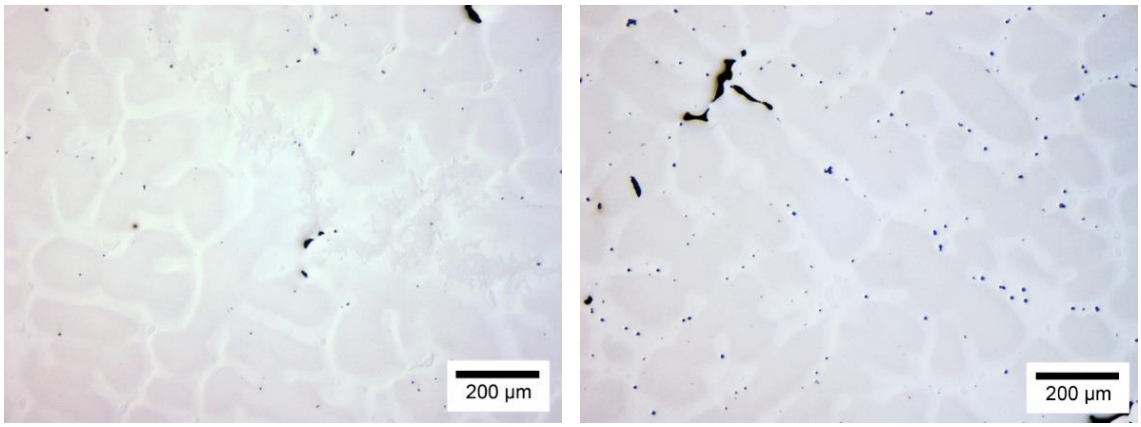

(a) (b)

Figure 9. Optical micrographs of (a) steel #1 without MA addition and (b) steel #3 with 1.5%MA at about 3” from the chill plate showing a dendritic structure in the un-etched condition.

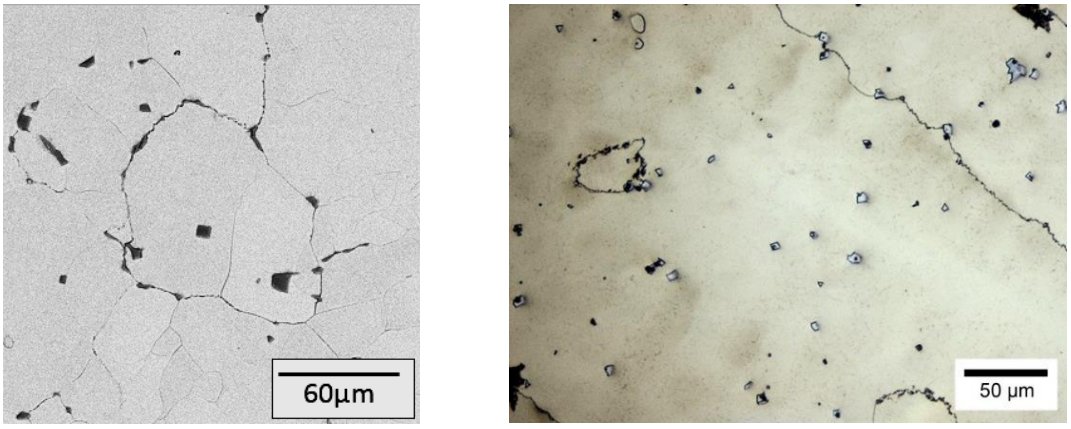

(a) (b)

Figure 10. (a) Backscattered electron image of the 1.5%MA steel and (b) optical image of the same steel. In (a), the dark particles are Ti(C,N) and in (b) those appear as a white/light gray inclusions.

3.2. INCLUSION ANALYSIS

The analysis of the inclusion population was studied utilizing an SEM with automated feature analysis. The results shown are an average of at least three scans on different samples with a total scanned area of greater than 20 mm^2 from each of the castings. Samples were taken from three locations as shown in Figure 6 and the average was reported. The classification of the inclusions was performed according to their composition as measured by EDS. As an example, the average chemistry of the more than 700 inclusions present in each steel is shown in Table 3. Backscattered electron images for the most common type of inclusion in steels #1, AlN-MnS, is shown in Figure 11 along with a joint ternary diagram. This diagram represents each inclusion by the three major components, in weight %. For steel #1 majority of inclusions are in ternaries of Mn-Al-N and Mn-Al-S. In Figure 12, for steels #2 and #3, the largest numbers of

inclusions were titanium containing inclusions fitting into the Mn-Ti-N, Mn-Ti-Al, and Mn-Ti-S ternary diagrams.

Table 3. Average EDS chemistries in wt.% of the inclusions analyzed in steel #1 and for the Ti-based inclusions in steels #2 and #3.

	Inclusion	C	N	Mg	Al	Si	S	Ti	Mn
Steel #1	AlN	0.0	24.5	0.0	60.2	0.0	0.7	0.0	14.6
	AlN-MnS	0.04	17.3	0.0	41.6	0.0	6.7	0.2	34.2
	MnS	1.21	0.6	0.0	0.5	0.0	16.8	0.0	80.9
	Ti-Based	2.53	10.6	0.0	27.2	0.0	5.2	15.8	38.7
	Others	0.7	16.2	0.1	39.7	0.4	2.5	0.1	40.3
	All	0.3	20.2	0.1	53.2	0.1	3.2	0.3	22.6
Steel #2	Ti-based	3.29	8.31	0.0	7.92	0.03	1.63	53.24	25.57
	All	2.9	12.0	0.1	17.6	0.4	1.8	45.5	19.7
Steel #3	Ti-based	3.24	4.86	0.0	6.59	0.02	3.01	59.47	22.82
	All	3.0	6.4	0.0	10.8	0.1	3.0	59.7	17.0

	Wt%
Mn	30.3
S	8.8
Al	48.1
N	12.9

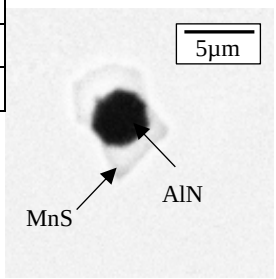

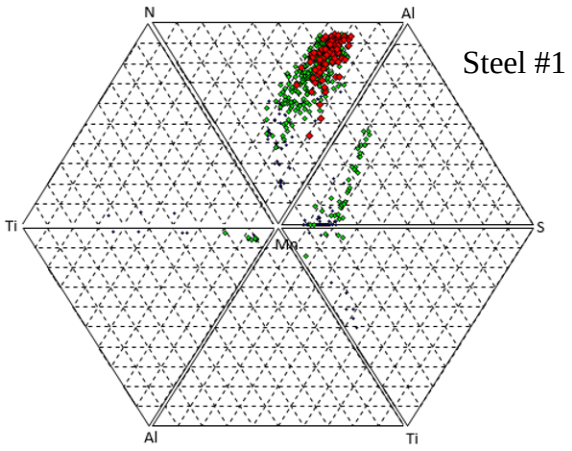

Figure 11. Backscattered electron image of a typical AlN-MnS inclusion in the base steel. A joint ternary diagram represents each inclusion and shows that inclusions in the base steel are mainly AlN and AlN-MnS complex inclusions.

	Wt%(1)	Wt%(2)
Mn	16.2	29.5
S	0.0	5.6
Al	1.3	5.8
N	3.3	11.1
Ti	75.5	46

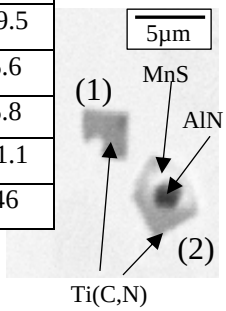

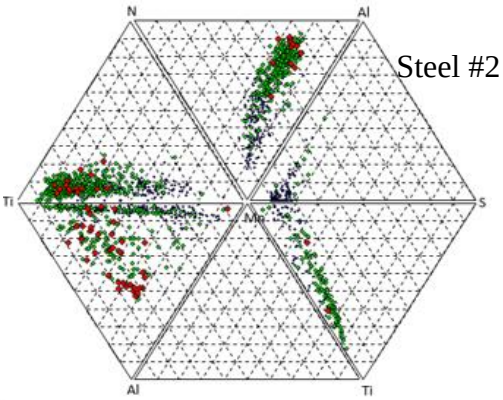

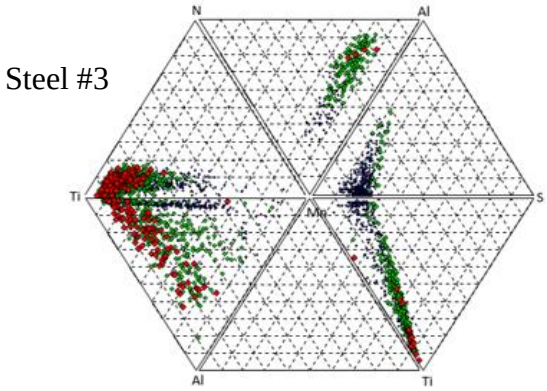

	Wt%
Mn	4.6
S	0.0
Al	1.1
N	6.1
Ti	84.9

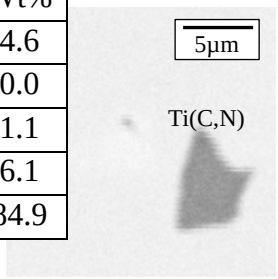

Figure 12. Joint ternary phase diagrams and backscattered electron images of Ti-based inclusions found in steels with the 0.5 and 1.5%MA addition, steels #2 and #3. Results show that the Ti-based inclusions are mainly Ti(C,N) inclusions. Some Ti-based inclusions are complex in nature with MnS and AlN co- precipitation.

The inclusion population densities of the steels are shown in Figure 13. In the base steel without the addition of the TiN master alloy, the inclusions were mostly AlN, MnS and complex AlN-MnS. Only a few Ti(C,N) inclusions were present due to residual Ti present in the initial charge. Average inclusion density in the base steel was 55 #/mm^2. After the addition of the TiN master alloy, the majority of the inclusions present were titanium-based complex inclusions that were co-precipitated with MnS and AlN as shown in Figure 12. The number density of Ti(C,N) is shown in Figure 13(b) for the three steel castings. The addition of master alloy produced a Ti(C,N) density of 145 #/mm^2 in the

steel with 0.5%MA and 440 #/mm^2 in the 1.5%MA steel. In steels #2 and #3, Ti(C,N) constitutes over 90% of the total inclusions.

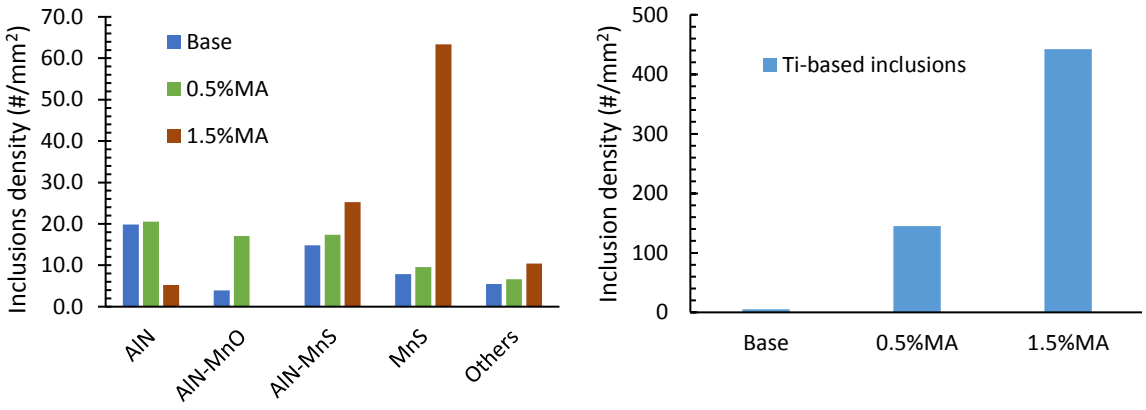

(a) (b)

Figure 13. (a) Inclusion number density of steels with 0, 0.5, and 1.5% MA additions as a function of inclusion type. (b) The Ti(C,N) inclusion population is shown separately because of the large percentage of these inclusions in the steels with MA addition. The impact of higher sulfur content in the 1.5%MA added steel is demonstrated by the large increase in MnS.

4. DISCUSSION

The experimental results show that addition of TiN inclusions in the form of a TiN master alloy to the Fe-30Mn-5.5Al-1.5C-1Si steel melt did not show detectable grain refinement of the as-cast macrostructure or microstructure as shown in Figure 7 and 8. However, a recent study showed that use of the same TiN-master alloy reduced the columnar zone by a grain refining factor of 0.8 produced an equiaxed grain size of 2-7mm in directionally solidified austenitic 316L castings with a similar mold design as used in the current study.[33] In a similar study, a decrease in grain size from 2.35mm to

0.70mm was also achieved.[5] This can be compared to the measured equiaxed grain size for the lightweight steel in the current study of 5.8 to 7.0mm

To expand the analysis for possible improvements of the microstructure, the secondary dendrite arm spacing (SDAS) was calculated and is shown in Figure 14. The secondary dendrites could be observed due to differential etching in interdendritic areas. The master alloy additions were shown to have little to no influence on the SDAS. The high thermal gradient resulted in an SDAS that was a strong function of position away from the steel chill. Measurements were at 1", 3", and 5" away from the chill plate. The SDAS ranged from 20-40 μm in position 1, much smaller than SDAS measurements at position 3 at 90-130 μm.

The as-cast microstructure of the steels consisted of a matrix of 100% austenite as shown in Figure 9 and that is consistent with the thermodynamic models presented in Figure 3(b) for the Fe-30Mn-5.5Al-1.5C-1Si steel. Ferrite was not observed in any of the castings. The inclusion analysis in Table 3 shows that the inclusions present were not the desired TiN, but actually Ti(C,N). The two inclusions are very similar, and they have the same crystal structure with a similar lattice parameter of 0.433μm (TiC) and 0.424μm (TiN).[21] TiC has a lattice mismatch with austenite of 14.8% while the TiN has a mismatch of 13.1%. This difference suggests that TiN may be a better candidate for grain refinement in these steels.

In order to explain this behaviour, thermodynamic simulations were performed using ThermoCalc 2017a with the TCFE9 database. The phase stability diagram, shown in Figure 15, was used to determine the stable precipitates that form in the liquid for a steel with composition of Fe-30Mn-1.5C-1.2Si-0.009N-yAl-xTi. The red dots represent

the compositions of the steels in the current study. Models were performed above the liquidus at temperatures of 1350 and 1500°C, respectively, as shown in Figure 15(a) and 15(b). The phase stability diagram shows that for the base steel without MA additions, AlN is stable near the liquidus well above 1500°C. When 0.5%MA is added to the steel, mixed AlN and Ti(C,N) is stable near liquidus and at 1500°C. For the steel with 1.5%MA however, Ti(C,N) is stable at 1500°C and below.

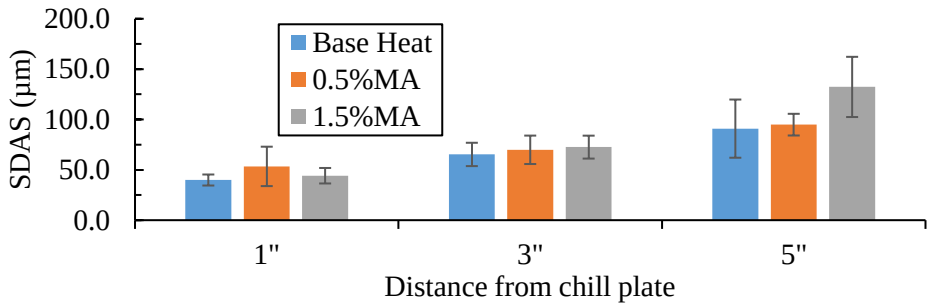

Figure 14. Secondary dendrite arm spacing, as measured from optical microscopy images, increases with distance from the chill plate.

The presence of Ti(C,N) instead of the targeted TiN was also predicted by simulations in Figure 4, however, since the inclusions were introduced into the melt by use of a master alloy with preformed TiN it was possible to have these particles survive and be present in the liquid. As shown in Figure. 12, the inclusions formed in the current study were cubic Ti(C,N) and were of different composition and shape from the TiN in the master alloy addition shown in Figure. 5. In addition, the Ti(C,N) was shown to precipitate around pre-existing AlN inclusions in the alloy with the 0.5MA addition. This is consistent with the modeling results in Figure. 15 which show that AlN and Ti(C,N)

are stable above 1500°C. It is obvious that at least some partial melting of the TiN in the master alloy addition occurred with re-precipitation of Ti(C,N) around pre-existing AlN or on TiN. It should be noted that formation of Ti(C,N) does not necessarily dictate an inability to be a suitable grain refining inoculant for austenitic steel. Successful examples of the use of Ti and Nb carbides to refine steels with austenitic solidification are present in the literature, for example, by in-situ formation of TiC in cast 1045 steel or by addition of premade NbC master alloy in a 316L steel.[11, 34]

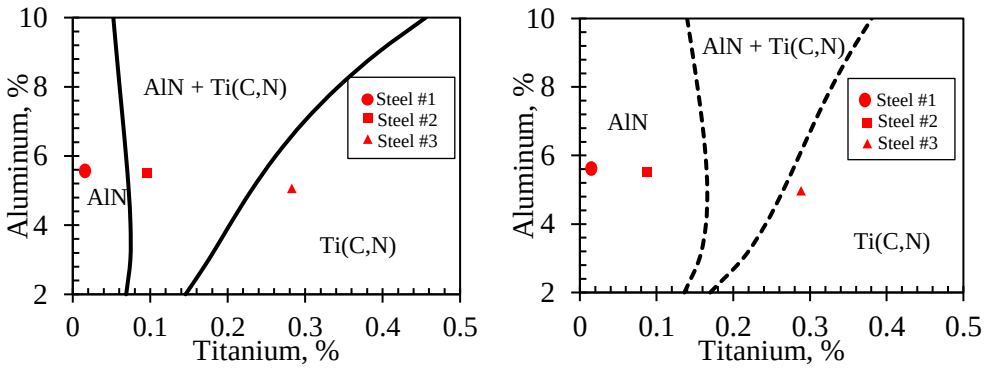

Figure 15. Thermodynamic simulation of the type of inclusion stable for different Al and Ti contents at (a) 1350°C and (b) 1500°C. Simulations were done above the liquidus temperature.

The heterogeneous nucleation rate is also dependent on the size and distribution of the nucleating particles. Therefore, a large volume fraction of nuclei with a large surface area is desirable. Literature suggests that grain refinement is also facilitated by larger inclusions.[35]. At a specific volume fraction of particles, the number of particles will

be inversely proportional to the diameter of the particles. Due to these opposing trends, a specific inclusion size range optimizes grain refinement. For an Mg-alloy, it was experimentally determined that Al_2Y particles with average diameter of 6-6.5 μm were the optimal size to refine the as-cast grain size in this system.[36] The same study also suggested that inclusions with less than 2 μm do not act as heterogeneous nuclei.

The size distributions of the inclusions formed for each of the steels in the current study are shown in Figure 16. The bin size used was a geometrical distribution where each bin is smaller than the previous one by a factor of $10^{-0.1}$. Considering the 2 μm threshold, around 40-48% of the inclusions formed are not suitable for grain refinement. The number of inclusions below the size threshold could be much larger considering that there is plenty of time for inclusions to coarsen during solidification. The average size was 2.7 μm for steel #2 with a 0.5%MA addition and 2.5 μm for steel #3 with a 1.5%MA addition. In both steels, 90% of the inclusions were less than or equal to 5 μm in size. The inclusion distribution for the base steel had a larger average of 4.1 μm and the majority of inclusions were from 3 to 6 μm in diameter. In a recent study using TiN to grain refine austenitic stainless 316L, the authors achieved grain refinement with 180 to 374 inclusions/mm^2.[5] Figure 13(b) shows that steel #3 in the current study had 440 inclusions/mm^2, which means over 200 inclusions/mm^2 were within the 2-5 μm range.

Surface active elements can also affect the effectiveness of a heterogeneous nucleation site. Sulfur is a surface active element and the high Mn content of the steel may encourage sulfur adsorption onto the surface of the Ti(C,N). This may interfere with the ability of iron atoms to adsorb to the surface of the heterogeneous nucleation site. Some of the Ti inclusions in the current study were found to be associated with MnS

precipitation and this may have prevented the Ti(C,N) from being effective as a heterogeneous nuclei for austenite solidification. Adsorption of sulfur onto the surface of the Ti(C,N) may have increased the Fe adsorption energy and thus the nucleation potential. The Ti-based inclusions were therefore separated into inclusions with and without the presence of AlN and MnS. A threshold above 5% sulfur was used to identify presence of MnS and a threshold above 5%Al to identify presence of AlN. The results are shown in Figure 17. Over 60% of the Ti(C,N) in steels #2 and #3 were free of any distinguishable co-precipitation. This suggests that MnS co-precipiation was not responsible for poisoning all of the inclusions nucleation sites. In addition, thermodynamic simulations shown in Figure 18 predict the formation of MnS only at very last liquid to solidify and it could not influence the steel solidification. On the other hand, the precision of the thermodynamic software on predicting the stability of MnS in a steel with such high alloying, especially high manganese might need further verification.

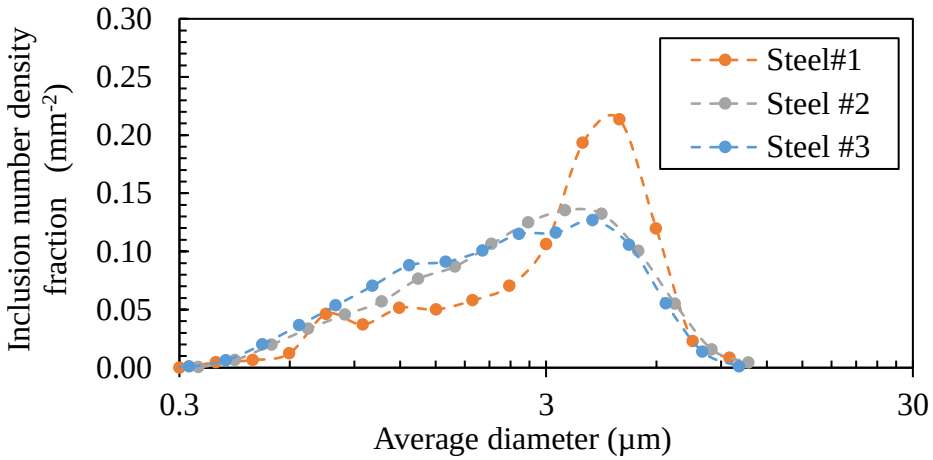

Figure 16. Average diameter distribution of nonmetallic inclusions recorded in the steels. The inclusion population on steels #2 and #3 after addition of the MA alloy had a wider size distribution and a smaller average diameter than the base steel.

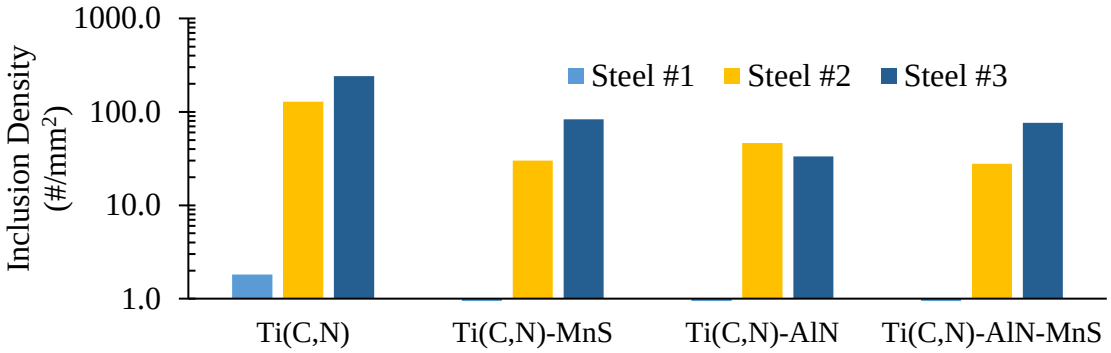

Figure 17. Much of the Ti-based inclusions were of the complex type in which Ti(C,N) was found to precipitate on pre-existing AlN. At lower temperatures MnS was also shown to precipitate around Ti(C,N), especially in Steel #3 with the highest sulfur content.

A possible explanation for why grain refinement was achieved in other systems but not in Fe-Mn-Al-C steels might be due to the interaction of individual alloying elements on the interfacial energy of the nucleating interface. Analysis of the binding energy between Fe and different carbides by *ab initio* calculations suggest that specific alloying elements can create an intermediate layer and modify this energy. Adsorption of Fe onto MC carbide surface should be facilitated by alloying with Mn.[37] However, such results were not shown experimentally. The formation of an interface reaction layer between the inclusion and the liquid can hinder or aid in nucleation. Grain refinement suppression by Zr, Si, Cr, and Mn has been observed in aluminum alloys.[38] In addition, Schumacher and Greer observed formation of intermediary layer of Al_3Ti between TiB_2 and α-Al in an aluminum-based alloy ($Al_{85}Y_8Ni_5Co_2$, in at%) and attributed the formation of Al_3Ti to the grain refinement of the alloy.[39-41]

Equilibrium modeling predicts the stability of $Ti_4C_2S_2$ at temperatures above 1440°C as shown in Figure 18. The $Ti_4C_2S_2$ phase was never observed in samples taken

from the furnace or the casting and was not considered in previous simulations. The boundary between Ti(C,N) and the liquid steel might be a better surface for $Ti_4C_2S_2$ to nucleate, similar to the formation of Al_3Ti on the surface of TiB_2 on aluminum systems.[41] The $Ti_4C_2S_2$ has an hexagonal crystal structure with lattice constants at ambient temperature of a=0.3209 nm and c=1.1210 nm.[42] In addition to a different crystal structure, the lattice misfit for the $Ti_4C_2S_2$ is around 20%, much larger than that of TiC/TiN.

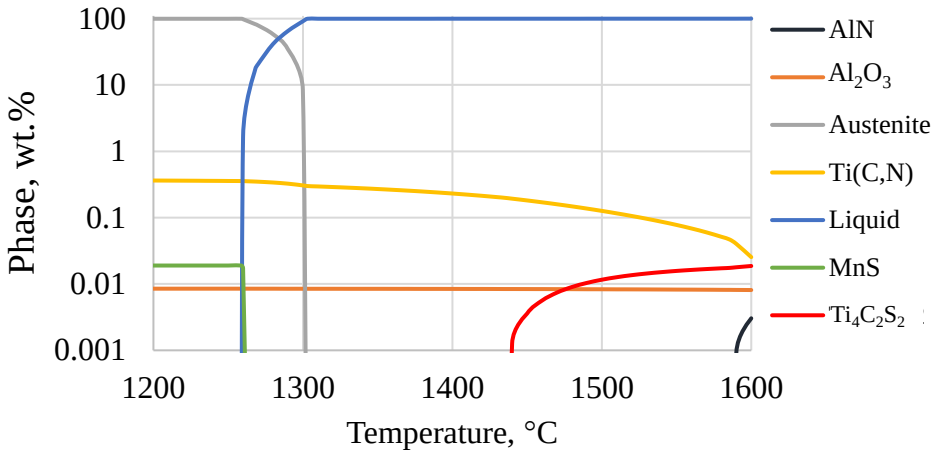

Figure 18. Equilibrium solidification modeling of a Fe-30Mn-5.6Al-1.5C-1Si-0.006N-0.004N-0.007S-0.3Ti steel shows the formation of $Ti_4C_2S_2$ well above the liquidus.

A recent study of grain refinement of a high manganese alloy with a nominal Fe-1%C-11%Mn-1%Si composition also did not observe grain refinement of the grain structure by Ti addition.[13] This could suggest that the high Mn content might be affecting the interfacial energy. This could happen either by increasing the absorption energy,

which would go against the calculations predicted in literature, or creating an intermediary phase between the TiC and TiN with austenite.[37]

The above discussion shows that future studies are needed to understand the evolution of inclusions in these steels as a function of melt practice. It may be possible to increase the stability of TiN in these steels by controlled melt additions to limit AlN and produce in situ TiN. A low sulfur melt practice should also be used to limit possible poisoning of heterogeneous nuclei. Future studies will focus on the influence of manganese and other alloying elements on the ability of Ti(C,N) to act as a nucleation site for both austenite and ferrite in Fe-Mn-Al-C alloys.

5. CONCLUSION

The potential of different inclusions to induce grain refinement during solidification of fully austenitic Fe-30Mn-5.6Al-1.5C steels was evaluated through lattice mismatch calculations and thermodynamic calculations. TiN presented a mismatch of 13.1% with austenite and was evaluated as a potential grain refining addition for nucleation of austenite based on previous success in an AISI 316L steel.

The addition of a master alloy containing a high density of TiN particles to the steel melt was shown to generate an area fraction of up to 0.4% of Ti(C,N) at a 1.5%wt addition of master alloy. The Ti(C,N) inclusions were present at grain boundaries and within the grains and this implies that some dissolution of the TiN occurred with re-precipitation as Ti(C,N) as well as possible rapid diffusion of C into the TiN. Grain refinement was not observed in any of the castings. The average grain size measured

from the equiaxed region of the test casting was determined to be 5.7 mm^2 in the base heat and above 6.9 mm^2 in the steels with the addition of 0.5 and 1.5%wt of the master alloy. No decrease in the columnar region or SDAS was observed. Although many of the Ti(C,N) were of the complex type with MnS co-precipitation, the majority of inclusions were free of precipitation. This implies that most of the Ti-inclusions could have served as nucleation sites without a possible poisoning effect by other nonmetallic inclusions.

Therefore, use of TiN as a grain refiner in fully austenitic FeMnAlC steel was shown to be inefficient for the conditions tested. Comparison with other studies that used TiN inoculation suggests that an interaction between the high content of alloying elements in the steel, specifically manganese and sulfur may be influencing the adsorption energy of Fe onto the dispersoid surface or producing a nanoscale reaction layer that may be less favorable for nucleation.

REFERENCES

1. Bartlett, Laura, and David Van Aken. "High Manganese and Aluminum Steels for the Military and Transportation Industry." *JOM*, vol. 66, no. 9, 2014, pp. 1770-1784.

2. Kim, Hansoo, et al. "Fe–Al–Mn–C lightweight structural alloys: a review on the microstructures and mechanical properties." *Science and Technology of Advanced Materials*, vol. 14, no. 1, 2013, p. 014205.

3. Lekakh, Simon N., et al. "Optimization of Melt Treatment for Austenitic Steel Grain Refinement." Metallurgical and Materials Transactions B, vol. 48, no. 1, 2016, pp. 406-419.

4. Morris, J. W. "The Influence of Grain Size on the Mechanical Properties of Steel." 2001.

5. Arvola, D. *Grain refinement of high alloy stainless steels in sand and directionally solidified castings*. Missouri U of Science and Technology, MS Thesis, Rolla, MO. Accessed 2018.

6. Grong, Øystein, et al. "Microstructure Control of Steels through Dispersoid Metallurgy Using Novel Grain Refining Alloys." ISIJ International, vol. 46, no. 6, 2006, pp. 824-831.

7. Haakonsen, F., Solberg, J. K., Klevan, O. S., & Van der Eijk, C. Grain Refinement of Austenitic Manganese Steels. In *AISTech Proceedings*. AIST. 2011.

8. Bartlett, Laura N., and Bryan R. Avila. "Grain Refinement in Lightweight Advanced High-Strength Steel Castings." International Journal of Metalcasting, vol. 10, no. 4, 2016, pp. 401-420.

9. Andersson, M., Janis, J., Holappa, L., Kivio, M., Naveau, P., Brandt, M., … Van der Eijk, C. *Grain size control in steel by means of dispersed non-metallic inclusions - GRAINCONT: Final report*. Luxembourg: Publications Office of the European Union, 2011.

10. Li, Ming, et al. "A New Grain Refiner for Ferritic Steels." Metallurgical and Materials Transactions B, vol. 48, no. 6, 2017, pp. 2902-2912.

11. Mizumoto, M., et al. "Development of new additive for grain refinement of austenitic stainless steel." International Journal of Cast Metals Research, vol. 21, no. 1-4, 2008, pp. 49-55.

12. Kucharczyk, J. W., Funk, K. R., & Kos, B. *U.S. Patent No. US 6,572,713 B2*. Washington, DC: U.S. Patent and Trademark Office, 2003.

13. Siafakas, D. *On deoxidation practice and grain size of austenitic manganese steel, MS T*hesis, Jonkoping, Sweden. Accessed 2017.

14. Leslie, W. C. *The Physical Metallurgy of Steels*. Hemisphere Publishing, 1981.

15. Dahle, E. S. *Grain refinement of high alloyed steel with cerium addition* (Unpublished). Norwegian University of Science and Technology, Trondheim, 2011.

16. YANG, Jian, et al. "Effect of RE oxide on growth dynamics of primary austenite grain in hardfacing layer of medium-high carbon steel." Journal of Rare Earths, vol. 30, no. 8, 2012, pp. 814-819.

17. Bramfitt, Bruce L. "The effect of carbide and nitride additions on the heterogeneous nucleation behavior of liquid iron." Metallurgical Transactions, vol. 1, no. 7, 1970, pp. 1987-1995.

18. Van der Eijk, C., Haakosen, F., Klevan, O. S., & Grong, O. Development of Grain Refiner Alloys for Steels. In *AISTech Proceedings*, 2011.

19. Dahle, E. S. *Grain refinement of high alloyed steel with cerium addition*. Norwegian University of Science and Technology, Doctoral Thesis, Trondheim, Norway, 2011.

20. Gao, Jinzhu L., et al. "Effects of Rare Earth on the Microstructure and Impact Toughness of H13 Steel." Metals, vol. 5, no. 1, 2015, pp. 383-394.

21. Tuttle, R. "Examination of Steel Castings for Potential Nucleation Phases." International Journal of Metalcasting, vol. 4, no. 3, 2010, pp. 17-25.

22. ThermoCalc V7.0 Software, TCFE9 Steels/Fe-Alloys V9.0, 9-13-18.

23. Chen, Shangping, et al. "Current state of Fe-Mn-Al-C low density steels." Progress in Materials Science, vol. 89, 2017, pp. 345-391.

24. Howell, R. A., Lekakh, S. L., Van Aken, D. C., Richards, V. L., "The Effect of Silicon Content on the Fluidity and Microstructure of Fe-Mn-Al-C Alloys," AFS Transactions (2008).

25. Kalashnikov, I., et al. "Chemical Composition Optimization for Austenitic Steels of the Fe-Mn-Al-C System." Journal of Materials Engineering and Performance, vol. 9, no. 6, 2000, pp. 597-602.

26. Nascimento, F. C., Foerster, C. E., Silva, S. L., Lepienski, C. M., Siqueira, C. J., & Alves Junior, C. (2009). A comparative study of mechanical and tribological properties of AISI-304 and AISI-316 submitted to glow discharge nitriding. *Materials Research*, *12*(2), 173-180. doi:10.1590/s1516-14392009000200011

27. Onink, M., et al. "The lattice parameters of austenite and ferrite in Fe-C alloys as functions of carbon concentration and temperature." Scripta Metallurgica et Materialia, vol. 29, no. 8, 1993, pp. 1011-1016.

28. Chu, C.M., et al. "Effect of alloying chemistry on the lattice constant of austenitic Fe-Mn-Al-C alloys." Scripta Metallurgica et Materialia, vol. 30, no. 4, 1994, pp. 505-508.

29. Ławrynowicz, Z. (2013). Bainite Transformation in Experimental Fe-Cr-Mo-V-Ti-C Steel. *Advances in Materials Sciences*, *13*(2). doi:10.2478/adms-2013-0005

30. Aigner, K., Lengauer, W., Rafaja, D., & Ettmayer, P. (1994). Lattice parameters and thermal expansion of Ti(CxN1−x), Zr(CxN1−x), Hf(CxN1−x) and TiN1−x from 298 to 1473 K as investigated by high-temperature X-ray diffraction. *Journal of Alloys and Compounds*, *215*(1-2), 121-126. doi:10.1016/0925-8388(94)90828-1

31. YANG, Jian, et al. "Effect of RE oxide on growth dynamics of primary austenite grain in hardfacing layer of medium-high carbon steel." Journal of Rare Earths, vol. 30, no. 8, 2012, pp. 814-819.

32. Sasaki, Masayoshi, et al. "Refinement of As-cast Austenite Grain in Carbon Steel by Addition of Titanium." ISIJ International, vol. 49, no. 9, 2009, pp. 1362-1366.

33. D. Arvola, S. Lekakh, R. O'Malley, and L. Bartlett, "Two Inoculation methods for refining as-cast grain structure in austenitic 316L steel," International Journal of Metalcasting, published online Sept. 2018 https://doi.org/10.1007/s40962-018-0260-1

34. Ohno, M., & Matsuura, K. (2008). Refinement of As-cast Austenite Microstructure in S45C Steel by Titanium Addition. ISIJ International, 48(10), 1373-1379. doi:10.2355/isijinternational.48.1373

35. Stefanescu, D. M. (2016). *Science and Engineering of Casting Solidification* (3rd ed.). Springer International Publishing.

36. Qiu, D., & Zhang, M. (2009). Effect of active heterogeneous nucleation particles on the grain refining efficiency in an Mg–10wt.% Y cast alloy. *Journal of Alloys and Compounds*, *488*(1), 260-264. doi:10.1016/j.jallcom.2009.08.100

37. Lekakh, S.N., and N.I. Medvedeva. "Ab initio study of Fe adsorption on the (001) surface of transition metal carbides and nitrides." Computational Materials Science, vol. 106, 2015, pp. 149-154.

38. Quested, T. E. (2004). Understanding mechanisms of grain refinement of aluminium alloys by inoculation. *Materials Science and Technology*, 20(11), 1357-1369. doi:10.1179/026708304225022359

39. Schumacher, P., & Greer, A. (1994). Enhanced heterogeneous nucleation of α-Al in amorphous aluminium alloys. *Materials Science and Engineering: A*, 181-182, 1335-1339. doi:10.1016/0921-5093(94)90858-3

40. Schumacher, P., & Greer, A. (1994). Heterogeneously nucleated α-Al in amorphous aluminium alloys. *Materials Science and Engineering: A*, 178(1-2), 309-313. doi:10.1016/0921-5093(94)90559-2

41. Schumacher, P., Greer, A. L., Worth, J., Evans, P. V., Kearns, M. A., Fisher, P., & Green, A. H. (1998). New studies of nucleation mechanisms in aluminium alloys: implications for grain refinement practice. *Materials Science and Technology*, 14(5), 394-404. doi:10.1179/mst.1998.14.5.394

42. Mao, X. (2019). *Titanium Microalloyed Steel: Fundamentals, Technology, and Products*. Retrieved from doi.org/10.1007/978-981-13-3332-3

III. PROGRESS IN GRAIN REFINEMENT OF FeMnAl CASTINGS. PART 2. TWO-STAGE INOCULATION WITH $MgAl_2O_4$ AND Ti(C,N)

Rairu Vaz Penna, Laura N. Bartlett

Missouri University of Science and Technology
Materials Science & Engineering Dept.
1400 N Bishop, Rolla, MO, U.S.A., 65409

Keywords: high manganese steels, grain refinement, nonmetallic inclusions, spinel, titanium

ABSTRACT

An in-situ two-stage inoculation method utilizing of $MgAl_2O_4$ (spinel) followed by co-precipitation of Ti(C,N) inclusions were investigated utilizing thermodynamic calculations and validated by experiments to produce grain refinement in a fully austenitic Fe-30Mn-5.6Al-1C-1Si steel. Spinel formation was accomplished with a small controlled addition aluminum followed by ferrosilicon-magnesium addition and then ferrotitanium addition to form Ti(C,N) in the melt. Inclusion development at various stages of steelmaking, during the inoculation process, and in the final castings was carefully studied utilizing electron microscopy, energy dispersive X-ray spectroscopy, and automated feature analysis. The results showed formation of spinel inclusions followed by nucleation of Ti(C,N) on their surface. The $MgAl_2O_4$-Ti(C,N) inclusions were also observed in the casting, but they did not have any effect on the average as-cast grain size. However, a melt practice was developed that utilized addition of titanium prior to the bulk aluminum addition that completely suppressed the formation of detrimental AlN inclusions and this may be an effective way to improve toughness in these steels.

1. INTRODUCTION

Austenitic FeMnAl steels are a class of steel derived from the Hadfield steels. Alloys in the chemistry range of 15-30%Mn, 5-10%Al, and 0.7-1.5%C have reduced of density up to 18% lower than quenched and tempered Cr and Mo martensitic steels.[1] The mechanical properties of these steels depend on composition and heat treatment and can range in ultimate tensile strengths (UTS) from 600-2000 MPa with up to 70% total elongation and with over 700 kJ/mm^2 of dynamic fracture toughness.[2,3] The main hardening mechanism for fully austenitic steels with greater than 6%Al and 0.5%C is the precipitation of nano-sized and homogenously distributed κ-carbide with a chemical formula of $(Fe,Mn)_3AlC_x$.[1]

Cast alloys are typically solution treated at 1050°C, water quenched, and aged in the temperature range of 500-600°C to precipitate the κ-carbide within the austenite matrix, greatly increasing hardness and strength. In these conditions, the yield strength can increase to as much as 1200 MPa, however further increases in strength require other hardening mechanisms such as refinement of the as-cast grain size.[1]

Inclusion control can be used to improve the total elongation and the toughness of the material but it has very little influence on the tensile strength.[4] If the inclusion population is engineered to control grain size, it can increase the yield and ultimate tensile strength by the Hall-Patch strengthening mechanism. Nonmetallic inclusions (NMI) can be engineered to have specific properties that promote austenite or ferrite nucleation during solidification. A large number of active nuclei increases the nucleation rate and this generates a larger number of grains with limited space for growth leading to

an overall reduction in grain size. Inclusions that are effective as heterogeneous nucleation sites should be thermodynamically stable in the liquid steel, have a low interfacial energy with the nucleating solid, present a large number density and a homogenous spatial distribution.[5]

The use of Ti-based inclusions for grain refinement of different steel alloys has been successful in several steel systems, including low and medium-carbon steels, as well as austenitic and ferritic stainless steels.[6-9] The most practical method is by addition of ferrotitanium added to the liquid steel. The titanium in solution reacts with carbon and/or nitrogen in the liquid to form a stable TiN/TiC in the liquid that act as a nuclei. Most recently, Arvola et al. developed a technique utilizing preformed TiN in the form of a master alloy addition to produce grain refinement in a 316L steel.[8] However, for in-situ formation of the Ti-based inclusion, intensive clustering has been observed.[7] The clustering decreases the number density of the substrates available for nucleation and this may consequently decrease the nucleation rate and thus decrease the grain refining efficiency. It was shown that clustering was greatly decreased by co-precipitating the TiN inclusions on pre-existing $MgAl_2O_4$ particles. It was also shown that this also increases the thermodynamic stability of the TiN.[7]

In addition to decreasing the clustering effect, spinel particles might also act as a substrate for nucleation of austenite. According to the calculation Arvola et al., $MgAl_2O_4$ has a lattice misfit of 7.9% with austenite while the TiN and TiC has a lattice misfit of 14.8 and 13.1%, respectively.[7] Further details on lattice misfit can be obtained in previously published papers.[10,11] The understanding of the formation of inclusions in FeMnAl steels can also improve other properties. Brittle and angular inclusions act as

stress concentration features and are detrimental to steel toughness. In FeMnAl steels, the presence of AlN is very common due to the high aluminum contents. It has been demonstrated that AlN is detrimental to the impact toughness of FeMnAl.[3,12] The in-situ formation of Ti-based inclusions has the possibility of removing nitrogen from solution and eliminating the formation of AlN inclusions. This study focused on the in-situ formation of Spinel and TiN for simultaneous inclusion control and grain refinement.

2. EXPERIMENTAL PROCEDURE

The target composition of the steels experimental steels was based on a steel with a complete austenitic solidification path at *Fe-30Mn*-5.*6Al*-1.5*C*-1.*0Si*. The steels were melted in a coreless induction furnace under a continuous argon flow of 25 scfm in a MgO crucible. The charging sequence for the base steel was high purity induction iron, graphite, ferrosilicon, 1020 aluminum, and then electrolytic manganese, respectively. The charging sequence was modified in the steels with added titanium. The aluminum was added last to avoid removing the nitrogen from solution prior to the titanium addition. Addition of 0.2%Al and 0.005%Mg was added together in the furnace to form spinel. Recovery rates were were considered to be 100 and 30%, respectively. The steel were poured at approximatly 1500°C. A schematic of the full melting sequence is shown in Figure 1.

Samples were taken at different steps in the melting process to understand the inclusion development during the process, in Figure 1. The samples were taken with quartz tubes sealed under vacuum to avoid reaction with atmosphere during sampling.

The samples solidify within a few seconds and this assures a good representation of the inclusion population present in the liquid as a function of addition. Inclusion analysis was performed on polished cross sections of samples taken from the melt and considering at least 2000 inclusions on each sample.

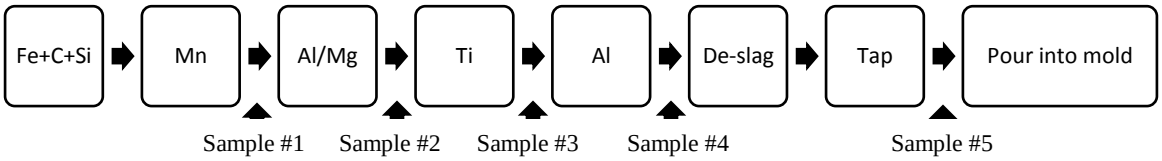

Figure 1. Melting sequence for steels with grain refining additions, showing the sampling moments during the melting and casting.

Table 1. Additional information on the melting procedure.

	Steel A	Steel B	Steel C
Time from Mg/Al to pour (min)	-	7	22
Tapping Temperature (°C)	1525	1515	1510

The mold had a cylindrical shape with a chill plate at the bottom for directional solidification, shown in Figure 2. Samples for composition and inclusion analysis were taken from the region next to the chill plate. Analysis of the macrostructure was done from the longitudinal cross section of the casting and etching was done to a polished face. Further details can be seen on a previously published paper.[10] The composition of the results steels was analyzed utilizingby optical emission spectroscopy (OES) and by a combustion analyzer (LECO analyzer) from samples taken from ½" from the chill plate.

Samples for inclusion analysis and optical microscopy were prepared by using standard metallographic techniques. A 10% Nital solution was used as an etchant for the microstructural evaluation. Macro etching was accomplished with a solution of 50%vol. HCl, 25%vol. HNO_3 and 25%vol. H_2O as listed for high alloyed steels in the ASTM E340-15, for 30-300s.

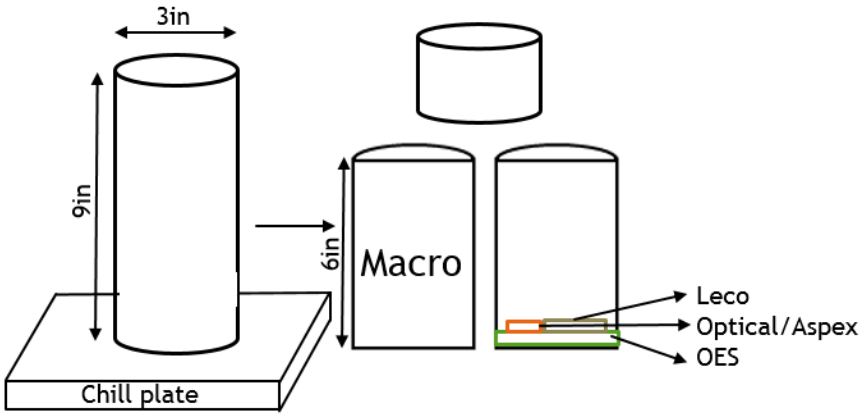

Figure 2. Steels were cast into a 3" diameter cylinder mold on top of a low-carbon steel chill plate and with 1" of hot topping.

The grain sizes were measured with aid of the image processing software, ImageJ. The average area of grains in the equiaxed region was measured and converted to an average grain size using the ASTM E112-13. The inclusions were analyzed from unetched polished samples using an ASPEX 1020 PICA automated scanning electron microscope with Automatic Feature Analysis, AFA, a backscattered electron detector, and an energy dispersive X-ray spectroscopy detector. Inclusions were separated according to their composition range into different classes.

The inclusion population was classified according to composition determined with SEM-EDS. The Fe content was not quantified in any inclusions because Fe-based inclusions are not expected, except in sample #1. Due to the high manganese content of the matrix (~30%), the manganese background content is high in several inclusions that do not contain manganese. Mn-based inclusions were identified by presence of sulfur and oxygen along with strong Mn signals, over 30%, and absence or other elements. The inclusions were divided in groups to simplify the classification and the analysis. Inclusions were divided in eight groups: AlN, Al_2O_3, MnS, Mn-Si-O, Ti-based, Spinel, Spinel-Ti, AlN-MnS. Ti-based inclusion were any inclusions with over 5%Ti, and Spinel inclusions were identified by presence of Mg and Al.

For better comparability of the inclusion populations, a methodology suggested by Van Ande et al. was used to represent inclusion size distribution.[13] This methodology uses the concept of Population Density Factor (PDF) to represent the number density of inclusion at specific size ranges. The bin sizes start from the largest non-metallic inclusion recorded in the sample and each size below this is reduced by a factor of $10^{-0.1}$. To convert the inclusion per unit area (#/mm^2) to the PDF, each bin size is divided by the bin size in order to normalize the data, since larger bin sizes have higher chance of inclusions being within that range. The final value called PDF has units of #/mm^3, it is however a representation of the 2D inclusion population. This method allows for a correlation between the type of inclusion population and the mechanism controlling it for different moments in the melting process, such nucleation, growth, breakage, agglomeration and removal of inclusions.

3. RESULTS

The compositions of the respective steels are shown in Table 2. The results show that the nominal composition of all the steels was close to the target composition of *Fe*-30*Mn*-5.6*Al*-1.5*C*-1*Si*. A small amount of Ti, 0.01%Ti, was measured in the base steel A as a results of the induction iron used in the charge. Steels B and C had additions of titanium of 0.30 and 0.46%Ti, respectively. The amount of oxygen, nitrogen and sulfur in the steels was similar. The total oxygen content was particularly low, aroung 5-6 ppm and this suggests that steel was relatively free of oxides.

Table 2.Composition in wt.% and (ppm) determined with OES and LECO* combustion analysis.

Steel	**Mn**	**Al**	**C***	**Si**	**Ti**	**Cr**	**Ni**	**O***	**N***	**S***
A	27.7	5.11	1.47	1.33	0.01	0.03	0.01	(6)	(66)	(45)
B	29.4	5.71	1.39	0.97	0.30	0.04	0.01	(5)	(68)	(52)
C	30.0	5.31	1.52	1.05	0.46	0.10	0.01	(6)	(60)	(48)

3.1. MICROSTRUCTURE CHARACTERIZATION

The as-cast microstructure of different steels is shown in Figure 3. All steels were observed to have a fully austenitic matrix without the presence of any ferrite. As shown in Figure 3(a), some precipitation that was most consistent with lamellar κ-carbide was noted on grain boundaries. The base steel A is shown to have a much lower inclusion density than steels with added titanium, as shown in Figure 3(a). The inclusions in steel A

were optically consistent with previous observations of AlN and MnS. The inclusions formed by the titanium addition appear to be larger in size than the original inclusion population of the base alloy, with some as large as 10 µm, as shown in Figures 3(b) and (c). The inclusions in steels B and C with titanium additions are observed to be cubic and in most cases exhibited an inhomogeneous contrast that may indicate regions of different chemical composition.

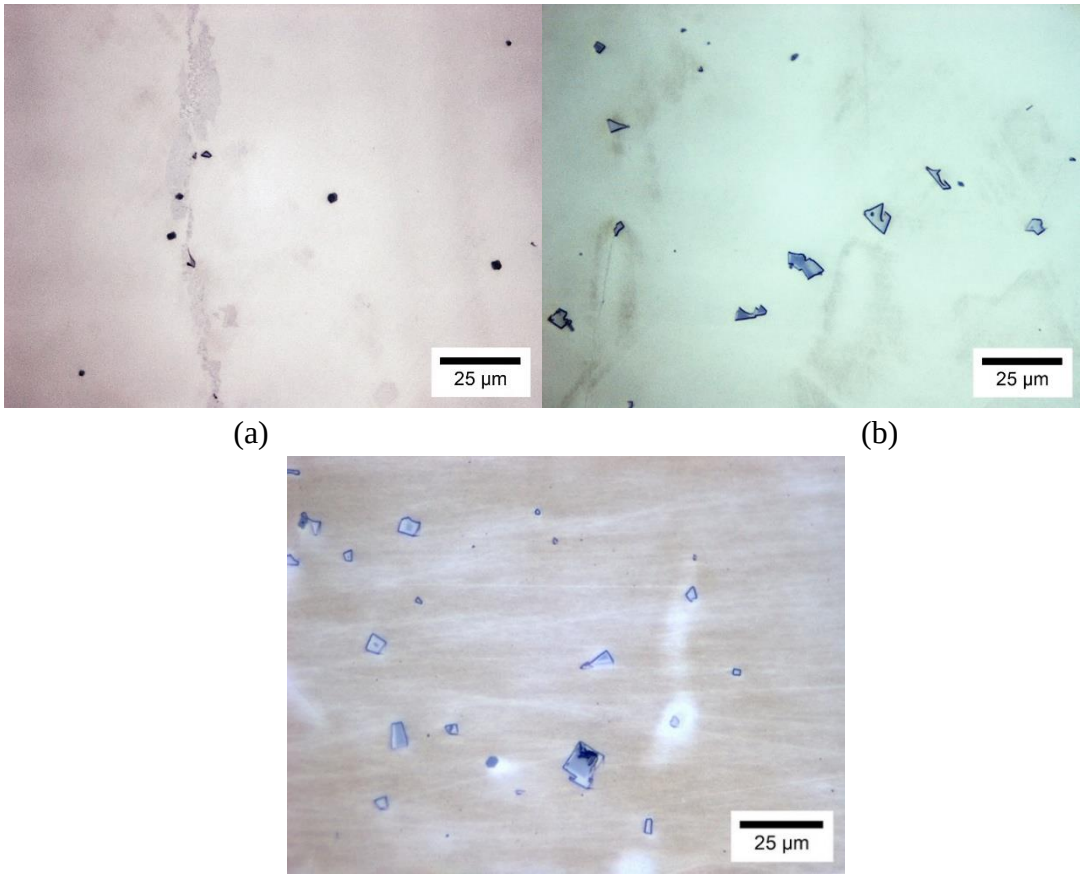

(a) (b)

(c)

Figure 3. Optical micrographs of the as-cast microstructure of (a) steel A without Ti addition, (b) steel B with 0.30%Ti, and (c) steel C with 0.46%Ti addition. (a) Inclusions in the unmodified steel were consistent with previous observations of AlN and MnS. (b and c) Inclusions in the steels with Ti additions are observed to be cubic and display a dual contrast.

The inclusion population in Figure 4 was determined utilizing an automated SEM-EDS and shows the difference in the inclusion populations of the different steels. The majority of the inclusions in the base steel were classified as AlN, MnS, and complex AlN-MnS, as previously observed for similar steels.[14,15] In steel B and C, MnS inclusions were observed, however, AlN and AlN-MnS was not. A large number of Ti-based inclusions formed in steel C, with almost 1000 inclusions/mm^2. The average composition of the inclusion population in each steel shows a shift in the type of the inclusions, as shown in Table 3. The average composition of inclusions for steels with Ti additions was over 70%Ti. In contrast, greater than 95% of the inclusions in the base steel were composed of Mn, Al, N, and S.

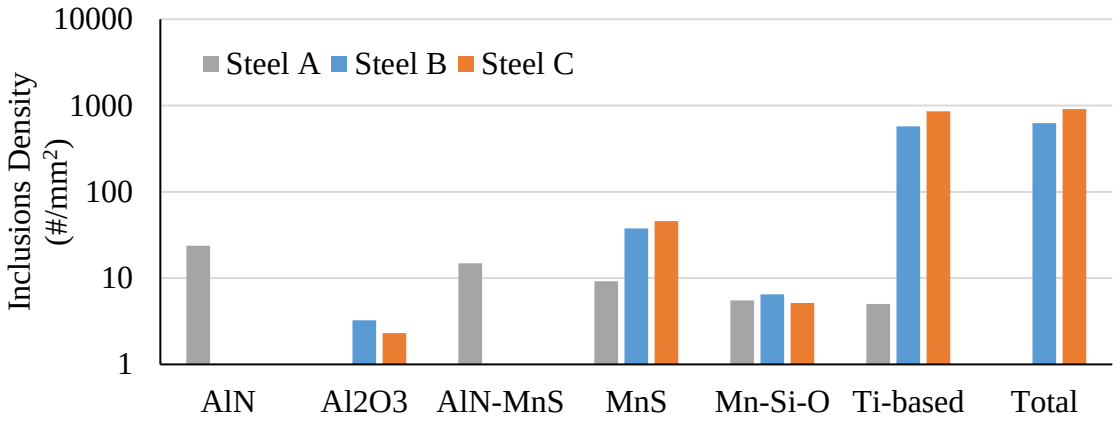

Figure 4. Inclusion number density of the different steels classified by type.

Table 3. Average composition of non-metallic inclusions.

	Mn	Al	Mg	Ti	O	N	S	Si	C
Steel A	**33.3**	**46.6**	0.1	0.0	-	**15.9**	**3.6**	3.6	-
Steel B	11.9	1.2	0.0	**74.0**	0.1	**12.5**	0.2	0.0	-
Steel C	12.3	0.6	0.0	**78.0**	0.6	**8.5**	0.1	0.0	-

The average compositions of inclusions in the castings show the absence of Mg-based inclusions. Analysis showed that not a single inclusion in the casting was classified as an Mg-based inclusion as shown in Figure 4. The rule file used classified any inclusion with over 5%Mg in the composition as Mg-based, or spinel. Table 1 shows that the variation in pouring time after inoculation varied from 7 to 22 min for steels B and C, respectively. Thus, floatation and removal of any Mg-based inclusions may have occurred prior to solidification. Inclusion evolution as a function of melt addition was subsequently analyzed with the goal of gaining a clearer understanding of the inclusion formation at each step in the melt practice as shown in Figure 1. The stability of different inclusions under thermodynamic equilibrium conditions was modeled using FactSage at each step in the melt practice as shown in Figure 5. Models predict initial formation of Mn-Si-O and then MgO + Spinel with subsequent addition of Mg and Al. After the addition of titanium to the furnace, the inclusion population is predicted to be primarily Ti(C,N). Addition of titanium leads to intense formation Ti(C,N) in step #3 well before solidification. The final addition of Al in step #4 initially de-stabilizes the spinel that reforms as temperature decreases. At this point, the Ti(C,N) might have precipitated all around the spinel and covered it to avoid dissolution $MgAl_2O_4$. The manganese sulfide was predicted to precipitate only at the end of solidification.

To try to understand why there are no Mg-based inclusions present in the casting, the development of the inclusions was analyzed by using the samples taken during melting of steel C, as referenced in Figure 1. In sample #1, the additions to the furnace only contained Fe-C-Si-Mn and the inclusion population was composed of Fe and Mn oxi-sulfides and manganese silicates.

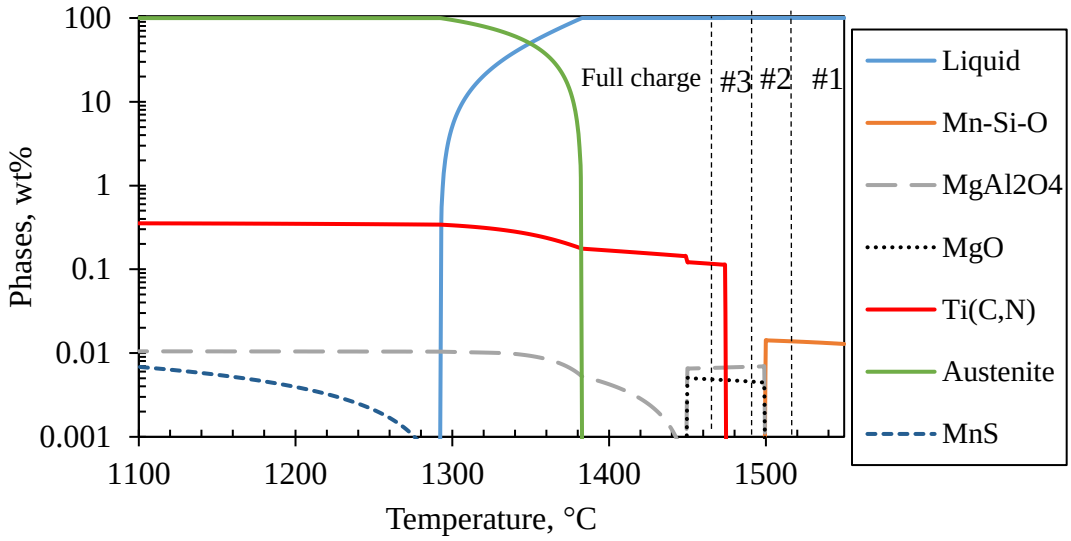

Figure 5. Equilibrium modeling of inclusion formation for the different sequence of melt additions, #1, #2, and #3 as referenced in Figure 1.

The inclusions in sample #2 that formed after the addition of Al and Mg, are shown in Figure 6 in the form of a joint ternary phase diagram and are represented by the three elements with the highest concentration in each of the inclusions. Inclusions above 2 µm were generally manganese silicates that may have nucleated early in the melting process and had time to coalesce and grow. The newly nucleated Mg-based inclusions are represented by the inclusions in ternaries Mn-Mg-O and Mn-Al-O, depending on which element was present in larger amount. This shows that Spinel inclusions do indeed form, but they were often coprecipitated with MnS as shown in Figure 6. The density of Mg-based inclusions, which included $MgAl_2O_4$ and MgO, was around 50 inclusions/mm^2. After addition of ferrotitanium to the furnace, inclusions in sample #3 were analyzed and the results are reported in Figure 7. A high density of Ti(C,N) inclusions were observed.

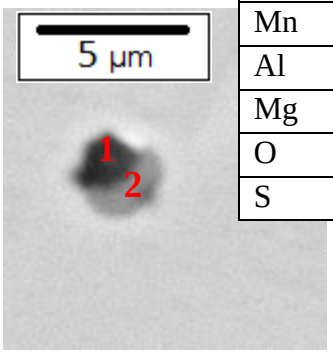

#2	1	2
Mn	39.1	67.5
Al	26.5	-
Mg	20.2	11.2
O	7.5	-
S	5.8	18.0

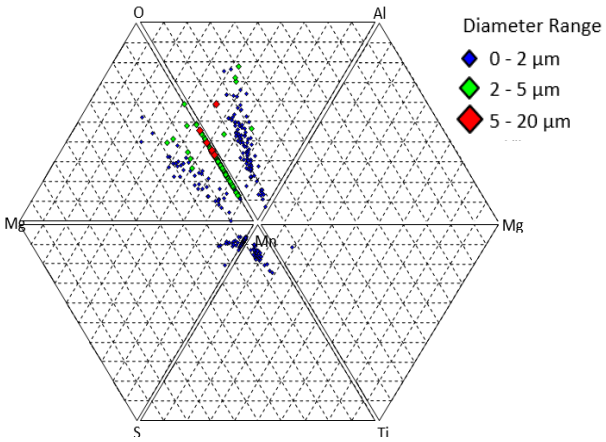

Figure 6. Inclusion population of sample #2 taken after addition of Al/Mg for the formation of $MgAl_2O_4$. A backscattered electron image shows EDS point analysis in two different parts of a complex inclusion composed of $MgAl_2O_4$-MnS.

Ti-based inclusions with Mg contents above 5% were also recorded and this indicates that precipitation of Ti(C,N) on spinel occurred and remained in the liquid up to this point. The area density of Ti(C,N) inclusions without Mg was over 240 times larger, so only a very small fraction of Ti(C,N) may have actually nucleated from spinel inclusions or the Ti(C,N) is obscuring them. Addition of Al, did not greatly modify the inclusion population. The inclusion analysis after Al addition in sample #4 is shown in Figure 8. Addition of aluminum at this point leads to formation of some Al_2O_3 inclusions and some inclusions in the Mn-Ti-Al ternary which are most likely coprecipitation of AlN or Al_2O_3 onto the previously present Ti(C,N). At this moment only 20 inclusions/mm^2 of Mg-based inclusions were observed, a decrease of 60% in a time span of 4min.

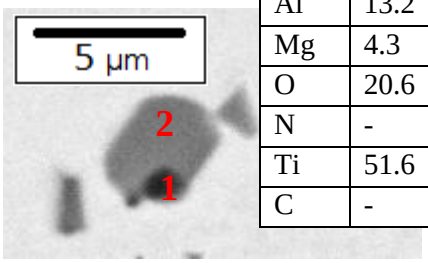

#3	1	2
Mn	10.2	6.2
Al	13.2	2.5
Mg	4.3	-
O	20.6	1.1
N	-	10.1
Ti	51.6	77.6
C	-	1.9

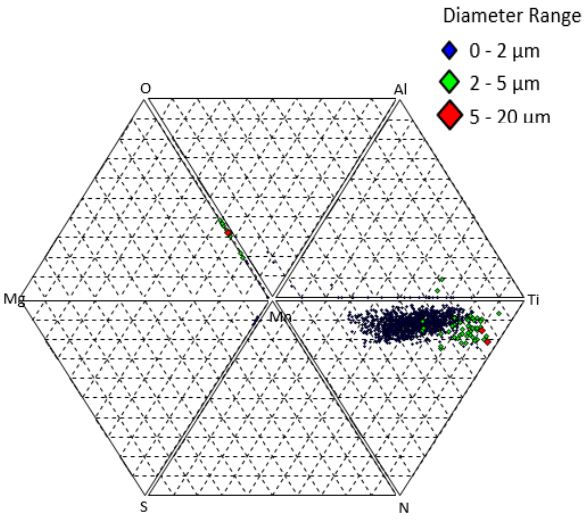

Figure 7. Inclusion population of sample #3 taken after addition of FeTi, with a backscattered electron image showing EDS point analysis in two different parts of a complex inclusion composed of $MgAl_2O_4$-Ti(C,N).

The inclusion population in the castings in Figure 4 shows no spinel inclusions because no inclusions with over 5%Mg were recorded in any of the steel castings. At first it was considered that Mg-based inclusions had floated out of the casting and were not present. However, the automated feature analysis used for measuring composition and classifying the inclusions uses an average composition of the inclusions and a closer look at the inclusions showed that spinel inclusions were still present in the interior of Ti(C,N) inclusions within the casting. The average size of Ti(C,N) was larger than that of spinel inclusions. The Figure 9 shows a $MgAl_2O_4$-Ti(C,N) cluster of inclusions found in the casting near a grain boundary. The average inclusion composition had less than the minimum threshold for elemental quantification of Mg and was classified as Ti-based.

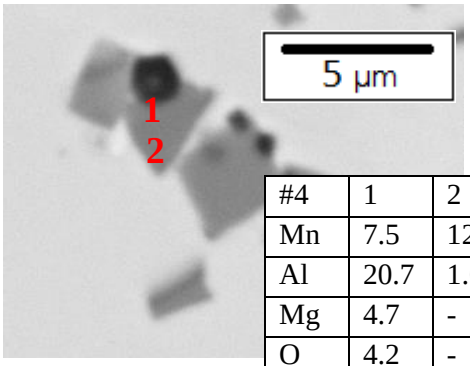

#4	1	2
Mn	7.5	12.3
Al	20.7	1.6
Mg	4.7	-
O	4.2	-
N	29.2	10.9
Ti	32.6	73.0
C	-	2.2

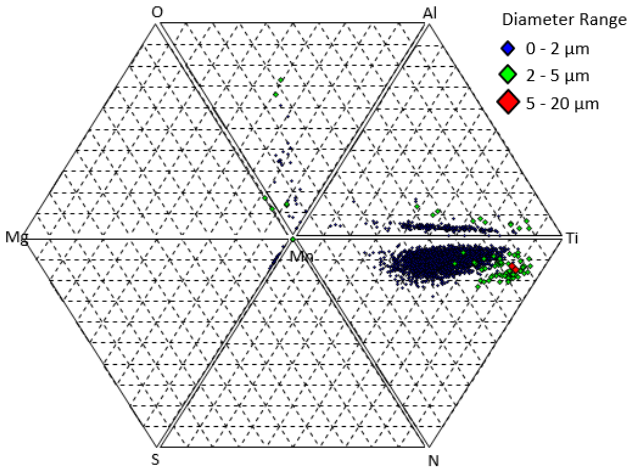

Figure 8. Inclusion population of sample #4 taken after addition of bulk aluminum, with a backscattered electron image showing EDS point analysis in two different parts of a complex inclusion composed of $MgAl_2O_4$-AlN-Ti(C,N).

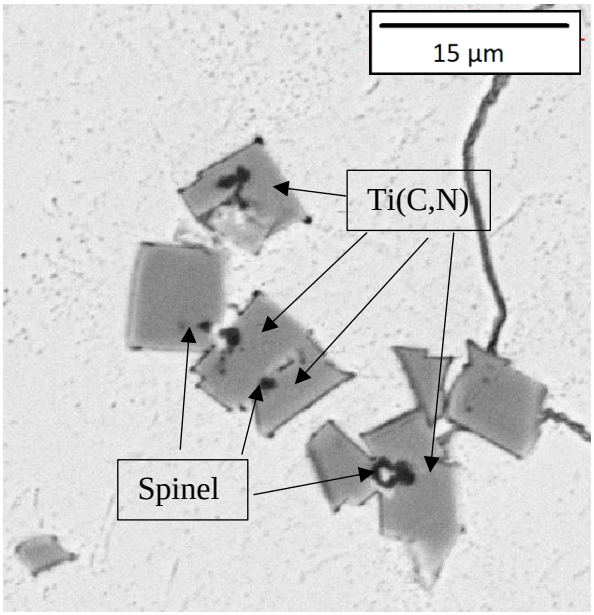

Figure 9. A backscattered electron image of a cluster of $MgAl_2O_4$-Ti(C,N) inclusions near a grain boundary in steel B. The sample was previously etched with 10%Nital, hence the delineated grain boundary.

The inclusion size distribution can be used to evaluate what kind of mechanisms are controlling the inclusion population. The population density function is shown in Figure 10. The initial inclusion population in sample #1 shows an aged population above 1 μm in size and this is identified by the approximately linear shape of the curve. Inclusion sizes below 1 μm present a quadratic shape which indicates fresh inclusion nucleation. With the addition of Mg in sample #2, not much different is shown in the overall shape of the distribution. The inclusions above 4 μm appear to have been removed from the liquid.

Addition of FeTi completely modifies the inclusion population as shown in Figure 10. A large density of inclusions appears that are 0.2-2 μm in size. A second inclusion population, derived from previously nucleated inclusions is shown for with a size range of 2- 5 μm. Inclusion analysis showed that these are Al_2O_3 and Mn-Si-O inclusions. After addition Al to the ladle in sample #4 no significant changes occurred in the population distribution. Sample #5 was taken from the ladle 17min after addition of FeTi. Only the quadratic population is present in Sample #5 and this is similar to inclusions observed after FeTi addition. These results show that very little growth or coalescence of inclusions is occurring and inclusion removal may be very slow.

The macrostructure of the steel was not changed by the addition of titanium and consequent change in the inclusion population. The length of the columnar zone remained unchanged in all three steel as shown in Figure 11. Steel C presented 24% smaller equiaxed grain size than the base steel, while steel B with a similar procedure, but lower Ti, presented an average equiaxed grain size 24% larger than the base steel.

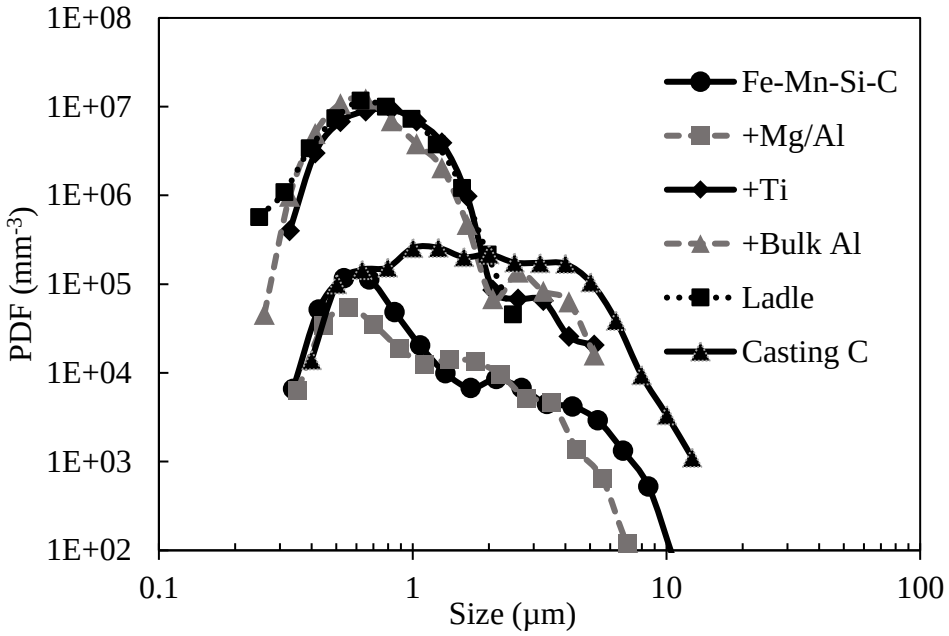

Figure 10. Population density function for a 2D analysis of the inclusion population at different moments of the melting and casting process.

4. DISCUSSION

The lack of growth, removal and clustering observed in the Ti-based inclusion population is a strong indication that the liquid is wetting the inclusion surface very well. It is suggested by literature that clustering of inclusions occurs by a mechanism of cavity bridge agglomeration that is facilitated by non-wetting condition between the solid particle and the liquid steel. The removal of inclusions is also facilitated by a non-wetting condition, especially during inert gas stirring (bubbling processes).[16,17] According to Young's equation, a low interfacial energy between the substrate and the liquid may create non-wetting conditions between the nucleating solid and the substrate which would be a barrier for heterogeneous nucleation. The Young's equation is shown in Eq. 1:

$$\frac{\gamma_{nL}-\gamma_{nS}}{\gamma_{LS}} = \cos\theta \qquad (1)$$

where γ_{LS} is the interfacial energy between the liquid and nucleating solid, γ_{nL} is the interfacial energy between the substrate and liquid, and γ_{nS} is the interfacial energy between the and substrate the nucleating solid. When γ_{nL} is much smaller than γ_{nS} there is an increase in the wetting angle, θ. The increase in θ indicates less wettability.

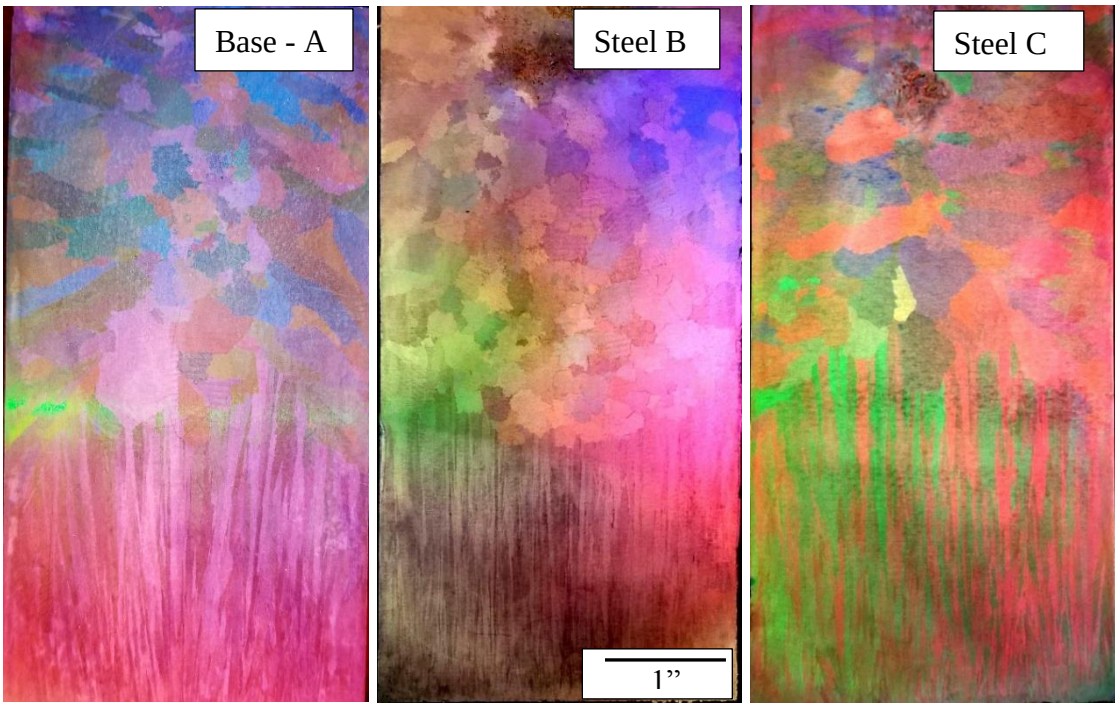

Figure 11. Macroetched structure of base steel (steel A), and steels with added Mg/Ti (steels B and C).

Inclusion clustering was evaluated using a clustering factor (C), that was calculated from the nearest neighbor distance (NND) as explained in literature.[18] A

clustering factor of 1 represents a completely random distribution. A clustering factor greater than one represents clustering and values below one indicate ordering.

The Figure 12 shows the clustering factor different steels and the presence of a high density of TiN/TiC. For a stainless steel UNS S31254 (SS) that had in-situ formation of TiN with and without coprecipitation on $MgAl_2O_4$, the clustering factor was reported to be 1.53 without coprecipitation which indicates clustering of inclusions.[18] With a modified procedure to form TiN after the formation of $MgAl_2O_4$ the inclusion population was close to completely random with clustering factor of 1.1. This indicates that without spinel formation, clustering of TiN occurs in stainless steels. In the current study, after the addition of titanium to the steel, the clustering factor varied from 0.8-1.2 showing a random distribution, even though the majority of Ti(C,N) inclusions did not nucleate from $MgAl_2O_4$ inclusions. In another study of FeMnAl steels using a TiN master alloy, the clustering factor was between 1.3 and 1.1.[10] In this case, there was strong evidence of dissolution and re-precipitation of Ti(C,N).

In steels, the clustering of TiN has been explained by the precipitation of oxides on the surface of the TiN. The oxides adhere to the surface of TiN or act as a heterogenous nuclei for more than one inclusion, creating a cluster.[18] In a study of an austenitic UNS S31254 steel, clustering was reduced when TiN was coprecipitated on $MgAl_2O_4$ inclusions. That may occur because the Ti(C,N) are coating the oxide inclusions of the steel making it no longer available to act as bridges for clustering. The inclusion population shown in Figure 4 shows a very low number of oxide inclusions (<10 inclusions/mm^2) and this is typical of FeMnAl steels. A representative spinel

inclusion is shown in Figure 7, and is shown coated by a manganese sulfide. There was no evidence that this poisoned the nucleation of Ti(C,N) on spinel surface.

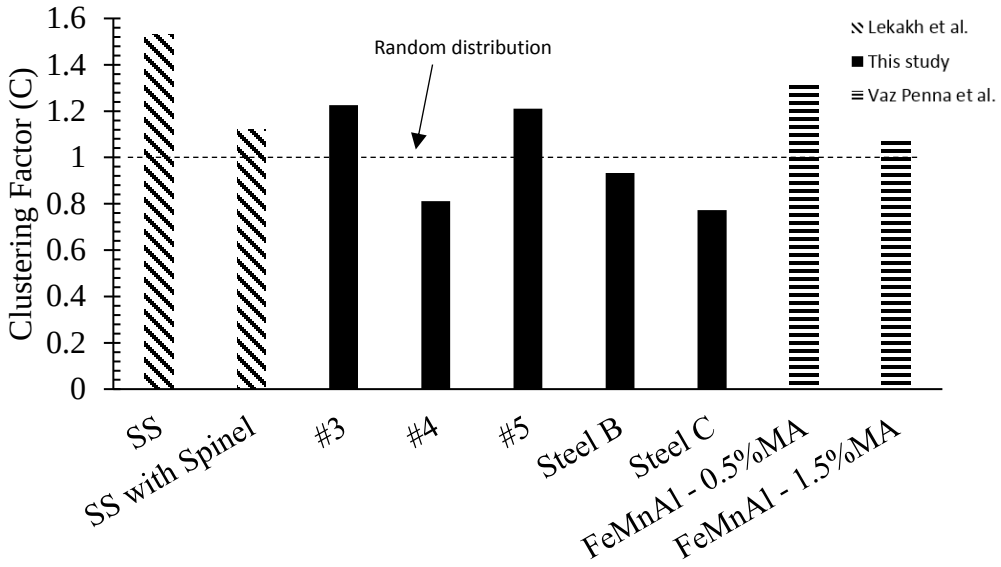

Figure 12. Clustering factor for TiN/TiC in different steels.[17,10]

The inclusion size distribution presented in linear bin sizes in Figure 13 shows that over 99% of the inclusion population present after the addition of Ti (#3), bulk Al (#4), and in the ladle (#5) has an average diameter below 2 μm. As mentioned in previous papers, literature suggested for Mg-based alloys that inclusions below 2μm do not act as heterogeneous nuclei. This was determined by measuring the average diameter of all the particles identified as active heterogeneous nucleation sites in the microstructure.[10,19] With the size distribution obtained in Figure 13, it was thus not likely that the inclusions would be able to act as a heterogeneous nucleation site. To have an appropriate size

distribution, coarsening of the inclusions in the liquid steel or clustering may be necessary.

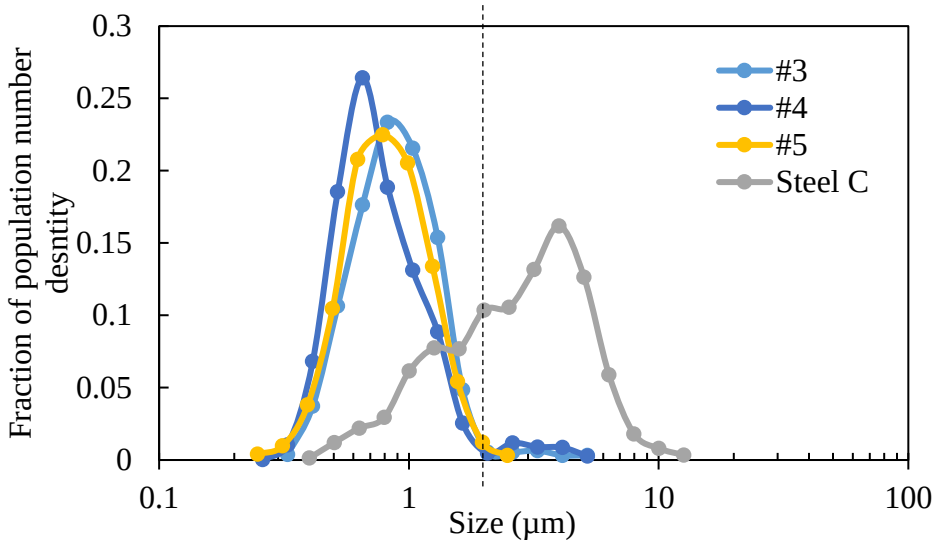

Figure 13. Inclusion size distribution of samples taken during melting and casting of steel C indicates that over 99% of inclusions were below 2 µm prior to pouring.

The analysis of the inclusion development and final inclusion population shows clearly the modification of the Al-based inclusion population due to the addition of titanium to the steel prior to the addition of bulk aluminum. In Figure 4, the base steel A had an area density of AlN and AlN-MnS close to 100 inclusions/mm^2 each. Steels B and C showed mainly TiN-based inclusions. This shows that at least for the titanium levels used, AlN does not form in these steels. The possibility of aluminum forming complex inclusions with the Ti-based inclusions was considered. However, the number of inclusions containing over 10% aluminum was negligible. The overall inclusion

chemistry for steels B and C, as given in Table 4, show a value of less than 1.1%Al and this is very low considering the matrix itself has 5.5%Al and some signal from the matrix is expected especially in smaller inclusions.

Table 4. Average composition in weight% of non-metallic inclusions in steels with added titanium.

	Mn	Ti	Al	Mg	Si	S	O	C	N
Steel B	11.4	71.2	1.1	0.0	0.0	0.2	0.1	3.7	12.0
Steel C	11.2	75.7	0.5	0.0	0.0	0.1	0.2	3.8	8.3

Studies of a Fe-30Mn-9Al-1C-1Si steel showed that the presence of AlN in as little as 50 inclusions/mm^2 can decrease the Charpy V-Notch toughness from 40 to 20J and dynamic fracture toughness from 400 to less than 50 kJ/m^2.[3,12] Unfortunately, it is also known that steels with titanium deoxidation instead of aluminum deoxidation show reduction in impact properties by almost 50% at similar inclusion densities.[15] In the current procedure, titanium oxides were not observed. During the moment of titanium addition to the melt is already high in Si, Mn, and C, and this maintains the dissolved oxygen at very low levels. The complete removal of AlN inclusions could be beneficial to the mechanical properties in these steels. Without the beneficial effect of grain refinement by Ti-based inclusions, it is necessary to optimize the titanium additions to decrease the area fraction of Ti-based inclusions.

5. CONCLUSION

Grain refinement in a as-cast Fe-30Mn-5.6Al-1.5C-1Si steel using a high density of Ti(C,N) was marginally effective at reducing the equiaxed grain size with a 0.3%Ti addition that co-precipitated on spinel surfaces.

Thermodynamic modeling and inclusion analysis of inclusion development in experimental steels showed that conditions were favorable for formation of $MgAl_2O_4$ inclusions which were observed in melt samples. In the conditions tested, the $MgAl_2O_4$ inclusions were also observed in the final casting with one or more Ti(C,N) inclusions that were found to precipitate around them. The addition of FeTi yielded a large number of Ti(C,N) in the final castings in quantities >500 inclusions/mm^2. However, only a 26% reduction in the equiaxed grain size was observed.

The population density functions of the overall inclusion populations showed a very difference in the Ti(C,N) population over time and this indicates the absence of growth, coalescence, and clustering between inclusions. This was possibly attributed to the low area density of oxides present in FeMnAl steel, which can act as bridges for inclusion clustering. Because of the lack of coarsening, the inclusions were in general less than 2 μm in diameter and might be too small to effectively act as substrates for heterogeneous nucleation of austenite from the melt.

One notable benefit of Ti addition was that Ti completely suppressed the formation of AlN. This may be beneficial to mechanical properties since AlN has been shown to have a strong detrimental effect on impact properties.

REFERENCES

1. Chen, S., Rana, R., Haldar, A., & Ray, R. K. (2017). Current state of Fe-Mn-Al-C low density steels. *Progress in Materials Science, 89,* 345-391. doi:10.1016/j.pmatsci.2017.05.002

2. Howell, R.A. & Van Aken, D.C.. (2009). A literature review of age hardening Fe-Mn-Al-C alloys. Iron and Steel Technology. 6. 193-212.

3. Bartlett, L.N., and Van Aken, D.C., "On the Effect of Aluminum and Carbon on the Dynamic Fracture Toughness of Fe-Mn-Al-C Steels," *AFS Transactions,* vol. 121(13-1343), (2013).

4. Thornton, P. A. (1971). The influence of nonmetallic inclusions on the mechanical properties of steel: A review. *Journal of Materials Science, 6*(4), 347-356. doi:10.1007/bf02403103

5. Stefanescu, D. M. (2015). *Science and Engineering of Casting Solidification*. Basingstoke, England: Springer.

6. Ohno, M., & Matsuura, K. (2008). Refinement of As-cast Austenite Microstructure in S45C Steel by Titanium Addition. *ISIJ International*, *48*(10), 1373-1379. doi:10.2355/isijinternational.48.1373

7. Lekakh, S. N., Ge, J., Richards, V., O'Malley, R., & TerBush, J. R. (2016). Optimization of Melt Treatment for Austenitic Steel Grain Refinement. *Metallurgical and Materials Transactions B, 48*(1), 406-419. doi:10.1007/s11663-016-0832-5

8. Arvola, D. A., Lekakh, S. N., O'Malley, R. J., & Bartlett, L. N. (2018). Two Inoculation Methods for Refining As-Cast Grain Structure in Austenitic 316L Steel. *International Journal of Metalcasting*. doi:10.1007/s40962-018-0260-1

9. Yang, L., Cheng, G., Li, S., Zhao, M., & Feng, G. (2015). Characteristics of MgAl2O4-TiN Complex Inclusion Precipitation and Growth during Solidification of GCr15SiMn in ESR Process. *ISIJ International*, *55*(8), 1693-1698. doi:10.2355/isijinternational.isijint-2015-170

10. Vaz Penna, R., Bartlett, L.N. (2019). "Progress in grain refinement of FeMnAl castings. Part 1. Fully austenitic FeMnAlC steel treated by complex TiN bearing master alloy". Manuscript in preparation.

11. Bramfitt, Bruce L. "The effect of carbide and nitride additions on the heterogeneous nucleation behavior of liquid iron." Metallurgical Transactions, vol. 1, no. 7, 1970, pp. 1987-1995.

12. Schulte, A. M., Lekakh, S. N., Van Aken, D. C., and Richards, V. L., "Phosphorus mitigation in cast lighweight Fe-Mn-Al-C steel," *Transactions of American Foundry Society*, vol.118, pp. 451 (2010).

13. Van Ende, M., Guo, M., Zinngrebe, E., Blanpain, B., & Jung, I. (2013). Evolution of Non-Metallic Inclusions in Secondary Steelmaking: Learning from Inclusion Size Distributions. *ISIJ International, 53*(11), 1974-1982. doi:10.2355/isijinternational.53.1974

14. Vaz Penna, R., Bartlett, L. N., & Constance, T. (2018). Understanding the Role of Inclusions on the Dynamic Fracture Toughness of High Strength Lightweight FeMnAl Steels. *International Journal of Metalcasting*. doi:10.1007/s40962-018-073-9

15. Bartlett, L., Dash, A., Van Aken, D., Richards, V., & Peaslee, K. (2013). Dynamic Fracture Toughness of High Strength Cast Steels. *International Journal of Metalcasting*, *7*(4), 17-33. doi:10.1007/bf03355561

16. Yin, H., Shibata, H., Emi, T., & Suzuki, M. (1997). Characteristics of Agglomeration of Various Inclusion Particles on Molten Steel Surface. *ISIJ International, 37*(10), 946-955. doi:10.2355/isijinternational.37.946

17. O'Malley, R. J. (2017). Inclusion Evolution and Removal in Ladle Refining. In *AISTech*. Retrieved from http://digital.library.aist.org/pages/PR-372-364.htm

18. Siafakas, D. *On deoxidation practice and grain size of austenitic manganese steel, MS T*hesis, Jonkoping, Sweden. Accessed 2017.

19. Qiu, D., & Zhang, M. (2009). Effect of active heterogeneous nucleation particles on the grain refining efficiency in an Mg–10wt.% Y cast alloy. Journal of Alloys and Compounds, 488(1), 260-264. doi:10.1016/j.jallcom.2009.08.100

SECTION

2. CONCLUSIONS

The engineering of inclusions for improvement of mechanical properties was used for mitigating the detrimental effects of pre-existing AlN inclusions and to refine the as-cast microstructure. Controlled additions of sulfur lead to the precipitation of soft MnS on the surface of hard and angular AlN inclusions. The large majority of the AlN was partially or completely coated with MnS, however, no improvement of the impact properties of the material was achieved. The Charpy V-notch toughness and dynamic fracture toughness were found to be related to the overall inclusion population area density and decreased with the increase in inclusion density for solution treated and quenched steels. In the aged condition toughness was much lower and indifferent to the inclusion population.

Studies aimed at developing a grain refining inoculant showed that additions of FeTi, FeTi+FeNb, and a TiN master alloy did not significantly modify the structure of Fe-30Mn-9Al-1C-Si steel with a primary solidification as δ-ferrite followed by formation of austenite through a peritectic reaction. A Fe-30Mn-5.6Al-1.5C-1Si steel with a single phase austenitic solidification also did not presented significant grain refinement by additions of FeTi, FeSiMg+FeTi, FeNb, FeSiCe, or by utilizing a TiN master alloy. Inclusions formed were identified as Ti(C,N), $MgAl_2O_4$+Ti(C,N), Nb(C,N), and Ce-oxisulfides, respectively. The Ce-based, Mg+Ti-based inclusions, however, did decrease the length of the columnar grains zone by approximately 50%.

APPENDIX

THE EFFECT OF Nb AND Ce ON REFINEMENT OF THE AS-CAST MICROSTRUCTURE IN FeMnAl STEELS

Rairu Vaz Penna, Laura N. Bartlett, Trevor Constance

Missouri University of Science and Technology
Materials Science & Engineering Dept.
1400 N Bishop, Rolla, MO, U.S.A., 65409

Keywords: high manganese steels, inoculation, nonmetallic inclusions

ABSTRACT

Grain refinement of the as-cast microstructure of FeMnAl steels is important for further development of the mechanical properties of the alloy. In this study several different grain refining additions were considered. These consisted of Nb, Ti, Ti+Nb, a TiN master alloy, Ce, and Mg+Ti that were considered based on previous results in the literature and calculations of lattice misfit between the inclusions and steels with either primary ferrite or primary austenite solidification. Inclusion analysis showed that desired inclusions were generally formed in a large number density of up to 1000 inclusions/mm^2 in some cases. However, in all cases there was not a large reduction in the equiaxed grain size, however, the length of columnar zone was decreased by addition of Ce to produce complex Ce-sulfides and Ce-oxides as well as Mg+Ti additions that produced a complex precipitation of Ti(C,N) on spinel inclusions.

1. INTRODUCTION

The FeMnAl steels are explored due to their high strength and high energy absorption properties. Production of high manganese steels by continuous casting route has several limitations and the only known commercial producer is in South Korea. Domestic steel producers are interested in determining a cost effective method of producing these steels, however, the high alloy content of these steels make them difficult to produce. This is because these alloys have very long-range solidification behavior, a large as-cast grain size and prolific solidification segregation that makes those steels susceptible to hot tearing during continuous casting. In addition, the high degree of segregation and large as-cast grain size produces a high degree of microporosity and a non-uniform response to subsequent heat treatment. Production by conventional casting methods is an option, but has diminished mechanical properties when compared to continuous castings due to increased segregation, larger grain size, and more porosity.

Grain refinement of the as-cast microstructure during conventional casting can be achieved by inoculation. The inoculation consists in addition of preformed particles or alloying elements to the melt to form these particles in-situ. These particles act as nucleation sites for austenite or ferrite (depending on the solidification path) and this greatly decreases the energy barrier for nucleation. The decrease in the energy barrier leads to a higher nucleation rate and the final grain size is decreased due to grain impingement.

The effectiveness of substrate as a grain refining agent depends on the interfacial energy with the liquid and nucleating solid, the thermodynamic stability in the melt, as

well as the size, morphology and spatial distribution. The interfacial energy is controlled by the chemical and physical properties of the nucleating agent itself, while other parameters can be controlled by melt processing. The interfacial energy is complicated to determine experimentally, however, the lattice misfit is often used as a reference for determining if a substrate is appropriate for grain refinement.[1-5] The planar disregistry model was suggested by Bramfitt to be a good indicator of heterogeneous nucleation potential and values below 6 to 12% are used as reference for good grain refiners.

Calculations of the lattice misfit for a variety of inclusions in relation to austenite and δ-ferrite are shown in the introduction section of this thesis on Tables 1.2 and 1.3 on pages 46-47. Based on those calculations and on experimental results from literature the addition of Nb for formation of NbC, Ce for formation of $AlCeO_3$, Ti for formation of Ti(C,N), and Mg for formation of $MgAl_2O_4$ were explored through experimental heats and their corresponding effects on the average equiaxed grain size and length of columnar grains zone were determined.

2. EXPERIMENTAL PROCEDURE

The grain refinement trials on as-cast steels during solidification were performed utilizing experimental heats produced in a 100 or 200lbs coreless induction furnace. High purity charge consisting of induction iron, ferrosilicon, electrolytic manganese, ferromolybdenum, 1020 aluminum, and graphite were charged in the furnace. The furnace and ladle used an MgO-based lining. The furnace atmosphere was controlled by

argon flow of 25scfm and covered by a blanket of alumina. The grain refining additions for the titanium added steels were either Ferrotitanium, a TiN containing master alloy, or ferromagnesium-silicon or a combination of these additions. The grain refining additions for the cerium-based heats consisted of a commercially available FeCeSi based ferroalloy. The steels with Nb additions were treated with ferroniobium.

Table 2.1 summarizes the steels discussed, including the addition of each steel, pouring temperature and the casting design used.

Table 2.1. Summary of steel grain refining additions and processing conditions for steels exhibiting single-phase austenitic solidification and primary ferrite solidification.

Steel	Addition	Pouring temp. (°C)	Casting Design	Solidification mode
1	BASE	1470	Y-block	ferrite → austenite
2	0.06%Ti	1419	Y-block	ferrite → austenite
3	0.12%Ti	<1420	Y-block	ferrite → austenite
4	0.12%Ti + 0.12%Nb	<1420	Y-block	ferrite → austenite
5	0.12%Ti + 0.48%Nb	<1420	Y-block	ferrite → austenite
6	Base	1502	Y-block	ferrite → austenite
7	0.5%MA	1496	Y-block	ferrite → austenite
8	BASE	Freezing	Cylinder + chill	ferrite → austenite
9	1%MA	Freezing	Cylinder + chill	ferrite → austenite
10	BASE	1534	Cylinder + chill	austenitic
12	0.08%Ce	1475	Cylinder + chill	austenitic
14	BASE	-	Cylinder + chill	austenitic
15	0.12%Nb	1507	Cylinder + chill	austenitic
16	0.12%Ce	1451	Cylinder + chill	austenitic
18	Spinel+Ti	1510	Cylinder	austenitic
19	Spinel+Ti	1515	Cylinder	austenitic
20	BASE	1450	Cylinder	austenitic

Most of the grain refining additions were added to the ladle prior to pouring. The one notable exception was for steel 7. During the processing of steel 7, the grain refining addition was in the form of a TiN-contaning mater alloy added into the furnace just prior to the tap. The steels were cast into no-bake sand molds that consisted of either modified Y-block castings shown in Figure 2.1(a) or cylindrical bar castings as shown in Figure 2.1.(b). Steels 1-7 were cast into the design on Figure 2.1(a) and steel 8-16 were cast in in the design shown in Figure 2.1(b). The design in Figure 2.1(a) was used to create a strong thermal gradient and directional solidification by adding a steel chill to the base plate in castings 8-16 to be closer to continuous casting conditions. In castings 18-20 the chill plate was not utilized to evaluate the effect of a shallow thermal gradient on heterogeneous nucleation and grain refinement.

The macrostructure was revealed by preparing the surface with 320# SiC abrasive paper and etching with a mixture of 50% HCl, 25% HNO_3, and 25% H_2O per volume, as per ASTM E320-15 for high alloy steels. The composition was determined with optical emission spectroscopy (OES) and by a LECO combustion analyzer for O/N and S/C.

The inclusion population was analyzed using an ASPEX PICA 1020 SEM-EDS system with Automated Feature Analysis, AFA, for identification of inclusions that were classified according to their composition. Grain size was measured from the macro-etched optical images by manual delineation of the grains present in the entire surface and measurement of the average area using ImageJ. Conversion from area to average diameter was done as per ASTM E112.

The results and discussion are separated according to the additions made into steels with a dual solidification, with Ce addition, with Nb addition, and with Ti addition and with or without directional solidification (chill plate).

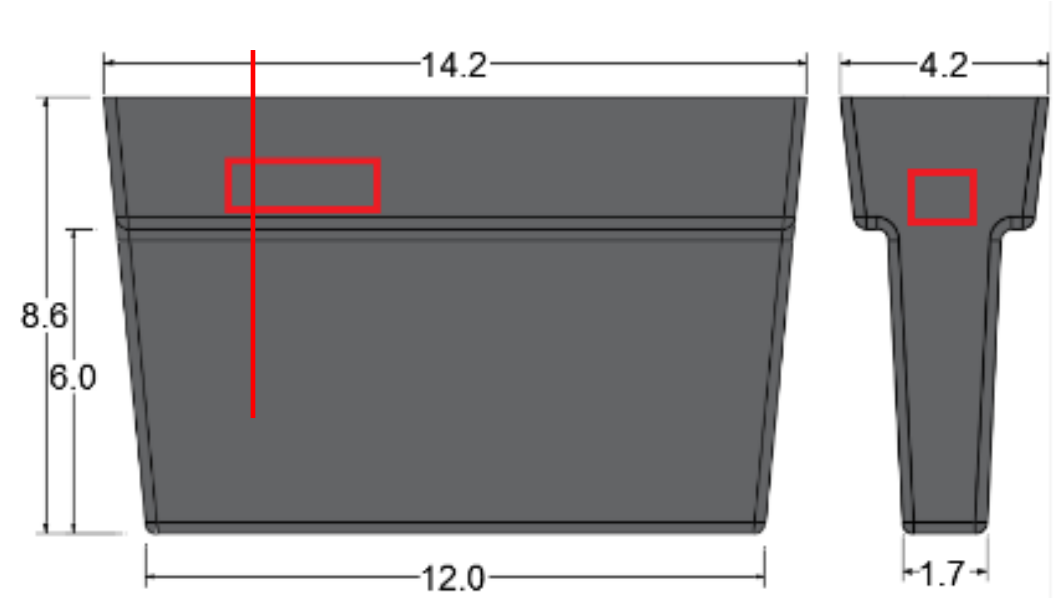

(a)

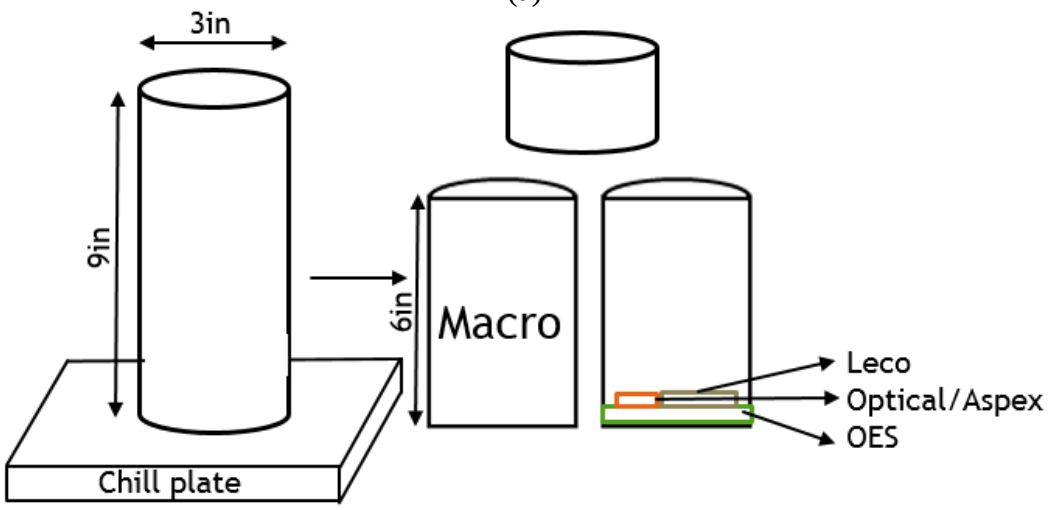

(b)

Figure 2.1. Casting design used for (a) steels 1-7 and (b) 8-16. The location of macro-etched regions is shown by the red line in (a) and marked on the longitudinal cross-section in (b).

Dual solidification steels presented a solidification that started with formation of δ-ferrite followed by a peritectic transformation in which the remaining liquid and ferrite was consumed by austenite. At room temperature the as-cast microstructure of most steels consisted of a fully austenitic matrix as shown in Figure 3.1 for steels 1, 3, and 5 with nominal composition of Fe-30Mn-8Al-1C-1Si-(0.5-0.6)Mo and with different additions of Ti and Nb for grain refinement. Steels 1-5 had 0.5-0.6%Mo. Molybdenum was not added in steels 6-9 in order to avoid the interaction between Mo and carbides forming in the liquid.

The steels with nominal composition of Fe-30Mn-5.6Al-1.5C-1Si had a fully austenitic solidification, with no formation of ferrite. The solidification sequence can determine the efficiency of the grain refining addition and this is discussed in detail in the introduction of this thesis in section 1.4.3. The steel with added FeNb was steel 15, steels 12 and 16 had addition of FeSiCe at different amounts, steels 18 and 19 had addition of FeSiMg and FeTi and used a design with no chill plate to decrease cooling rate. The steels 1, 6, 8, 10, 14, 20 were base heats with no additions.

3. RESULTS AND DISCUSSION

3.1. DUAL SOLIDIFICATION STEELS

The initial steels cast for studying grain refinement during solidification were cast with a nominal composition of Fe-30Mn-9Al-1C-1Si. Thee compositions are listed in Table 3.1. The as-cast microstructure presented in Figure 3.1 shows a dendritic structure, in steel 3 the dendrite cell sizes appear to be smaller than in the base steel 1. A look in

Table 2.1 shows that steel 3 was cast at a temperature at least 50°C lower than steel 1 which could also affect the secondary dendrite arm spacing and dendrite sizes. The microstructures of steels 6 and 7 are shown in Figure 3.2. As previously reported, steel 6 is a base alloy and steel 7 had the addition of 0.5wt.% of the TiN master alloy (MA), but it did not show much difference from steels 1-5.

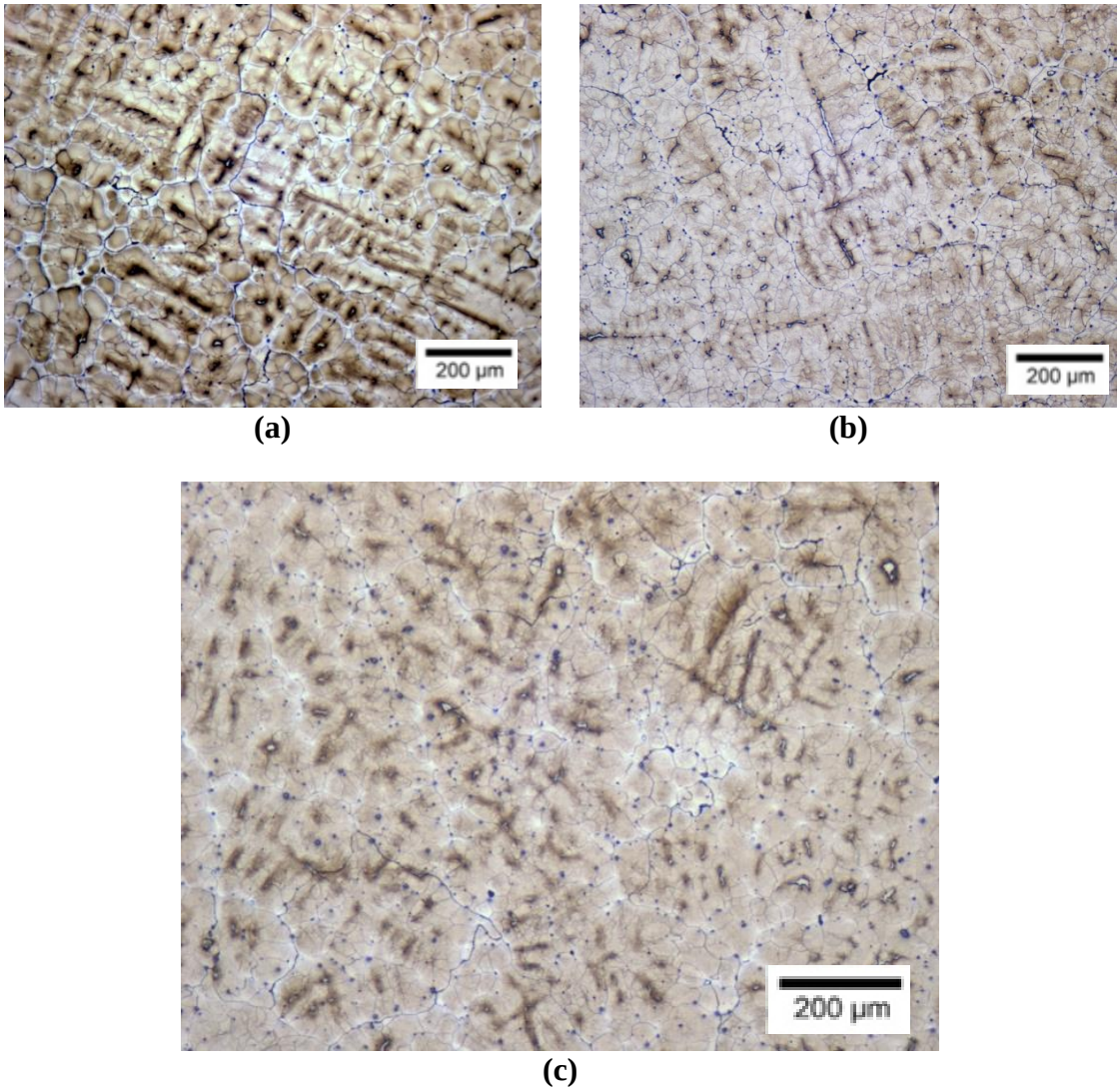

(a) **(b)**

(c)

Figure 3.1. Optical microstructure of steels (a) 1, (b) 3 added with Ti, and (c) 5 added with Ti+Nb showing a decrease in the size of the dendrites.

Table 3.1. Compositions of steels with dual solidification modes.

	Mn	Al	C	Si	Mo	Nb*	Ti	Total O (ppm)	N (ppm)	S (ppm)	Type
GR-1	30.3	7.9	1.07	1.11	0.63	-	0.02	7	20	87	Base
GR-2	30.2	8.0	1.02	1.08	0.57	0	0.05	12	2	57	Ti
GR-3	30.4	7.8	1.07	1.11	0.60	0	0.16	33	29	71	↑+Ti
GR-4	31.4	8.0	1.00	1.12	0.53	0.12*	0.16	10	16	70	↑+Nb
GR-5	30.7	8.4	1.01	1.12	0.53	0.61*	0.16	14	23	74	↑+Nb
GR-6	29.9	7.9	1.05	1.06	-	-	-	5	34	33	Base
GR-7	29.8	7.7	1.05	1.08	-	-	0.18	7	36	31	MA
GR-8	30.4	7.2	0.94	0.87	-	-	0.01	3	38	78	Base
GR-9	29.5	7.0	0.94	0.86	-	-	0.21	2	52	87	MA

*****Estimated from charge.

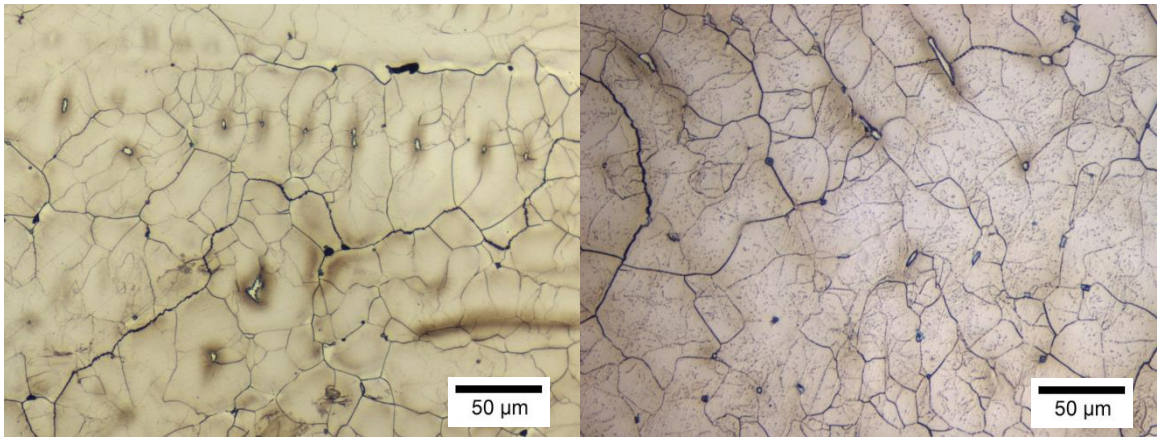

(a) (b)

Figure 3.2. Optical microstructure of steels (a) 6 and (b) 7 showing no signs of nucleation from the Ti(C,N) inclusions formed and small amounts of retained ferrite.

The average grain size of all steels were similar as shown in Figure 3.3. There was a decrease from 1.1mm to 0.8mm in average grain size from base steel 1 to steels 2-5, which seems to indicate a decrease in grain size of steel when added with Ti and Ti+Nb. However, base steel 6 had the same grain size as steel 2 added with Ti, steel 5 added with Ti+Nb, and steel 7 added with 0.5% MA.

The as-cast macrostructures of steels 1-7 are shown in Figure 3.4. There is no visible difference in the grain size between the base steels 1 and 6 and the steels added with Ti, Ti+Nb, and the TiN master alloy. Grains are in general small, and elongated perpendicular to the direction of heat extraction. A region of fine subgrains seems to be present within the elongated columnar grains.

The inclusion population in the base steel 1 was mostly composed of AlN and MnS as shown in Figure 3.5. Small amounts of Ti-based inclusions were present due to trace amounts of titanium in the charge. After the addition of Ti and Nb, a large number

of Ti-based inclusions formed. Since steels 1-5 had addition of 0.5%Mo, the phase formed was a (Ti,Nb,Mo)(C,N). The automated SEM-EDS uses a difference in Z-contrast to identify inclusions. The presence of Mo in the carbonitrides made them the same contrast as the matrix and thresholding for automatic classification was not possible. Table 3.2 shows the average composition of 32 Ti-based inclusions in steel 3 in weight percent. The amount of Mo adds up to over 14%, due to this it was decided to remove Mo from the composition, for formation of Ti(C,N) and Nb(C,N) without any element in solution and also to make it possible to use the automated SEM-EDS for quantification of the population.

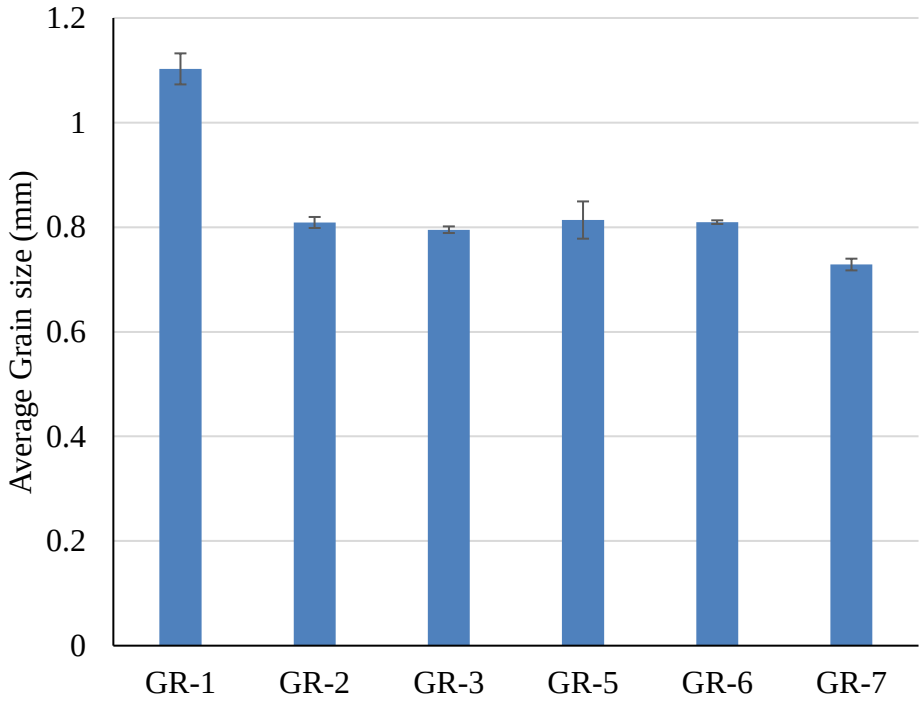

Figure 3.3 As-cast average grain size of steels.

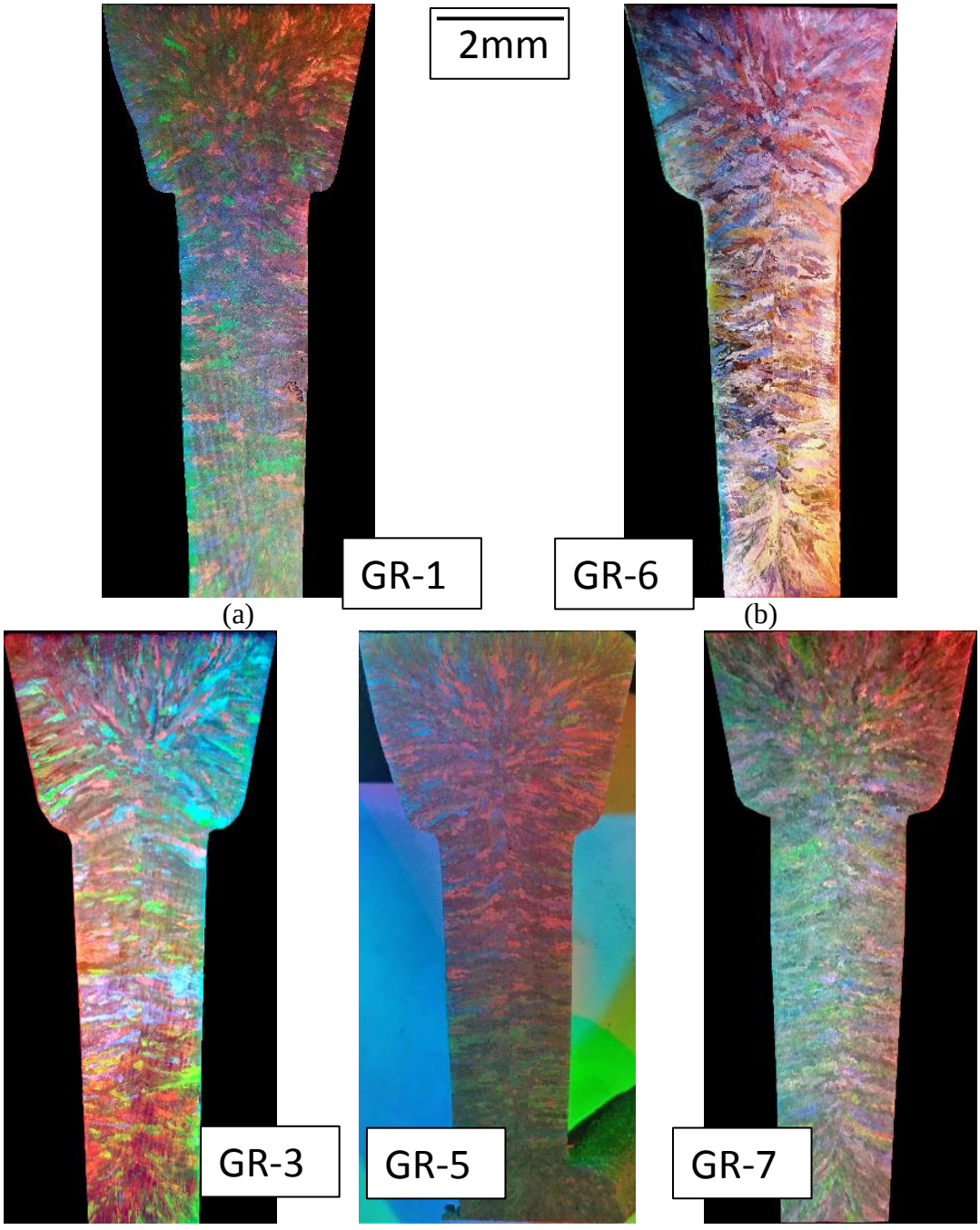

Figure 3.4 As-cast macrostructure of steels base steels (a) 1 and (b) 6, was very similar to steels (c) 3 added with Ti, (d) 5 added with Ti+Nb, and (e) 7 added with 0.5% MA.

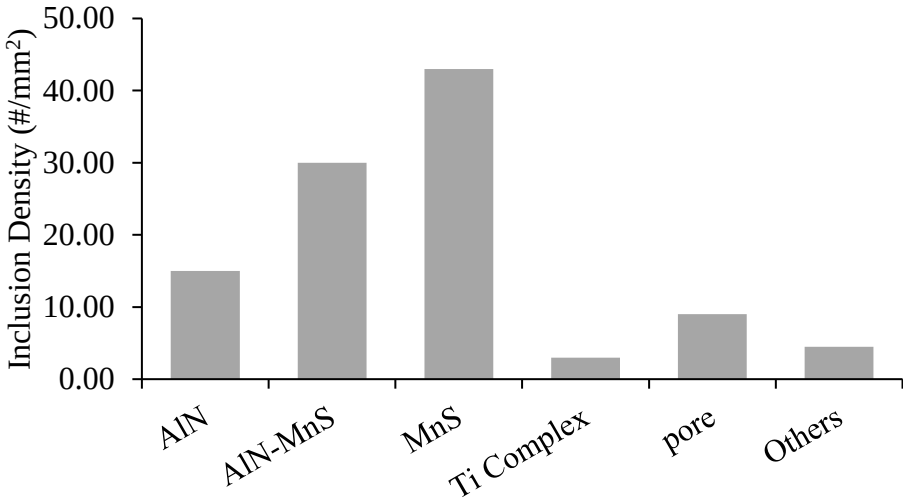

Figure 3.5. Inclusion densities by type in base steel 1.

Table 3.2. Average composition of Ti-based inclusions in wt%.

Fe	Mn	Al	S	N	C	Ti	Mo
30.1	21.9	3.3	1.1	1.9	2.3	24.7	14.6

Without considering Mo in the composition, the inclusions were mostly Ti-C-N with presence of MnS and AlN that co-precipitated, as shown in Figure 3.6. The Ti-based inclusions had a faceted morphology and were evenly distributed in the matrix.

Steels 6 and 7 were a base steel and a steel with added 0.5wt% TiN Master Alloy (MA), respectively. The inclusion population was mostly Ti(C,N) with a Ti-based inclusion density of 472 inclusions/mm^2, as shown in Figure 3.7. Despite the large density of Ti(C,N), Figure 3.3 showed that no quantitative refinement was obtained.

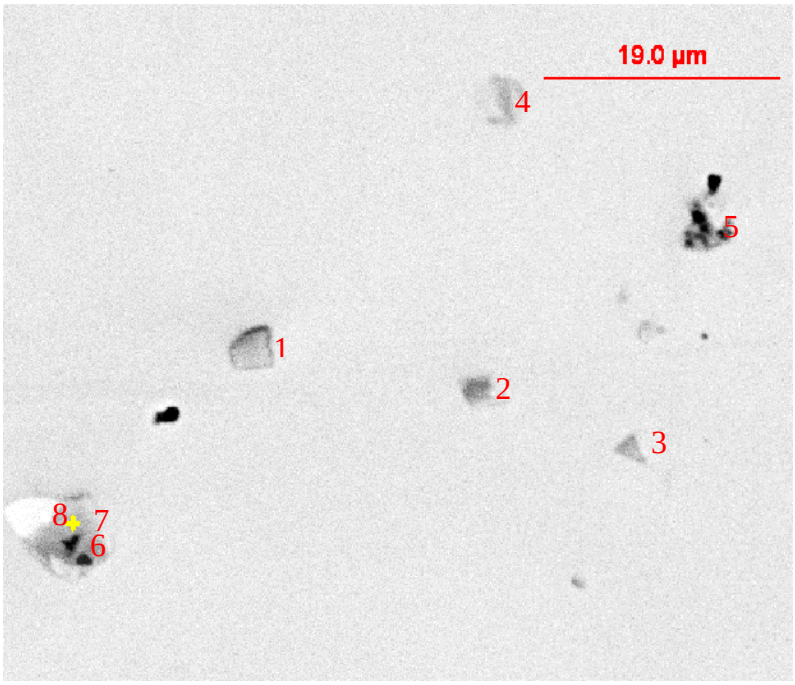

	Fe	Mn	Al	Ti	C	N	S	**Classification**
1	6.7	5.8	-	54.4	4.1	13.3	9.0	Ti(C,N)
2	23.7	14.2	2.2	45.3	4.9	-	5.8	TiC-MnS
3	6.6	5.7	1.0	66.6	5.3	-	9.0	TiC
4	62.0	27.2	7.2	-	1.8	-	-	porosity
5	23.6	16.4	8.3	36.3	3.1	3.7	4.8	Ti(C,N)-MnS-AlN
6	3.5	9.0	5.9	48.8	-	20.6	8.1	TiN-MnS
7	2.4	3.0	-	67.9	4.9	5.4	10.0	Ti(C,N)
8	43.1	45.3	2.2	-	1.5	-	2.3	Segregation

Figure 3.6. Example of inclusions present in steel 3 with Ti addition. Molybdenum content was not quantified on these inclusions.

For steels 8 and 9, the casting design was changed to a cylinder as shown in Figure 2.1(b). Steel 8 as the base steel and steel 9 had the addition of 1% MA. Figure 3.8 shows that the microstructure of these steels were dendritic and directional as intended.

The macrostructure in Figure 3.9 shows a grain structure very similar to steels 1-7, the grains are in general elongated perpendicularly to the heat extraction direction. A fine columnar grain region is present closer to the chill plate, but a separation between it and equiaxed region is not easily determined. The average grain size shown in Figure 3.10, shows no quantitative refinement.

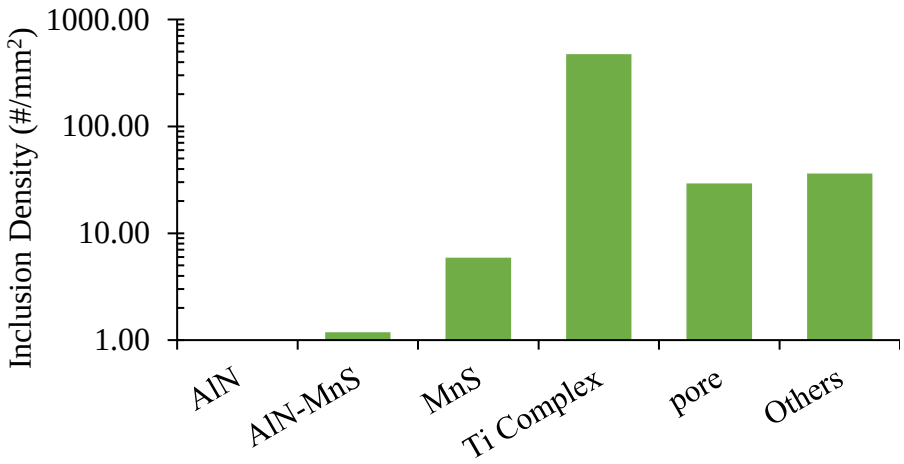

Figure 3.7. Inclusion population of steel 7 added with TiN master alloy.

All the trials with the steels with nominal composition Fe-30Mn-9Al-1C-1Si showed no grain refinement with addition of Ti, Nb or MA. The grain refinement depends on the interaction between the phase acting as a heterogeneous nuclei and the phase nucleating on it. A dual solidification mode can make grain refinement more difficult since there is a change in the nucleating phase during the solidification. Therefore for further tests, the nominal composition was changed to Fe-30Mn-5.6Al-1.5C-1Si as explained in detail in Paper II of this thesis on pages 87-89.

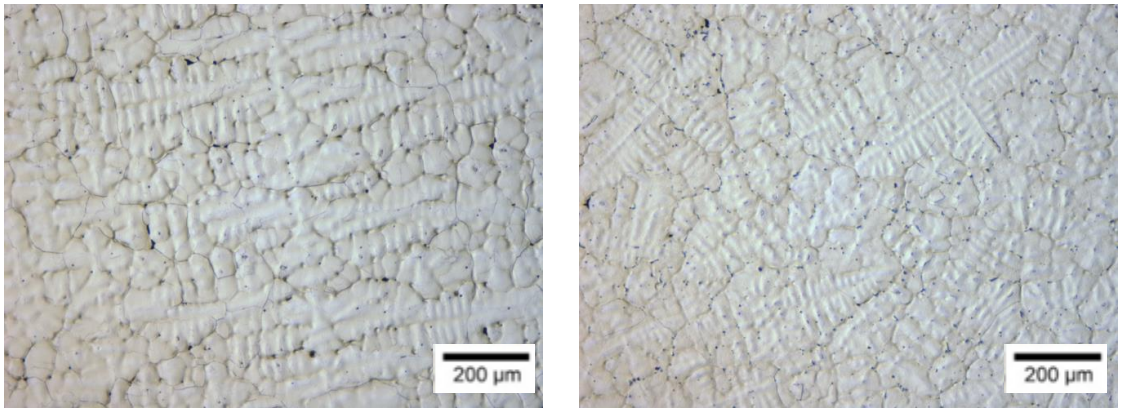

(a) **(b)**

Figure 3.8. The microstructure of steels and 8 and 9. In (a) is shown a view parallel to the heat extraction in steel 8 and in (b) is a view parallel to the heat extraction direction for steel 9.

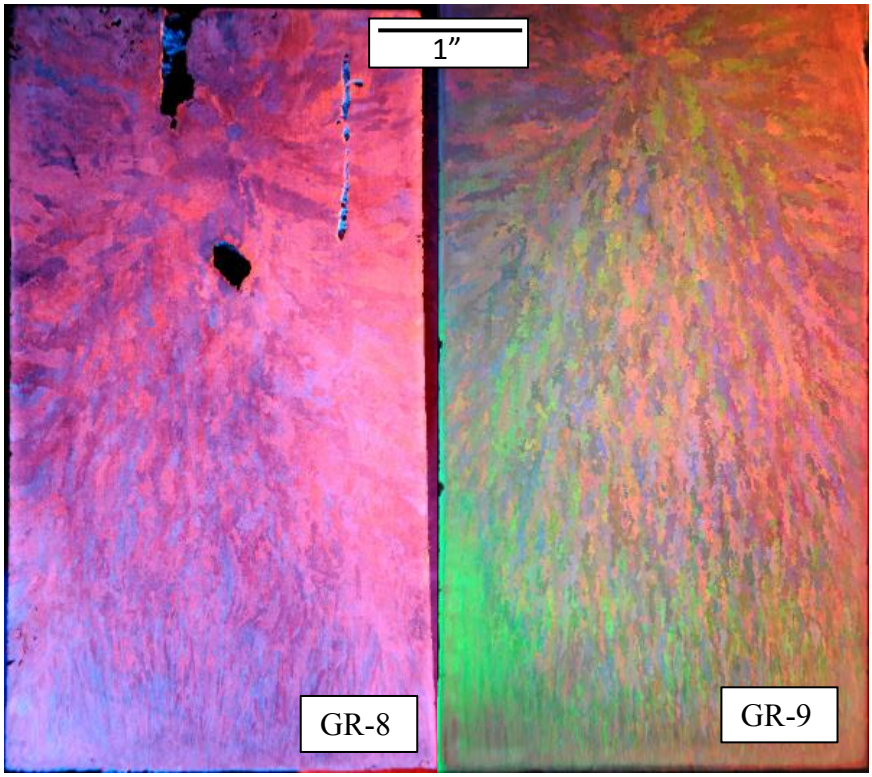

Figure 3.9. Macrostructure of base steel 8 and steel 9 added with 1%MA.

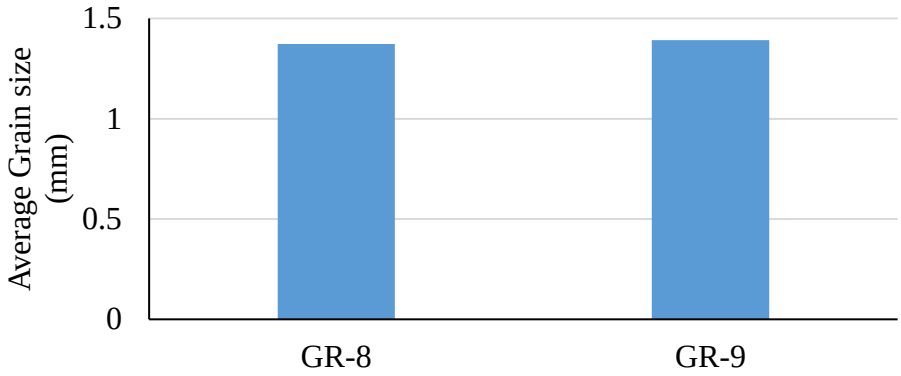

Figure 3.10. Average grain size of base steel 8 and steel 9 added with 1%MA.

3.2. FULLY AUSTENITIC – Nb STEELS

The base steel 14 and steel 15 used the fully austenitic nominal composition and the cylindrical casting deign on Figure 2.1(b). Steel 15 had the addition of 0.3%Nb in the ladle as FeNb. The composition is shown in Table 3.3.

The microstructure of steel 14 and 15 is shown in Figure 3.11(a,b). The inclusions formed by the addition of FeNb were larger than the original inclusions in the base steel. They had an elongated shape as the result of eutectic precipitation in the last areas to solidify. This typically means it precipitated by the end of solidification and thus it cannot act as a nucleation site.

Table 3.3. Composition in wt.% and (ppm) of steels 14 and 15.

	Fe	Mn	Al	C	Si	S	O(ppm)	N(ppm)	Nb	Ti
14	Bal.	27.7	5.11	1.47	1.29	0.0045	6	66	0.02	0.01
15	Bal.	29.3	5.29	1.58	1.33	0.0049	6	59	0.31	0.02

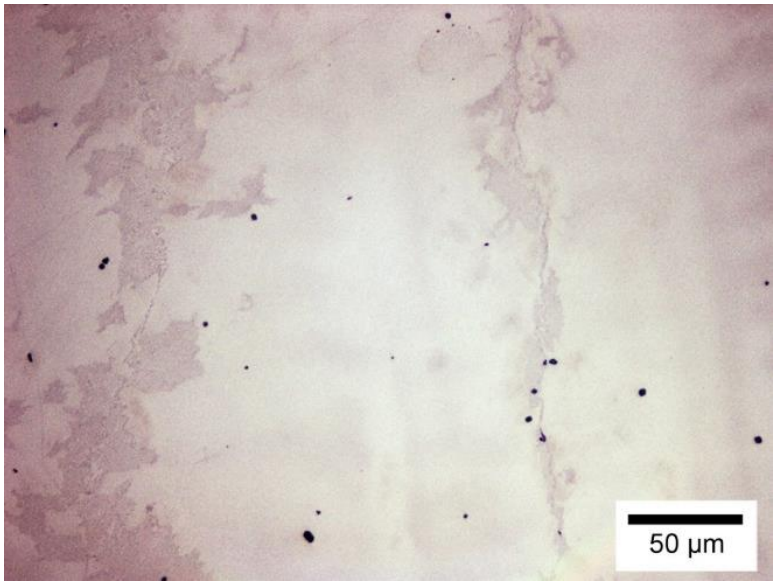

(a)

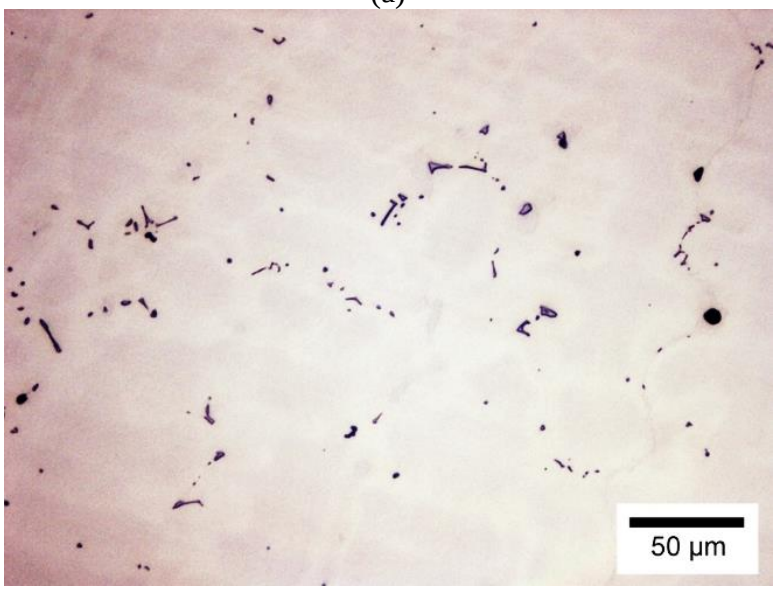

(b)

Figure 3.11. Microstructure of steel (a) 14 and (b) 15. Addition of FeNb produced Nb-rich carbonitride precipitation in the last areas to solidify and on grain boundaries.

The macrostructure in Figure 3.12 is very different from the microstructure of steels 8 and 9 in Figure 3.9. There is a clear transition from columnar structure to equiaxed grains and the grains are an order of magnitude larger than steels with the

mixed solidification mode. No grain refinement occurred due to the addition of Nb as shown in Figure 3.13, this was expected since there is clear evidence of late nucleation the Nb-based inclusions.

The inclusion population in Figure 3.14 shows that base steel 14 has the typical inclusion population of FeMnAl with no addition. Steel 15 had a very large density of Ti(C,N) of almost 963 inclusions/mm^2.

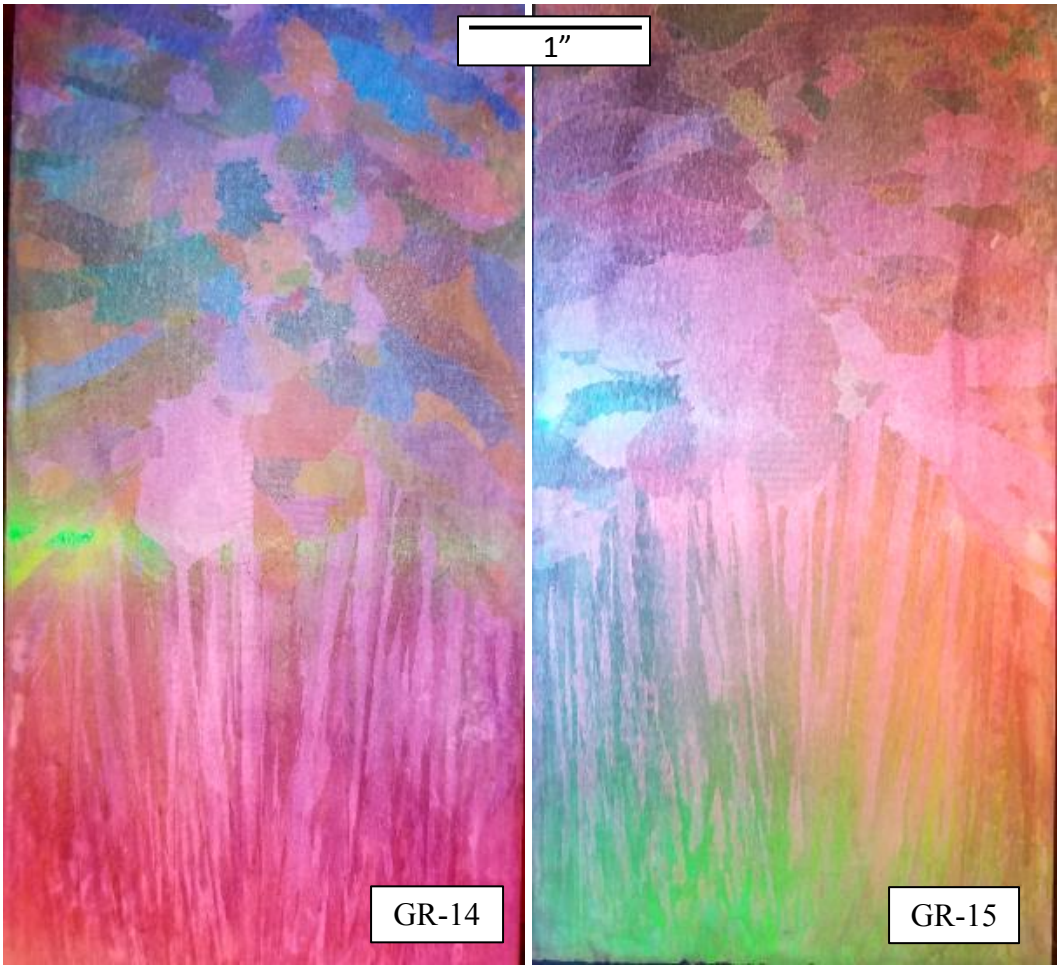

Figure 3.12. Macrostructure of (a) base steel 14 and (b) a steel with added Nb.

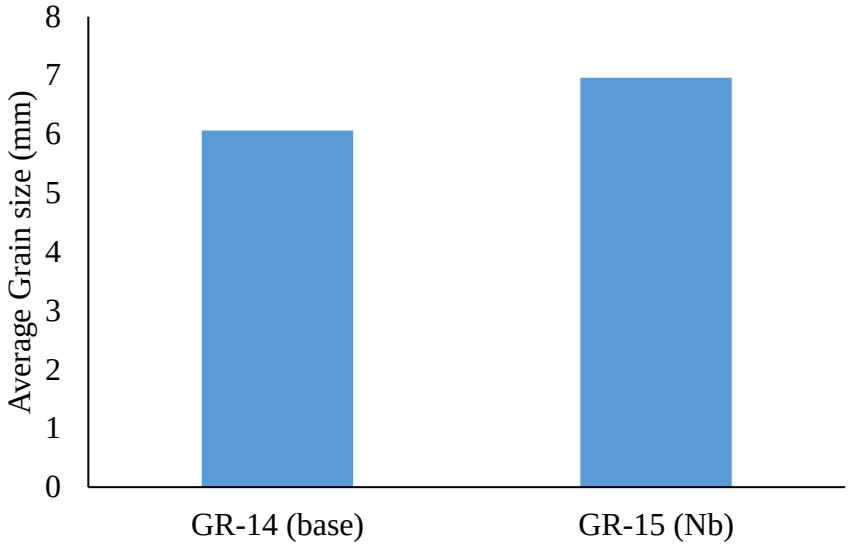

Figure 3.13. Average grain size of castings.

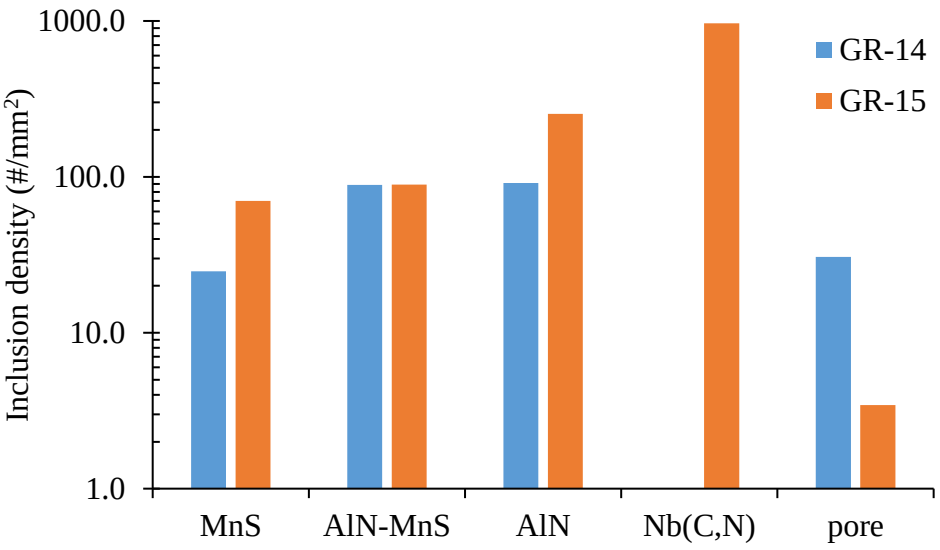

Figure 3.14. Inclusion population by type of steels 14 and 15.

3.3. FULLY AUSTENITIC – Ce STEELS

Steels 12 and 16 had addition of FeSiCe to promote formation of Ce-based inclusions, in particular, $AlCeO_3$. The compositions of steels cast are shown in Table 3.4. The Ce content was not measured due to limitation of the the OES system used. The Ce content was estimated based on charge amount and a recovery rate estimated at 90%.

The optical microstructure in Figure 3.15 shows that inclusions formed after the addition of cerium are concentrated in interdendritic regions and grain boundaries. This is clearer in Figure 3.15(b) where the Ce-based inclusions can be easily identified by the white color.

The macrostructure in Figure 3.16 shows a decrease on the length of the columnar zone from 76 mm in steel 10 to 42 mm in steel 16 with 0.12%Ce. But no apparent grain refinement on the equiaxed grain size. The average grain size of equiaxed region is on Figure 3.17, it shows that despite reducing the columnar zone, not much refinement occurred. Addition of Ce has been reported to grain refine FeMnAl at contents 0.1%.[6]

Table 3.4. Composition of steels used for analysis of effect of Ce addition on grain size.

	Fe	Mn	Al	C	Si	S(ppm)	O(ppm)	N(ppm)	Ni	Ce*	Ti
GR-10	Bal.	29.6	5.6	1.30	1.28	19	7	50	0.09	-	0.01
GR-12	Bal.	30.3	5.25	1.50	1.33	130	3	65	0.06	0.08	0.07
GR-16	Bal.	29.1	5.42	1.44	1.23	29	5	52	0.002	0.12	0.01

*Estimated from charge

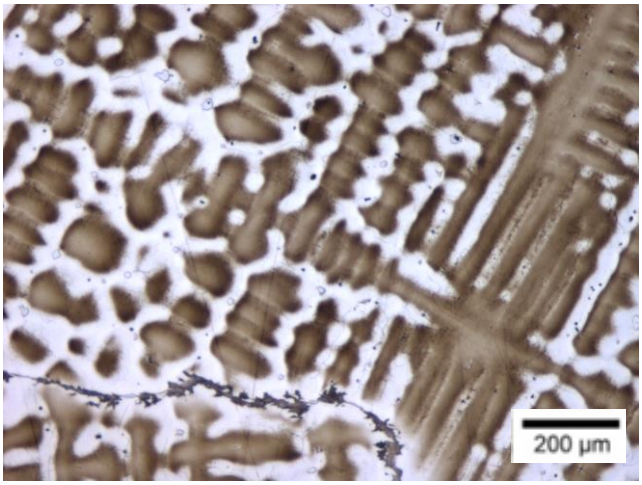

(a)

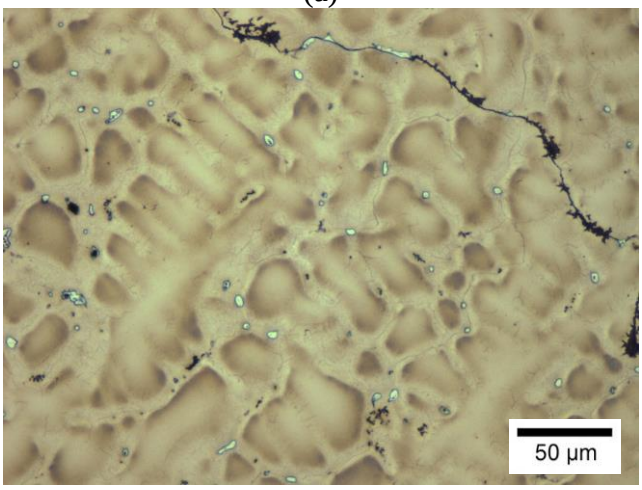

(b)

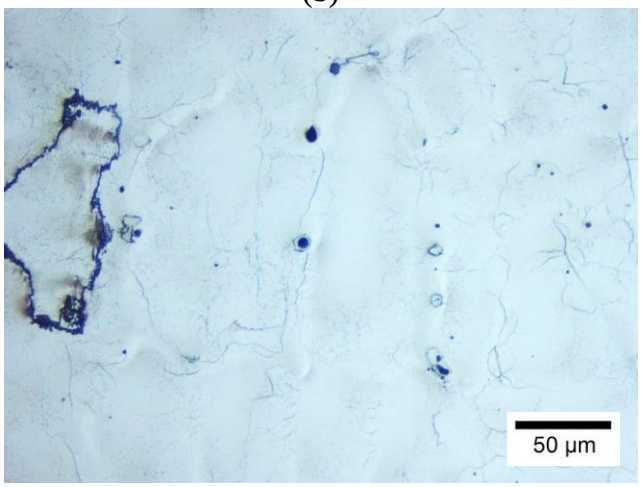

(c)

Figure 3.15. Microstructure of (a) base steel 10, and steels (b) 12 and (c) 16 with added Ce.

The inclusion population on the steels with added Ce was very complex. Inclusions were divided into several groups according to the type of inclusion as oxides, sulfides, nitrides or phosphides. The majority of inclusions were cerium sulfides and oxides, that either precipitated as a single inclusion or they were found co-precipitated around AlN. $AlCeO_3$ was present in very low numbers, or their existence was masked by other precipitating inclusions. According to the lattice misfit calculations previously reported, Ce-O and Ce-S are ideal for refinement of austenite, but may work for δ-ferrite. The steel used in the study that achieved grain refinement when Ce was added to alloys exhibiting a dual-phase solidification, which starts with δ-ferrite.[6] It seems that under the conditions tested, cerium works better for refinement of δ-ferrite in FeMnAl steels than for steels that have a primary austenite solidification path.

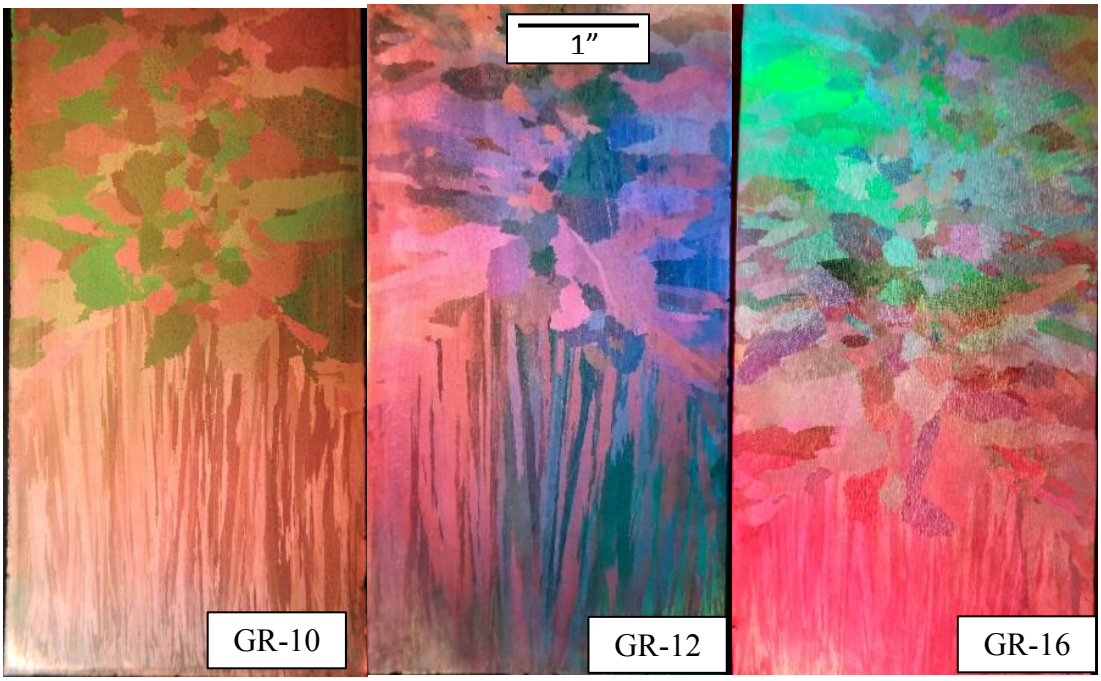

Figure 3.16. Macrostructure of base steel 10 and steels 12 and 16 with added Ce.

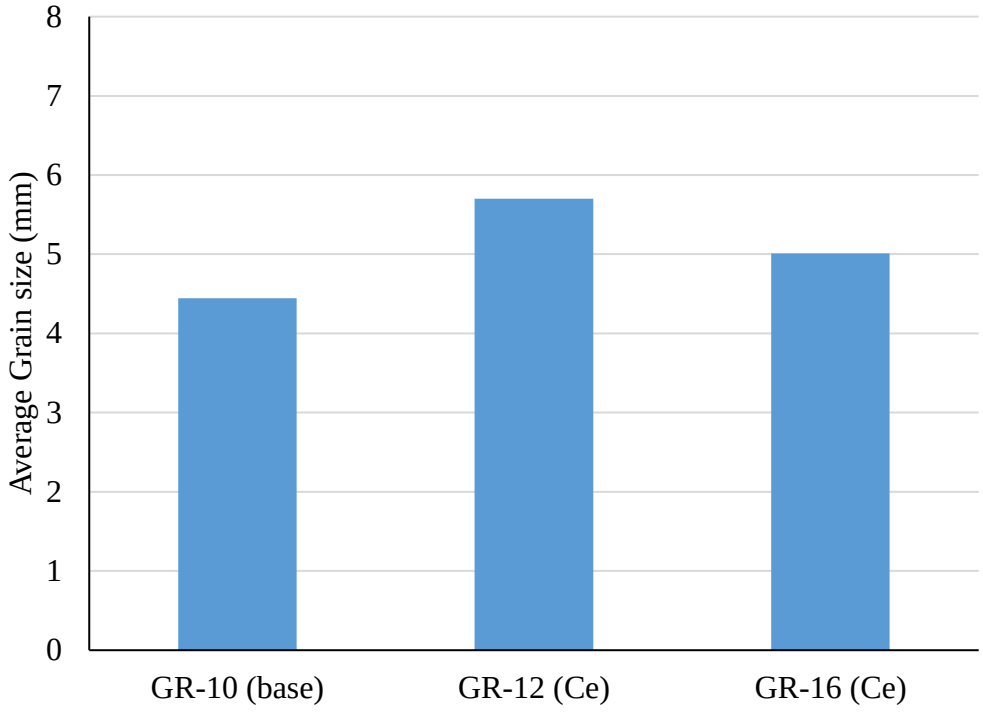

Figure 3.17. Average grain size of castings with added Ce.

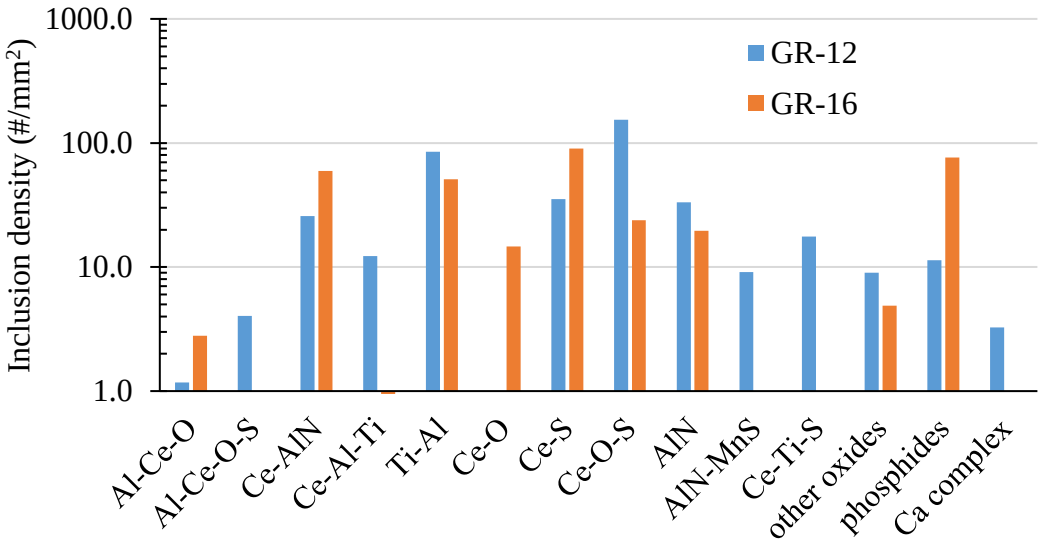

Figure 3.18. Inclusion populations of steels with added Ce.

3.4. FULLY AUSTENITIC – Ti STEELS

The last steels cast for evaluation of grain refinement through inoculation were conducted by addition of Mg followed by Ti to the furnace to produce $MgAl_2O_4$ followed by co-precipitation of Ti(C,N). The casting design was the one shown in Figure 2.1(b), however no chill plate was used to decrease cooling rate. The composition is shown in Table 3.5, magnesium was not quantified and is estimated to 0.005%Mg at a recovery rate of 30%. The microstructure shown in Figure 3.19, also appears to that inclusions are mostly in the interdendritic regions especially in image (b).

Table 3.5. Composition of steels added with Mg and Ti.

	Fe	**Mn**	**Al**	**C**	**Si**	**S(ppm)**	**O(ppm)**	**N(ppm)**	**Ni**	**Ti**
GR-20	Bal	30.6	5.3	1.42	0.87	34	5	55	0.002	-
GR-18	Bal	30.7	5.16	1.49	1.13	58	8	54	0.01	0.5
GR-19	Bal	29.2	5.63	1.39	1.02	36	6	44	0.002	0.3

The etched macrostructure shown in Figure 3.20 shows a decrease on length of the columnar zone, with almost full suppression in steel 18 when compared to base steel 20. The procedure for steel 18 and 19 was almost the same, except that the time between inoculation and pouring of steel 19 was faster than that of steel 18. The structure of steels 19 and 20, however, look very similar.

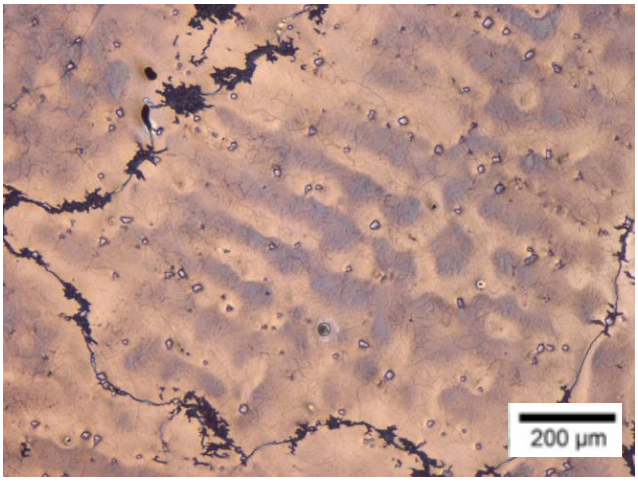

(a)

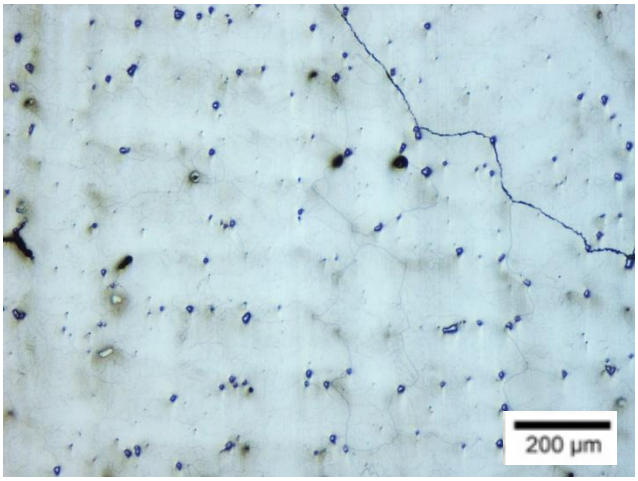

(b)

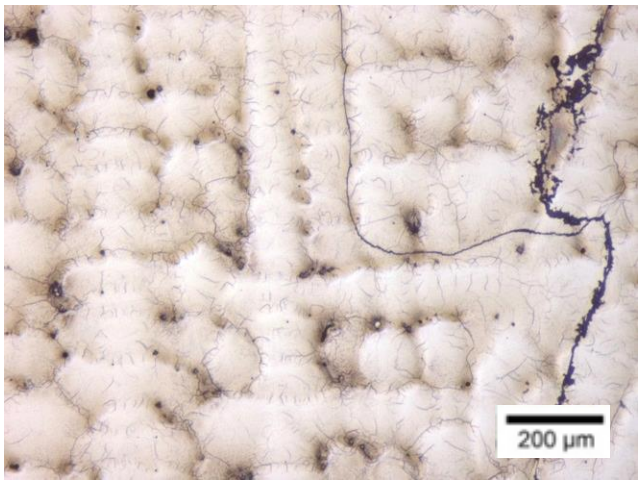

(c)

Figure 3.19. Microstructure of steels with addition of Mg+Ti. (a)Base steel without addition and (b,c) with added Mg-Ti.

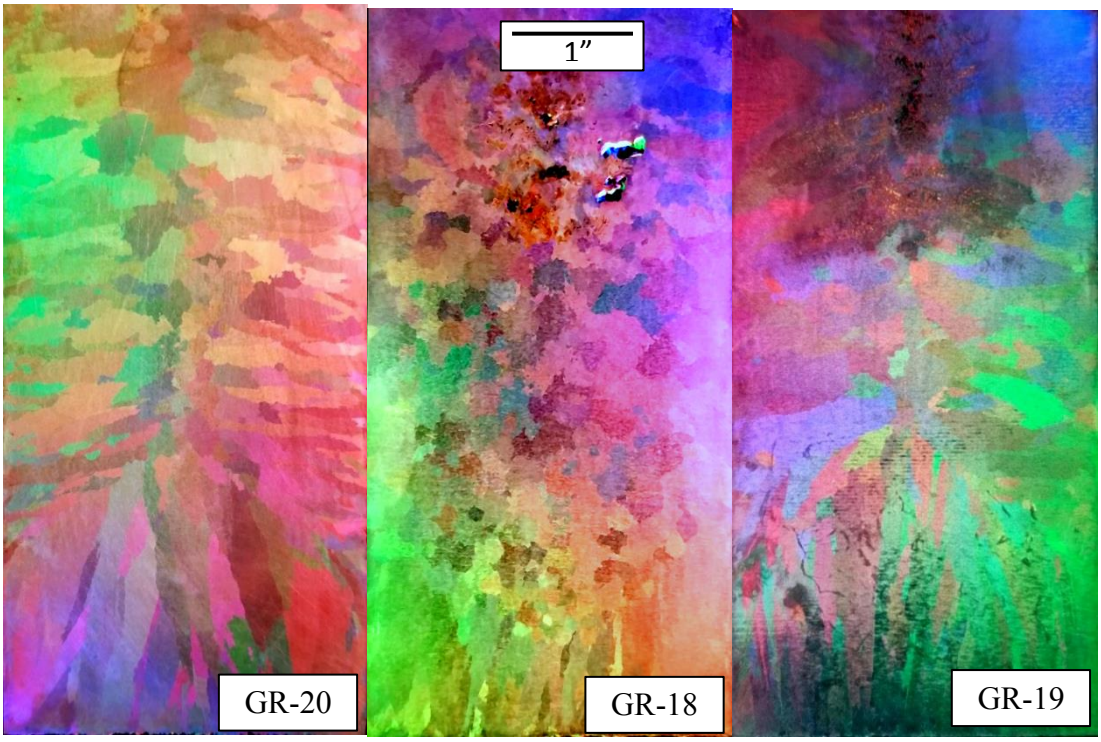

Figure 3.20. Macrostructure of the steels with Mg+Ti addition and base steel 20.

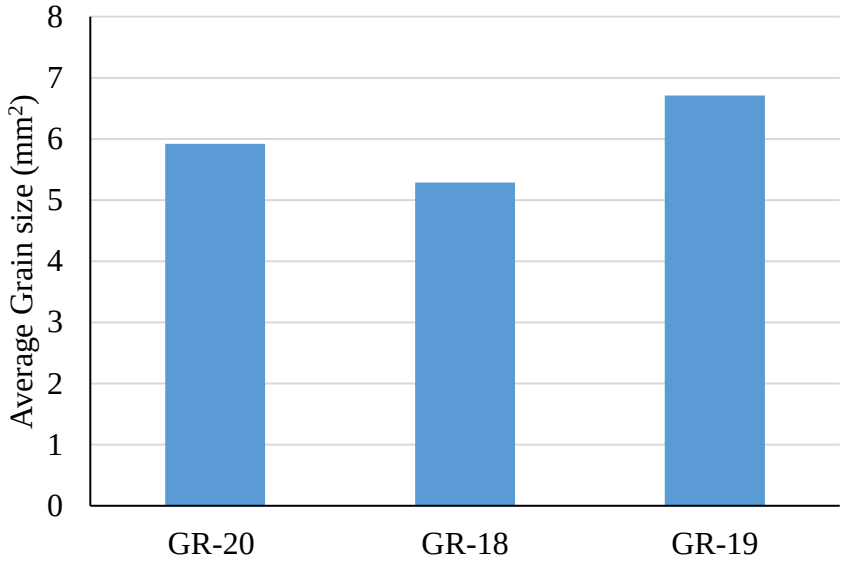

Figure 3.21. Average grain size of castings with added Ce.

The average diameter of equiaxed grain sizes in Figure 3.21 shows that despite the suppresion of the columnar grain zone and the apparent smaller overall grain, size, the average diameter of the equiaxed zone remained the same. Nonetheless, the expansion of the equiaxe zone is still an important and valid result.

The inclusion analysis shows many Ti-based inclusions, however inclusions with presence of Mg were not seen. This result most likely the result of the Ti-based inclusions masking the EDS signal of the lower atomic number spinel inclusions. The initial Mg-based inclusions are very small compared to the formed Ti(C,N) and despite the presence of spinel in the core of the Ti(C,N), the average composition of the inclusion does not have significant amount of Mg. Because of this, the automated classification based on composition can not separate the spinel inclusions that are in the center of Ti(C,N). Steels 18 and 19 had a similar number of Ti-based inclusions despite the fact that steel 18 had a higher Ti content.

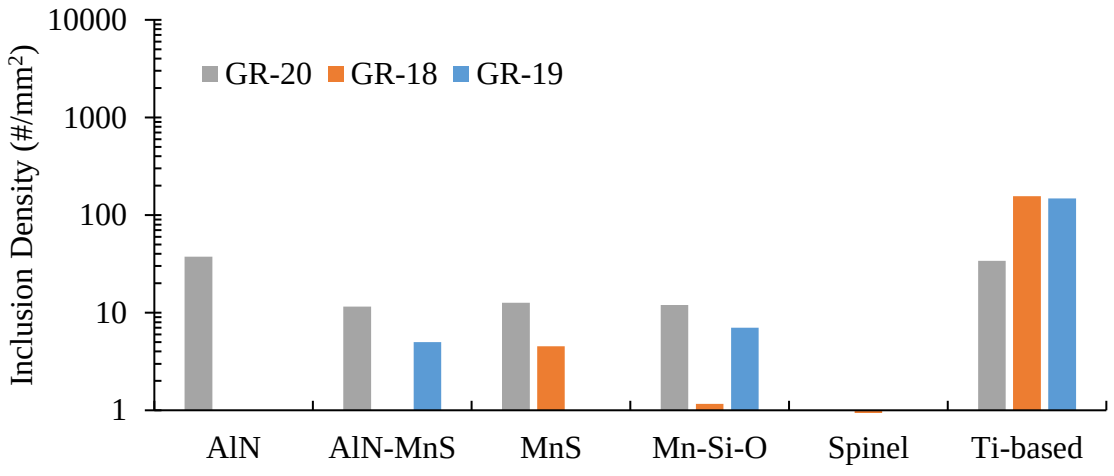

Figure 3.22. Inclusion number density by type for steels with Mg+Ti addition.

4. CONCLUSIONS

The use of different additions for grain refinement of the as-cast structure of different FeMnAlC steels was investigated. Additions of ferroalloys of FeNb, FeTi, FeTi+FeNb, a TiN Master Alloy, Ce additions, and a two-step inoculation method consisting of ferroalloy additions of FeSiMg+FeTi were experimentally studied. The resulting inclusions included Ti(C,N), Nb(C,N), complex cerium oxisulfides, and spinel or $MgAl_2O_4$.

No grain refinement was achieved for with additions of Nb, ferrotitanium, or with a TiN master alloy when the solidification path was as δ-ferrite followed by austenite. However, Ce additions were able provide some degree of grain refinement. When solidification was fully austenitic, Ce addition above 0.1% and addition of FeSiMg+FeTi were able to decrease the length of the columnar zone from 76 to 42mm for the Ce and almost a full suppression for additions of Mg followed by Ti to produce co-precipitation of Ti(C,N) on spinel inclusions.

REFERENCES

1. Bramfitt, Bruce L. "The effect of carbide and nitride additions on the heterogeneous nucleation behavior of liquid iron." Metallurgical Transactions, vol. 1, no. 7, 1970, pp. 1987-1995.

2. Van der Eijk, C., Haakosen, F., Klevan, O. S., & Grong, O. Development of Grain Refiner Alloys for Steels. In *AISTech Proceedings*, 2011.

3. Dahle, E. S. *Grain refinement of high alloyed steel with cerium addition*. Norwegian University of Science and Technology, Doctoral Thesis, Trondheim, Norway, 2011.

4. Gao, Jinzhu L., et al. "Effects of Rare Earth on the Microstructure and Impact Toughness of H13 Steel." Metals, vol. 5, no. 1, 2015, pp. 383-394.

5. Tuttle, R. "Examination of Steel Castings for Potential Nucleation Phases." International Journal of Metalcasting, vol. 4, no. 3, 2010, pp. 17-25.

6. Bartlett, Laura N., and Bryan R. Avila. "Grain Refinement in Lightweight Advanced High-Strength Steel Castings." International Journal of Metalcasting, vol. 10, no. 4, 2016, pp. 401-420.

BIBLIOGRAPHY

1. Hadfield, R. (1935). Special Steels. Nature, 135(3418), 741-745. doi:10.1038/135741a0

2. Dean, R. S., & Anderson, C. T. (1943). U.S. Patent No. US2329186A. Washington, DC: U.S. Patent and Trademark Office.

3. Ham, J. L., & Cairns Jr, R. E. (1958). Manganese joins aluminum to give strong stainless. Product Engineering, 29(52), 50-51.

4. Kim, H., Suh, D., & Kim, N. J. (2013). Fe–Al–Mn–C lightweight structural alloys: a review on the microstructures and mechanical properties. *Science and Technology of Advanced Materials*, *14*(1), 014205. doi:10.1088/1468-6996/14/1/014205

5. Bartlett, L. N., Van Aken, D. C., Peaslee, K. D., & Howell, R. A. (2010). Effect of Phosphorus and Silicon on the Precipitation of K-Carbides in Fe-30% Mn-9% Al-X% Si-0.9% C-0.5% Mo Alloys (10-069). Transactions of the American Foundrymen's Society, 118, 413.

6. Kalashnikov, I., Acselrad, O., Shalkevich, A., & Pereira, L. (2000). Chemical Composition Optimization for Austenitic Steels of the Fe-Mn-Al-C System. Journal of Materials Engineering and Performance, 9(6), 597-602. doi:10.1361/105994900770345430

7. Howell, R. A. (2009). *Microstructural influence on dynamic properties of age hardenable FeMnAl alloys* (Doctoral dissertation). Retrieved from http://scholarsmine.mst.edu/doctoral_dissertations/1940/

8. Huang, H., Gan, D., & Kao, P. (1994). Effect of alloying additions on the κ phase precipitation in austenitic Fe-Mn-Al-C alloys. *Scripta Metallurgica et Materialia*, *30*(4), 499-504. doi:10.1016/0956-716x(94)90610-6

9. Chen, S., Rana, R., Haldar, A., & Ray, R. K. (2017). Current state of Fe-Mn-Al-C low density steels. *Progress in Materials Science*, *89*, 345-391. doi:10.1016/j.pmatsci.2017.05.002

10. Acselrad, O., Kalashnikov, I. S., Silva, E. M., Khadyev, M. S., & Simao, R. A. (2006). Diagram of phase transformations in the austenite of hardened alloy Fe-28% Mn-8.5% Al-1% C-1.25% Si as a result of aging due to isothermal heating. *Metal Science and Heat Treatment*, *48*(11-12), 543-553. doi:10.1007/s11041-006-0133-8

11. Acselrad, O., Kalashnikov, I. S., Silva, E. M., Simao, R. A., Achete, C. A., L.C. Pereira. "Phase Transformation in Fe-Mn-Al-C Austenite Steels with Si Addition." Metallurgical Transactions A 33A (2002): 3569-3572.

12. Howell, R., Lekakh, S., Van Aken, D., Richards, V. (2008). The effect of silicon content on the fluidity and microstructure of Fe-Mn-Al-C Alloys. Trans. Am. Foundry Soc. 116. 867-878.

13. Bhadeshia, H.K.D.H. & Robert Honeycombe, Sir. (2006). The Effects of Alloying Elements on Iron-Carbon Alloys. 10.1016/B978-075068084-4/50006-6.

14. Buckholz, S. A., & Van Aken, D. C. (2013). On the influence of aluminum and carbon on abrasion resistance of high manganese steels. In *AFS Proceedings*. Schaumburg, IL: American Foundry Society.

15. Kalashnikov, I., Acselrad, O., Shalkevich, A., Chumakova, L., & Pereira, L. (2003). Heat treatment and thermal stability of FeMnAlC alloys. *Journal of Materials Processing Technology, 136*(1-3), 72-79. doi:10.1016/s0924-0136(02)00937-8

16. Chang, K., Chao, C., & Liu, T. (2010). Excellent combination of strength and ductility in an Fe–9Al–28Mn–1.8C alloy. Scripta Materialia, 63(2), 162-165. doi:10.1016/j.scriptamat.2010.03.038

17. Bartlett, L., & Van Aken, D. (2014). High Manganese and Aluminum Steels for the Military and Transportation Industry. *JOM, 66*(9), 1770-1784. doi:10.1007/s11837-014-1068-y

18. Choo, W., Kim, J., & Yoon, J. (1997). Microstructural change in austenitic Fe-30.0wt%Mn-7.8wt%Al-1.3wt%C initiated by spinodal decomposition and its influence on mechanical properties. *Acta Materialia*, *45*(12), 4877-4885. doi:10.1016/s1359-6454(97)00201-2

19. Sato, K., Tagawa, K., & Inoue, Y. (1990). Modulated structure and magnetic properties of age-hardenable Fe-Mn-Al-C alloys. Metallurgical Transactions A, 21(1), 5-11. doi:10.1007/bf02656419

20. Bartlett, L., Dash, A., Van Aken, D., Richards, V., & Peaslee, K. (2013). Dynamic Fracture Toughness of High Strength Cast Steels. *International Journal of Metalcasting, 7*(4), 17-33. doi:10.1007/bf0335556

21. Vaz Penna, R., Bartlett, L. N., & Constance, T. (2018). Understanding the Role of Inclusions on the Dynamic Fracture Toughness of High Strength Lightweight FeMnAl Steels. *International Journal of Metalcasting*. doi:10.1007/s40962-018-0273-9

22. Bartlett, L.N., Van Aken, D.C. (2013).Effect of Aluminum and Carbon on the Dynamic Fracture Toughness of Fe-Mn-Al-C steels. Trans. Am. Foundry Soc. 112.

23. Wakelin, D. H. (1999). *The Making, Shaping, and Treating of Steel: Ironmaking volume*.

24. Cheng, W., Song, Y., Lin, Y., Chen, K., & Pistorius, P. C. (2013). On the Eutectoid Reaction in a Quaternary Fe-C-Mn-Al Alloy: Austenite → Ferrite + Kappa-Carbide + M23C6 Carbide. *Metallurgical and Materials Transactions A, 45*(3), 1199-1216. doi:10.1007/s11661-013-2083-2

25. Park, J. H., Kim, D., & Min, D. J. (2012). Characterization of Nonmetallic Inclusions in High-Manganese and Aluminum-Alloyed Austenitic Steels. *Metallurgical and Materials Transactions A, 43*(7), 2316-2324. doi:10.1007/s11661-012-1088-6

26. Schulte, A.M., Lekakh, S.N., Van Aken, D.C., Richards, V.L. (2010) "Phosphorus Mitigation in Cast Lightweight Fe-Mn-Al-C Steel," AFS Trans. 118, pp. 451- 463

27. Mapelli, C. (2008). Non-metallic inclusions and clean steel. Metallurgia Italiana. 100.

28. Pickering, F. B. (1978). *Physical Metallurgy and the Design of Steels*. Applied Science Publishers.

29. Thornton, P. A. (1971). The influence of nonmetallic inclusions on the mechanical properties of steel: A review. *Journal of Materials Science, 6*(4), 347-356. doi:10.1007/bf02403103

30. Ånmark, N., Karasev, A., & Jönsson, P. (2015). The Effect of Different Non-Metallic Inclusions on the Machinability of Steels. *Materials, 8*(2), 751-783. doi:10.3390/ma8020751

31. Thornton, P. A. (1971). The influence of nonmetallic inclusions on the mechanical properties of steel: A review. *Journal of Materials Science, 6*(4), 347-356. doi:10.1007/bf02403103

32. Maciejewski, J. (2015). The Effects of Sulfide Inclusions on Mechanical Properties and Failures of Steel Components. *Journal of Failure Analysis and Prevention, 15*(2), 169-178. doi:10.1007/s11668-015-9940-9

33. Singh, V. (2009). *Inclusion modification in steel castings using automated inclusion analysis*(Master's thesis). Retrieved from https://scholarsmine.mst.edu/cgi/viewcontent.cgi?article=6422&context=masters_theses

34. Cox, T. B., & Low, J. R. (1974). An investigation of the plastic fracture of AISI 4340 and 18 Nickel-200 grade maraging steels. *Metallurgical Transactions*, *5*(6), 1457-1470. doi:10.1007/bf02646633

35. Hahn, G. T., Kanninen, M. F., & Rosenfield, A. R. (1972). Fracture Toughness of Materials. *Annual Review of Materials Science*, *2*(1), 381-404. doi:10.1146/annurev.ms.02.080172.002121

36. Ohno, M., & Matsuura, K. (2008). Refinement of As-cast Austenite Microstructure in S45C Steel by Titanium Addition. *ISIJ International*, *48*(10), 1373-1379. doi:10.2355/isijinternational.48.1373

37. Ohno, M., Yamaguchi, T., Matsuura, K., & Isobe, K. (2011). Suppression of Coarse Columnar Grain Formation in As-cast Austenite Structure of a Hyperperitectic Carbon Steel by Nb Addition. *ISIJ International*, *51*(11), 1831-1837. doi:10.2355/isijinternational.51.1831

38. Arvola, D., Lekakh, S., O'Malley, R., & Bartlett, L. N. (2018). *Effect of phase solidification sequence in stainless steel on grain refining efficient*. Paper presented at AISTech.

39. Costa e Silva, A. (2006). Thermodynamic aspects of inclusion engineering in steels. *Rare Metals*, *25*(5), 412-419. doi:10.1016/s1001-0521(06)60077-6

40. Seetharaman, S. (2013). *Treatise on Process Metallurgy, Volume 3: Industrial Processes*. London, England: Newnes.

41. Costa e Silva, A. V. (2018). Non-metallic inclusions in steel - origin and control. *Journal of Materials Research and Technology*, *7*(3), 283-299. Retrieved from https://doi.org/10.1016/j.jmrt.2018.04.003

42. Costa e Silva, A. V. (2018). Non-metallic inclusions in steel - origin and control. *Journal of Materials Research and Technology*, *7*(3), 283-299. Retrieved from https://doi.org/10.1016/j.jmrt.2018.04.003

43. Leslie, W.C. (1983). Inclusions and mechanical properties. ISS Trans. 2, 1–24

44. Moore, J. J., & Bodor, G. A. (1985). Steel deoxidation practice: Special emphasis on heavy section steel casting. In *Trans Am Foundry Soc* (pp. 99-114). American Foundry Society.

45. Liu, H., Liu, J., Michelic, S., Wei, F., Zhuang, C., Han, Z., & Li, S. (2016). Characteristics of AlN inclusions in low carbon Fe–Mn–Si–Al TWIP steel produced by AOD-ESR method. *Ironmaking & Steelmaking*, *43*(3), 171-179. doi:10.1179/1743281215y.0000000028

46. Schulte, A. M. (2010). *Foundry parameters for casting high-aluminum lightweight steel in complex shapes* (Master's thesis). Retrieved from http://scholarsmine.mst.edu/masters_theses/4997

47. The Casting Process, Carson Castings, 2017

48. Casting structure, FOUNDRY LEXICON, 2017.

49. Kurz, W., & Fisher, D. J. (1998). Fundamentals of solidification. Lausanne, Switzerland: Trans Tech.

50. K. Tamtal and D. Karunakar, "Grain Refinement of Cast Alloys: A Review," National Conference on RAME, Vol. 1, No.1, January 2014, pp. 1-14.

51. S. Kou: Welding Metallurgy, 2nd ed., Wiley, New York, NY, 2003.

52. Stefanescu, D. M. (2013). *Science and Engineering of Casting Solidification*. Berlin, Germany: Springer Science & Business Media.

53. P. Kumar and A. Choudhury, "A Brief Review on Grain Refinement In Steel Through Dynamic Strain Induced Transformation," Journal of Materials Science & Surface Engineering, Vol. 4, No. 5, September 2016, pp. 436-443.

54. J. Wallace, N. Church, and P. Wieser, "Grain Refinement of Steel Castings," Journal of Metals, Vol. 19, June 1967, pp. 44-51.

55. Bramfitt, Bruce L. "The effect of carbide and nitride additions on the heterogeneous nucleation behavior of liquid iron." Metallurgical Transactions, vol. 1, no. 7, 1970, pp. 1987-1995.

56. Van der Eijk, C., Haakosen, F., Klevan, O. S., & Grong, O. Development of Grain Refiner Alloys for Steels. In *AISTech Proceedings*, 2011.

57. Dahle, E. S. *Grain refinement of high alloyed steel with cerium addition*. Norwegian University of Science and Technology, Doctoral Thesis, Trondheim, Norway, 2011.

58. Gao, Jinzhu L., et al. "Effects of Rare Earth on the Microstructure and Impact Toughness of H13 Steel." Metals, vol. 5, no. 1, 2015, pp. 383-394.

59. Tuttle, R. "Examination of Steel Castings for Potential Nucleation Phases." International Journal of Metalcasting, vol. 4, no. 3, 2010, pp. 17-25.

60. Arvola, D. A., Lekakh, S. N., O'Malley, R. J., & Bartlett, L. N. (2018). Two Inoculation Methods for Refining As-Cast Grain Structure in Austenitic 316L Steel. International Journal of Metalcasting. doi:10.1007/s40962-018-0260-1

61. Andersson, M., Janis, J., Holappa, L., Kivio, M., Naveau, P., Brandt, M., … Van der Eijk, C. Grain size control in steel by means of dispersed non-metallic inclusions - GRAINCONT: Final report. Luxembourg: Publications Office of the European Union, 2011.

62. Li, Ming, et al. "A New Grain Refiner for Ferritic Steels." Metallurgical and Materials Transactions B, vol. 48, no. 6, 2017, pp. 2902-2912.

63. AtomWork Database. (2019, March 12). Retrieved from https://crystdb.nims.go.jp/crystdb/search-materials

64. Siafakas, D., Matsushita, T., Lauenstein, Å., Ekengård, J., & Jarfors, A. (2017). The Influence of Deoxidation Practice on the As-Cast Grain Size of Austenitic Manganese Steels. Metals, 7(6), 186. doi:10.3390/met7060186

65. Chu, C.M., et al. "Effect of alloying chemistry on the lattice constant of austenitic Fe-Mn-Al-C alloys." Scripta Metallurgica et Materialia, vol. 30, no. 4, 1994, pp. 505-508.

66. Bartlett, Laura N., and Bryan R. Avila. "Grain Refinement in Lightweight Advanced High-Strength Steel Castings." International Journal of Metalcasting, vol. 10, no. 4, 2016, pp. 401-420.

67. Bartlett, L.N., Van Aken, D.C., Lekakh, S., and Peaslee, K.D., “Mechanical Properties of Cerium-Treated Fe-Mn-Al-C Steel Castings,” AFS Transactions, vol. 119, paper 11-035 (2011)

68. Haakonsen, F., Solberg, J. K., Klevan, O. S., & Van der Eijk, C. Grain Refinement of Austenitic Manganese Steels. In AISTech Proceedings. AIST. 2011.

69. Mizumoto, M., Sasaki, S., Ohgai, T., & Kagawa, A. (2008). Development of new additive for grain refinement of austenitic stainless steel. International Journal of Cast Metals Research, 21(1-4), 49-55. doi:10.1179/136404608x361657

70. Van der Eijk, C., & Walmsley, J. (2001). Grain refinement of fully austenitic stainless steels using a Fe-Cr-Si-Ce master alloy. In *59th Electric Furnace and 19th Process Technology Conferences*. Phoenix, AZ.

71. Grong, Øystein, et al. "Microstructure Control of Steels through Dispersoid Metallurgy Using Novel Grain Refining Alloys." ISIJ International, vol. 46, no. 6, 2006, pp. 824-831.

VITA

Rairu Vaz Penna was born in Ouro Preto, Brazil. During his undergraduate time, had an internship at Aperam Inox Brazil and worked on a research project with companies VALE and VLI on material development for railroad applications. He studied for one year at Missouri University of Science and Technology as a Metallurgical Engineering exchange student with a "Science Without Borders" scholarship from Brazilian government prior to graduating with a Bachelor of Science in Metallurgical Engineering from Universidade Federal de Ouro Preto in September 2016.

After graduation, Rairu continued his studies in a master's program at Missouri University of Science and Technology as a graduate research assistant, starting in January 2017. His research topic was on the influence of inclusion population on the microstructure and properties of FeMnAl steels under the guidance of Dr. Laura Bartlett, Dr. Ronal O'Malley, and Dr. Simon Lekakh. During his master's, Rairu worked with the development of a grain refinement method for FeMnAl steel by casting dozens of different alloys and analyzing its microstructure and properties. He also authored a publication in conference proceedings and three journal articles. Rairu received his Master of Science in Metallurgical Engineering from Missouri S&T in May 2019.